

*Kaleeswaran Balasubramaniam, M.Sc. Eng*



**DAMAGE LOCALIZATION BASED ON  
PIEZOELECTRIC AND FIBER BRAGG GRATING  
SENSED GUIDED WAVES**

A dissertation submitted to the Scientific Board of the Szewalski Institute of  
Fluid-Flow Machinery, Polish Academy of Sciences in partial fulfilment of the  
requirements for the Degree of Doctor of Philosophy

Supervisor: Dr Paweł Henryk Malinowski, DSc., PhD

Auxiliary Supervisor: Dr Rohan Soman, PhD

Gdańsk, Poland  
March 2023

## Acknowledgement

I would like to express my sincere gratitude to my supervisor Prof Paweł Małinowski, and auxiliary supervisor Dr Rohan Soman for their guidance, motivation, and scientific observations. I would also like to express my sincere thanks to Prof Tomasz Wandowski, Mr Piotr Fiborek, Prof Maciej Radzieński, Prof Mirosław Sawczak, and Dr Mohammad Ali Fakih, who were always up for the discussions and sharing their experiences. My sincere gratitude to my collaborators Dr Shirsendu Sikdar from Cardiff University, Prof Michał Jurek and Prof Dominika Ziaja from Polytechnic Rzeszów. I also want to thank all my friends from Instytut Maszyn Przepływowych im. R. Szewalskiego Polskiej Akademii Nauk (IMP PAN) with whom I shared many memories and celebrations during my stay in Poland. I am also indebted to Ms Renata, and Ms Justyna for their unconditional helps in administrative support.

I am immensely grateful for the unwavering support and guidance of Prof Wiesław Ostachowicz during my PhD journey. My mother Mrs Savithri Balasubramaniam's unwavering affection and my father Mr Balasubramaniam's disciplinary and motivational words have always encouraged me to strive for greater heights. I would also like to thank my brother, wife, and other family members for their support during this challenging period. The road to completing my PhD was full of obstacles and challenges and was a tough journey for me. However, I am indebted to all those who motivated and supported me in every possible way to achieve this significant accomplishment. Finally, I want to acknowledge the funding provided by the National Science Centre (NCN), Poland under two project grants: SONATA BIS 2016/22/E/ST8/00068 and OPUS 2019/33/B/ST8/01699, which enabled me to pursue my research journey.

Place: Gdańsk, Poland

Date: March 2023

Kaleeswaran Balasubramaniam

## **Abstract**

Structural health monitoring (SHM) is used in aerospace, civil, naval, and automotive industries to monitor structures for damage, stress/strain, and vibrations. The aim is to ensure reliability through continuous/active/online monitoring that is as reliable as proven non-destructive techniques (NDT). Ultrasonic-guided waves (GW) are a promising technique for SHM, but dispersion effects, electromagnetic noises, and environmental factors can affect the accuracy of the data collected.

The research aims to develop an effective multistep damage identification process (detection, localization and quantification) using the proposed SHM-GW method. The proposed multi-step method was tested on many isotropic and anisotropic structures with different kinds of damage and also using various types of sensing units. In this research work, an improved GW damage localization technique with sector-based elliptical (SEC) methodology is developed to localize damages in various structures. The research also showcases quick damage detection and damage quantification methods. The SEC effectively identified damage at multiple locations, sizes, and types. The technique originally developed for piezoelectric sensors and laser Doppler vibrometry (LDV)-based scanning points were later applied to the GW sensing study using fiber optic Bragg grating (FBG) sensors.

The implementation of hybrid FBG-PZT sensors in damage identification is also carried out in this research using the proposed method. The use of remote FBG bonding and direct bonding strategies for GW sensing is also studied along with the application of the varying bond (adhesive) line length as a parametric factor. The proposed damage identification multi-step methodology was also tested on numerical finite element models (FEM) to validate the experimental FBG-PZT studies.

## Contents

<b>Acknowledgement</b>	<b>i</b>
<b>Abstract</b>	<b>ii</b>
<b>List of Symbols, Abbreviations</b>	<b>vii</b>
<b>List of Tables</b>	<b>ix</b>
<b>List of Figures</b>	<b>xiii</b>
<b>List of Publications</b>	<b>xiv</b>
<b>1 Introduction to GW-based SHM systems</b>	<b>1</b>
1.1 Overview . . . . .	1
1.2 Basics of SHM systems . . . . .	2
1.2.1 PZT and FBG sensors . . . . .	4
1.3 Elastic wave propagation in plates . . . . .	5
1.3.1 Elastic wave motion: Rayleigh waves . . . . .	5
1.3.2 Elastic wave motion: Love waves . . . . .	6
1.3.3 Elastic wave motion: Lamb waves . . . . .	7
1.3.4 Elastic wave motion: SH waves . . . . .	9
1.4 Analysis of structures using GW . . . . .	9
<b>2 State of the art in GW studies</b>	<b>11</b>
2.1 SHM and NDE methods . . . . .	11
2.2 GW-based SHM methods . . . . .	14
2.2.1 Damage detection using GW methods . . . . .	15
2.2.2 Damage localization using GW methods . . . . .	16
2.2.3 Sensor optimization in GW studies . . . . .	17
2.2.4 Reasons for GW signals variation . . . . .	18
2.2.5 Temperature effects studied using GW . . . . .	18
2.2.6 GW studies using LDV . . . . .	22



2.2.7	GW studies using FEM . . . . .	25
2.2.8	Summary . . . . .	25
2.3	GW sensing instruments used in the study . . . . .	25
2.3.1	GW analysis using LDV . . . . .	26
2.3.2	Data acquisition using DAQR . . . . .	27
2.3.3	GW analysis using PZT and FBG hybrid method . . . . .	27
<b>3</b>	<b>Motivation/objectives of the research</b>	<b>30</b>
3.1	Research gaps and objective . . . . .	30
3.1.1	SHM-GW common multi-step method . . . . .	31
3.1.2	SHM-GW analysis using FBG remote bonding . . . . .	35
3.2	Research objectives achieved . . . . .	36
3.3	List of material specimens investigated . . . . .	38
3.4	Thesis outline . . . . .	40
3.5	Thesis to be proven . . . . .	40
<b>4</b>	<b>GW-based damage localization in structures</b>	<b>42</b>
4.1	Elliptical method in damage localization . . . . .	42
4.2	Sectorial Elliptical (SEC) method in damage localization . . . . .	45
<b>5</b>	<b>Elliptical algorithm damage analysis with experimental cases</b>	<b>49</b>
5.1	ACS: impact damage analysis using LDV scanning points . . . . .	49
5.1.1	Methodology . . . . .	49
5.1.2	Details about ACS and damages . . . . .	49
5.1.3	Damage localization discussion and results . . . . .	50
5.1.4	Sectional conclusion . . . . .	53
5.2	GFRPS: Multiple BVID analysis using LDV scanning points . . . . .	54
5.2.1	Methodology . . . . .	54
5.2.2	Details about GFRPS and damages . . . . .	55
5.2.3	Damage localization discussion and results . . . . .	55
5.2.4	Sectional conclusion . . . . .	59
<b>6</b>	<b>SHM-GW common method: damage identification analysis</b>	<b>60</b>
6.1	SCS: multiple debond identification using PZTs . . . . .	60
6.1.1	Methodology . . . . .	61
6.1.2	Details about experimental setup, SCS and damages . . . . .	62
6.1.3	Results and discussion . . . . .	64
6.1.3.1	Choice of the GW mode and frequency . . . . .	64
6.1.3.2	Damage detection step results: Step 1 . . . . .	64
6.1.3.3	Damage localization using SEC: Step 2 . . . . .	66

6.1.3.4	Computational efficiency and accuracy studies .	68
6.1.3.5	Damage quantification using CM: Step 3 . . . . .	72
6.1.4	Sectional conclusion . . . . .	72
6.2	CFRPS: multiple impact damage identification using LDV scanning points . . . . .	75
6.2.1	Details about experimental setup, CFRPS and damages .	76
6.2.2	Initial discussion . . . . .	77
6.2.3	Damage localization results and discussions . . . . .	77
6.2.3.1	RMSD analysis of signals: Step 1 . . . . .	78
6.2.3.2	SEC models and results: Step 2 . . . . .	79
6.2.4	Sectional conclusion . . . . .	80
6.3	ALS: multiple damage identification using FBG sensors . . . . .	81
6.3.1	Details about ALS and damages . . . . .	81
6.3.2	Results and discussion . . . . .	81
6.3.3	Multiple damage detection and localization: Steps 1,2 . .	82
6.4	ALS-FEM: multiple damage identification using FEM models .	84
6.4.1	FEM model preparation . . . . .	87
6.4.2	Dynamic explicit procedure . . . . .	88
6.4.3	FBG PZT hybrid coupled model . . . . .	88
6.4.4	Theoretical equations . . . . .	89
6.4.5	CD similarity analysis: Step 1 . . . . .	91
6.4.6	SEC localization analysis of FEM models: Step 2 . . . .	92
6.5	Sectional Conclusion . . . . .	94
<b>7</b>	<b>Effect of GW in FBG direct and remote bonding configurations</b>	<b>95</b>
7.1	FBG sensor bonding configurations . . . . .	95
7.1.1	Experimental analysis . . . . .	95
7.1.2	Results and Discussions . . . . .	99
7.2	FBG through thickness study: FEM study . . . . .	99
<b>8</b>	<b>Conclusion and future work</b>	<b>105</b>
8.1	Thesis review: overall outcomes . . . . .	105
8.2	Summary of the thesis contributions . . . . .	107
8.3	Future work . . . . .	108
8.4	Proven thesis . . . . .	109
<b>A</b>	<b>Appendix</b>	<b>110</b>
A.1	ACS inspection . . . . .	110

A.1.1	Velocity profile . . . . .	110
A.2	SCS inspection . . . . .	111
A.3	CFRPS inspection . . . . .	114
A.3.1	FWF waveform plots . . . . .	114
A.4	ALS monitoring with FBGs . . . . .	116
A.5	FEM Matlab pseudocode . . . . .	117
A.5.1	FWF Analysis . . . . .	118
A.6	FBG Reflectivity spectrum study . . . . .	119
A.6.1	GUI Matlab-based toolbox . . . . .	121
A.6.2	Validation . . . . .	123

<b>Bibliography</b>	<b>125</b>
---------------------	------------

## List of Symbols and Abbreviations

$^{\circ}$	Degree
$\delta t$	Change in time
$\delta P$	Difference in data/value
$Exp$	Exponential
$exp$	Experimental
$ref$	Referential
$w.r.t$	With respect to
$i.e$	That is
SHM	Structural Health Monitoring
NDT	Nondestructive testing
NDE	Nondestructive evaluation
LW	Lamb waves
SH	Shear Horizontal waves
GW	Guided waves
S0	Fundamental Symmetric guided wave mode
A0	Fundamental Anti-Symmetric guided wave mode
PZT	Piezoelectric/Lead Zirconate Titanate transducer
FBG	Fiber Bragg Grating sensor
DAQ	Data Acquisition and Receiver
LDV	Laser Doppler Vibrometer
IRT	Infrared thermography
UT	Ultrasound inspection Techniques
RAPID	Reconstruction Algorithm for Probabilistic Inspection of Damage
SEC	Sectional Elliptical method
CM	Confusion Matrix
DI	Damage Indices
TOF	Time of Flight
HT	Hilbert Transformation
RMS	Root Mean Square
RMSD	Root Mean Square Deviation

WRMS	Weighted Root Mean Square
RRMS	Radial Root Mean Square
RWF	Residual Weight Factor
CD	Cosine Distance
BVID	Barely Visible Impact Damage
ICD	Impact Crack Damage
FWF	Full Wave Field visualization
ACS	Aluminium nomex Composite Structure
SCS	Sandwich honeycomb Composite Structure
CFRP	Carbon Fiber Reinforced Polymer
CFRPS	Carbon Fiber Reinforced Polymer Structures
GFRP	Glass Fiber Reinforced Polymer
GFRPS	Glass Fiber Reinforced Polymer Structures
ALS	Aluminium Specimen
LAMSS	Laboratory for Active materials and Smart structures
FEM	Finite Element Method
SEM	Spectral Element Method
GUI	Graphical User Interface
FWHM	Full Width at Half Maximum
TPI	True Positive Index

## List of Tables

3.1	SHM levels for damage study. . . . .	31
3.2	Selected materials/structures for the SHM-GW analysis. . . . .	38
5.1	Material properties of the ACS. . . . .	50
5.2	Case models studied using the elliptical algorithm. . . . .	52
5.3	Error estimated using the elliptical algorithm. . . . .	54
5.4	SHM elliptical threshold damage localization on LDV data. . . . .	59
5.5	SHM elliptical threshold damage localization on SEM data. . . . .	59
6.1	Experimental cases studied. . . . .	62
6.2	Damage detection step for inside monitoring: DAQR data. . . . .	66
6.3	Damage detection step for outside monitoring: DAQR data. . . . .	67
6.4	Experimental cases: damage localization and error estimation. . . . .	69
6.5	Experimental case study: grid points and time reduction. . . . .	71
6.6	Numerical cases: damage localization and error estimation. . . . .	71
6.7	Numerical case study: grid points and time reduction. . . . .	71
6.8	Pixel count-based error estimation. . . . .	74
6.9	Material properties of CFRPS. . . . .	76
6.10	Predicted group velocity values. . . . .	79
6.11	Error estimation using SEC [all units in cm]. . . . .	79
6.12	Time and grid reduction percentage with and without SEC. . . . .	80
6.13	Damage estimation analysis predicted with SEC. . . . .	84
6.14	Time and grid point difference with and without SEC. . . . .	85
6.15	FEM model parameters. . . . .	88
6.16	Damage estimation analysis predicted with SEC. . . . .	94
6.17	Time and grid point reduction with and without SEC. . . . .	94
7.1	PZT Connection types and effect of GW. . . . .	98
A.1	Velocity values obtained from DAQR and Abaqus data. . . . .	113
A.2	Material properties of ALS. . . . .	116
A.3	Comparing theoretical and numerical results. . . . .	118

## List of Figures

1.1	SHM systems overview: exemplary aeronautical application. . .	3
1.2	PZT used in the GW measurements. . . . .	4
1.3	Schematic representation: optical fiber and FBG. . . . .	5
1.4	FBG used in the GW measurements. . . . .	6
1.5	Exemplary FBG's response as a function of strain. . . . .	6
1.6	Rayleigh waves on a semi-infinite medium. . . . .	7
1.7	Love waves in a solid medium. . . . .	7
1.8	Fundamental LW modes in a thin plate. . . . .	8
1.9	SH waves on a solid media. . . . .	9
1.10	GW measuring systems: (a) Pitch catch, (b) Pulse echo. . . .	10
2.1	Comparison of SHM and NDT techniques. . . . .	12
2.2	Visual inspection done at IMP PAN. . . . .	12
2.3	Infrared thermography experimental setup at IMP PAN. . . .	13
2.4	An exemplary acoustic emission-based monitoring. . . . .	14
2.5	GW-based SHM monitoring using DAQR setup at IMP PAN. .	15
2.6	Exemplary TOF of GW modes. . . . .	16
2.7	Temperature effects study using PZT network at IMP PAN. .	19
2.8	PZT positioned for SHM monitoring of CFRPS. . . . .	20
2.9	Healthy signals obtained (a) at different temperature conditions (b) zoomed in the first peak of (a) signals. . . . .	21
2.10	An exemplary peak picking crest and trough from GW signals at T1 25 °C . . . . .	22
2.11	GW amplitude trend due to temperature effects excitation by P3 and sensed by P8 of sample in Figure 2.8 under (a) Healthy, (b) Damage. . . . .	23
2.12	GFRPS with stiffener assembly and located debond using LDV- RMS study. . . . .	24
2.13	Schematic LDV setup for GW acquisition. . . . .	26
2.14	DAQR Schematic setup. . . . .	28
2.15	Fiber optics GW experiment schematic setup. . . . .	29

2.16	Reflectivity spectrum slope. . . . .	29
3.1	DI study : (a) Schematic plate, (b) RMSD, (b) CD. . . . .	32
3.2	Damage detection: Step 1. . . . .	33
3.3	Damage localization: Step 2. . . . .	34
3.4	Sensor network: (a) PZT-PZT, (b) PZT-FBG. . . . .	35
3.5	Damage quantification: Step 3. . . . .	35
3.6	Changing FBG bond length with remote bonding configuration. . . . .	36
4.1	Signal paths showing incident and reflections in healthy and damaged structure. . . . .	42
4.2	$TOF^{ref}$ distance approximation using elliptical method. . . . .	43
4.3	$TOF^{ref}$ and $TOF^{exp}$ peak picking calculation. . . . .	44
4.4	Ellipse resolution for $\tau$ at: (a) $3 \mu s$ , (b) $5 \mu s$ . . . . .	45
4.5	Flowchart of the elliptical algorithm. . . . .	45
4.6	Exemplary approach for Step 1-RMSD detection and Step 2- SEC localization. . . . .	47
4.7	Exemplary flowchart of the SEC-SA method. . . . .	47
5.1	Methodological flowchart in ACS analysis. . . . .	50
5.2	ACS facet with damages and cross-section of core ACS. . . . .	51
5.3	ACS backside with Nomex core and damages. . . . .	51
5.4	Sensor arrangements: (a) Case 1 quadrant I-IV, (b) Case 4 quadrant II. . . . .	52
5.5	Experimental elliptical algorithm results with different sensor arrangements: (a) Case 1, (b) Case 2, (c) Case 3, (d) Case 4. . . . .	53
5.6	Methodological flowchart in GFRPS analysis. . . . .	55
5.7	GFRPS with PZT positions and BVIDs. . . . .	56
5.8	LDV-RRMS plots excitation from PZT1 at different frequencies. . . . .	56
5.9	LDV-RRMS plots excitation for 200 kHz from PZT1-PZT4. . . . .	57
5.10	Distribution of circular scanning nodal points for SHM study. . . . .	57
5.11	Localization threshold results (a) SEM data,(b) LDV data. . . . .	58
6.1	Proposed common multi-step methodology in damage identifi- cation analysis. . . . .	61
6.2	Experimental setup with DAQR. . . . .	63
6.3	Schematic representation of the SCS with debonding [square] and artificial masses [M], positions (coordinates of the centre) of PZTs. . . . .	63
6.4	Peak peaking of A0 mode from 150 kHz excitation. . . . .	64



6.5	Amplitude (vs) frequency plot of A0 mode. . . . .	65
6.6	Damage detection step for inside monitoring: DAQR results of Case 2. . . . .	65
6.7	Damage detection step for outside monitoring: DAQR experimental: (a) Case 1, (b) Case 2, (c) Case 3 and (d) Case 4. . . .	66
6.8	SEC experimental results: (a) Case 1, (c) Case 2, Threshold of SEC results: (b) Case 1 (d) Case 2. . . . .	68
6.9	SEC experimental results: (a) Case 3, (c) Case 4, Threshold of SEC results:(b) Case 3, (d) Case 4. . . . .	69
6.10	SEC numerical results: (a) Case 6 (c) Case 7 and (e) Case 8. Threshold of SEC results: (b) Case 6 (d) Case 7 and (f) Case 8.	70
6.11	Case 8 of Figure 6.10 damage map at different percentages (thresholds). . . . .	73
6.12	Zoomed Case 8 of Figure 6.10 damage map at different percentages (thresholds). . . . .	74
6.13	Threshold (vs): (a) Miss hits, (b) TPI. . . . .	75
6.14	Damaged:(a) CFRPS, (b) Sensing points for SEC study. . . . .	77
6.15	RMSD maps : (a) First wave arrival, (b) Entire signal length. .	78
6.16	SEC localization results (a) Case 1: LDV case 1 (b) Case 2: SEM case 2. . . . .	80
6.17	Experimental SHM setup with FBG and PZTs at IMP PAN. . .	82
6.18	Schematic representation of the ALS and damage locations. . .	83
6.19	GW signals sensitivity with added rubber sheets. . . . .	83
6.20	Exemplary signal difference between Healthy and Damage D1. .	84
6.21	CD bars sectorial regions: experimental damage cases. . . . .	85
6.22	Localized SEC results of different damage scenarios. . . . .	86
6.23	ALS: (a) Pristine, (b) with multiple simulated damages. . . . .	87
6.24	FEM (a) Meshed model, (b) Excitation from the cylindrical coordinate nodes. . . . .	89
6.25	Theoretical reflectivity spectrum. . . . .	91
6.26	CD bars sectorial regions: numerical damage cases. . . . .	92
6.27	Localized FEM SEC results of different damage scenarios. . . .	93
7.1	Different PZT connection types. . . . .	96
7.2	Process :(a) Remote bonding, (b) Direct bonding, (c) Curing. .	97
7.3	Schematic ALS cross-sectional configuration with (a) direct bonding, (b) remote bonding. . . . .	98
7.4	Remote bonding : (a) A0 amplified, (b) S0 amplified, (c) S0, A0 modes. . . . .	100

7.5	Amplitude pattern trend of remote bonded FBG at various frequencies and bond lengths. . . . .	101
7.6	Exemplary HT envelope of out-phase direct bonding S0 GW mode at 100 kHz. . . . .	101
7.7	Amplitude pattern trend of direct bonded FBG at various frequencies and bond lengths. . . . .	102
7.8	FEM FBG meshed model. . . . .	103
7.9	FEM model to check GW sensitivity. . . . .	103
7.10	GW signals obtained via in-plane vibration. . . . .	104
7.11	Frequency thickness profile. . . . .	104
8.1	SHM levels 1-3 achieved using multi-step methodology. . . . .	106
A.1	FWF analysis at different time instances. . . . .	110
A.2	<i>delt</i> calculation example of Case 4 signals at (a) 0° and (b) 90°. . . . .	111
A.3	Velocity profile from the LDV data for ACS specimen. . . . .	112
A.4	Velocity profile from the LDV data for SCS specimen. . . . .	112
A.5	Velocity profile based on values from Table A.1 . . . . .	113
A.6	RMS plots from LDV data at various excitation frequencies. . . . .	114
A.7	FWF with S0/A0+ interaction. . . . .	115
A.8	1D waveforms from theoretical and LDV data. . . . .	115
A.9	Waveforms comparison plots from S10, S12 signals of LDV data. . . . .	116
A.10	Dispersion curves (Vg Th) for ALS. . . . .	117
A.11	Frequency (vs) Amplitude plot of A0 mode for H case. . . . .	118
A.12	ALS FEM model:(a) Model with D1, (b) S0 mode, (c) A0 mode, (d) Change in wave pattern due to D1. . . . .	120
A.13	Models used in the GUI build up. . . . .	121
A.14	Directional sensitivity analysis. . . . .	121
A.15	Data extraction tab. . . . .	122
A.16	FBG reflectivity spectrum calculation tab. . . . .	123
A.17	Validation of GW signals. . . . .	124

## List of Publications

1. **Balasubramaniam, K.**, Sikdar, S., Ziaja, D., Jurek, M., Soman, R. and Malinowski, P., 2023. A global-local damage localization and quantification approach in composite structures using ultrasonic guided waves and active infrared thermography. *Smart Materials and Structures*, 32(3), p.035016, **Impact Factor and year: 4.131, 2023.**
2. **Balasubramaniam, K.**, Sikdar, S., Soman, R. and Malinowski, P., 2022. Multi step structural health monitoring approaches in debonding assessment in a sandwich honeycomb composite structure using ultrasonic guided waves. *Measurement*, 194, p.111057, **Impact Factor and year: 5.131, 2023.**
3. **Balasubramaniam, K.**, Fiborek, P., Ziaja, D., Jurek, M., Sawczak, M., Soman, R. and Malinowski, P.H., 2022. Global and local area inspection methods in damage detection of carbon fiber composite structures. *Measurement*, 187, p.110336, **Impact Factor and year: 5.131, 2023.**
4. **Balasubramaniam, K.**, Sikdar, S., Wandowski, T. and Malinowski, P.H., 2021. Ultrasonic guided wave-based debond identification in a GFRP plate with L-stiffener. *Smart Materials and Structures*, 31(1), p.015023, **Impact Factor and year: 4.131, 2023.**
5. **Balasubramaniam, K.**, Ziaja, D., Jurek, M., Fiborek, P. and Malinowski, P., 2021. Experimental and Numerical Analysis of Multiple Low-Velocity Impact Damages in a Glass Fibered Composite Structure. *Materials*, 14(23), p.7268, **Impact Factor and year: 3.748, 2023.**
6. **Balasubramaniam, K.**, Sikdar, S., Fiborek, P. and Malinowski, P.H., 2021. Ultrasonic guided wave signal based nondestructive testing of a bonded composite structure using piezoelectric transducers. *Signals*, 2(1), pp.13-24.
7. Soman, R., **Balasubramaniam, K.**, Golestani, A., Karpiński, M., Malinowski, P. and Ostachowicz, W., 2021. Actuator placement optimization

for guided waves based structural health monitoring using fibre Bragg grating sensors. *Smart Materials and Structures*, 30(12), p.125011, **Impact Factor and year: 4.131, 2023.**

8. Soman, R., **Balasubramaniam, K.**, Golestani, A., Karpiński, M. and Malinowski, P., 2020. A two-step guided waves based damage localization technique using optical fiber sensors. *Sensors*, 20(20), p.5804, **Impact Factor and year: 3.847, 2023.**
9. Soman, R., Kudela, P., **Balasubramaniam, K.**, Singh, S.K. and Malinowski, P., 2019. A study of sensor placement optimization problem for guided wave-based damage detection. *Sensors*, 19(8), p.1856, **Impact Factor and year: 3.847, 2023.**

#### **List of publications in book chapter**

1. **Balasubramaniam, K.**, Soman, R. and Malinowski, P., 2022, June. Development of GUI Based Tool for the Visualization of the FBG Spectrum Subjected to Guided Waves. In *European Workshop on Structural Health Monitoring: EWSHM 2022-Volume 3* (pp. 170-179). Cham: Springer International Publishing.
2. **Balasubramaniam, K.**, Fiborek, P., Sikdar, S. and Malinowski, P.H., 2021. Damage Assessment for a Sandwich-Like Panel Using Experimental and Numerical Analysis of Guided Waves. In *Advances in Non-destructive Evaluation: Proceedings of NDE 2019* (pp. 73-84). Springer Singapore.

#### **List of conference proceedings**

1. **Balasubramaniam, K.**, Soman, R., Wandowski, T., Malinowski, P and Ostachowicz, W., 2023, April. Through thickness inspection in various structures using ultrasonic wave coupling in an embedded fiber optical sensor. In *Proc.SPIE, Health Monitoring of Structural and Biological Systems XVII* (Vol. 12488, pp. 86-92). SPIE.
2. Soman, R., **Balasubramaniam, K.**, Grochowska, K., Lipinska, W., Malinowski, P and Ostachowicz, W., 2023, April. Investigating the use of polarization maintaining FBG sensors for guided waves based structural health monitoring. In *Proc.SPIE, Health Monitoring of Structural and Biological Systems XVII* (Vol. 12488, pp. 432-437). SPIE..

3. Soman, R., Sarbaz, S., **Balasubramaniam, K.**, Golestani, A., Karpinski, M., Wandowski, T., Malinowski, P and Ostachowicz, W., 2023, April. Investigating the effect of material on the coupling of guided wave in the optical fiber. In Proc.SPIE, Health Monitoring of Structural and Biological Systems XVII (Vol. 12488, pp. 393-399). SPIE.
4. **Balasubramaniam, K.**, Ostachowicz, W., Malinowski, P. and Soman, R., 2023, July. Numerical Guided Wave Analysis of an Isotropic Structure with Optical Fiber Bragg Grating Sensors. In 49th Annual Review of Progress in Quantitative Nondestructive Evaluation (Vol. 86595, p. V001T03A001). American Society of Mechanical Engineers.
5. **Balasubramaniam, K.**, Ziaja, D., Jurek, M., Soman, R. and Malinowski, P., 2022, April. Nondestructive analysis of composite structure subjected to impact damage conditions. In Proc.SPIE, Health Monitoring of Structural and Biological Systems XVI (Vol. 12048, pp. 123-131).
6. **Balasubramaniam, K.**, Soman, R. and Malinowski, P., 2022, April. Guided waves based damage detection based on quadrant area using optical fiber sensors. In Proc.SPIE, Health Monitoring of Structural and Biological Systems XVI (Vol. 12048, pp. 44-51).
7. **Balasubramaniam, K.**, Soman, R. and Malinowski, P., 2022. Study of Bond Length and Its Effect on Guided Waves Using Fiber Optic Sensors. In Physical Sciences Forum (Vol.4, No.1, p.8). Multidisciplinary Digital Publishing Institute
8. **Balasubramaniam, K.**, Fiborek, P. and Malinowski, P.H., 2021, March. Lamb waves based assessment of impact damage in multilayered CFRP plate. In Proc.SPIE, Health Monitoring of Structural and Biological Systems XV (Vol. 11593, pp. 128-137).
9. **Balasubramaniam, K.**, Wandowski, T. and Malinowski, P., 2021. Debonding Analysis of Composite Material Using Ultrasonic Wave-Based NDT Methods. STRUCTURAL HEALTH MONITORING 2021.
10. Soman, R., Golestani, A., **Balasubramaniam, K.**, Karpiński, M., Malinowski, P. and Ostachowicz, W., 2021, March. Application of ellipse and hyperbola methods for guided waves based structural health monitoring using fiber Bragg grating sensors. In Proc.SPIE, Health Monitoring of Structural and Biological Systems XV (Vol. 11593, pp. 65-73).
11. **Balasubramaniam, K.**, Wandowski, T. and Malinowski, P., 2019, July.

Approaches for localization of damage in composites using propagation of Lamb waves. In 9th ECCOMAS Thematic Conference on Smart Structures and Materials, SMART (Vol. 8).

12. **Balasubramaniam, K.**, Singh, S.K., Soman, R. and Malinowski, P.H., 2018, November. A study of electromechanical impedance and guided wave techniques for the sensitivity of sensors network in damage detection. In Proceedings of the 7th APWSHM Conference, Hong Kong, China (pp. 12-15).

### **Internships and research visits during study**

1. 7th International Summer School on Smart Materials and Structures, 16 July 2018 to 19 July 2018, Trento, Italy, organized by Prof. Daniele Zonta.
2. CertBond 1st summer school on Reliable roadmap for certification of bonded primary structures, 20 September 2021 to 22 September 2021, Trieste, Italy, organized by Prof. Chiara Bedon.
3. One week research work visit to Polytechnic Rzeszów, 27 September 2021 to 01 October 2021, organised by Prof. Michał Jurek and Prof. Dominika Ziaja
4. One day research work visit to Indian Institute of Technology, Chennai, 25 April 2022, organised by Prof. Krishnan Balasubramanian.
5. CISM coursework on Composite Manufacturing Processes: Analyses, Modelling, and Simulations, 2 May 2022 to 6 May 2022, Udine, Italy, organized by Prof. Wolfgang A. Wall.
6. 1st International Summer School on Clean Energy and Functional Materials (CenMAT) on Intelligent materials, diagnostics and structural analyses, 28 September 2022 to 07 October 2022, Gdańsk, Poland, organized by Prof. Magdalena Mieloszyk.
7. CertBond 2nd summer school on Sustainable composite bonded joints, 17 October 2022 to 19 October 2022, Guimaraes, Portugal, organized by Prof. José Sena Cruz.
8. Three days research work visit to the University of Warsaw, 08 February 2023 to 10 February 2023, organised by Prof. Michał Karpinski.

## Chapter 1

### Introduction to GW-based SHM systems

#### 1.1 Overview

A key factor in the certification of structures is structural integrity and reliability. The condition of the structures' structural reliability is a crucial component of their economic viability and safety. By using structural health monitoring (SHM) to check structures constantly, reliability is guaranteed [1]. The reliability of parts is an important aspect of the discussion in the aerospace, automotive, civil and other major engineering industries. The tragic bridge collapse of Mianus River Bridge, USA in 1983 could have been avoided if the bridges had been equipped with present-day online monitoring sensors. Similarly, the present automotive industries use a variety of sensors in continuous monitoring of the engine and other rotary parts to know about wear and tear. Due to various flight hours and heavy payloads, parts such as skin, stiffeners, beams, etc. are prone to structural damage in aeroplanes. Air crash investigations reveal that the skin part is subject to heavy loads from atmospheric pressure conditions [2]. Thus, the online monitoring of these structural components in various functional engineering fields is much needed in saving precious lives and valuable cargo.

In aerospace, automotive, and other high-tech industries, safety, reliability and continuous maintenance are critical factors [3]. The amount of research and development in these industries is growing rapidly with sophisticated instruments and ideas/techniques. Engineering structures sustain fatigue damage [4], barely visible impact damage (BVID) [5], and other types of damage after routine/continuous workload [1]. Damage may also occur during the manufacturing or in the maintenance stage. As a result, identifying any form of structural damage is crucial before any fatal incident occurs. Recent technological advances help in structural analysis and damage assessment. A regular inspec-

tion reduces the possibility of overlooking critical damage. SHM techniques are advanced nondestructive testing (NDT) techniques involving online and continuous monitoring of engineering structures. To improve structural reliability and life cycle management, such online monitoring is necessary to get more information about the varying structural changes [1]. The SHM process includes continuous acquisition, validation, and analysis of data collected by sensors installed permanently in the structure [3]. Identification of the features from the obtained monitoring data (i.e., responses based on any damage-sensitive feature like for example vibration-based amplitude or frequency) is necessary to classify the healthy and damaged state of the part/structure. Reliability and reduced costs make the SHM a common solution in structural analysis.

## 1.2 Basics of SHM systems

To detect the presence or growth of damage, SHM techniques involve extracting damage-sensitive parameters, implementing a processing strategy, observing/visualizing the results, and then coming to a decision. The SHM's primary goal is to provide the structure operator with a continuous real-time assessment of the structure's condition and to ensure a high level of safety and structural integrity [6]. The development of a reliable SHM system helps facilitate the diagnosis and analysis of the prognosis of structures.

SHM is a process of monitoring structures for diagnostic and prognostic analysis [3]. The process involves the observation of various parameters (i.e temperature, strain, amplitude, charges, etc) obtained continuously to monitor the changes in the geometric and material properties of the structure. SHM systems require the use of sensors and actuators to validate structural integrity. Apart from that, the process involves the selection of the sensor types, sensor localization optimization, frequency and excitation mode selection, data acquisition and receiver (DAQ) equipment selection etc. The systems also require data processing and transmission devices, higher computational power and reliable electrical and mechanical connections for monitoring [6]. The SHM systems are usually compared with the human nervous systems which sense the pain and report it to the brain [4]. Similarly, SHM systems are capable of sensing damage from any part of the structure and reports the data to the data storage device.

SHM helps to reduce the cost and time with continuous monitoring using sensors. SHM has the following advantages: it doesn't require access to the inspection area as it can be monitored online [7], provides safe inspection



of structures, can be automated with no human interference, helps to quickly repair larger structures effectively and can interrogate many locations/regions. There are various examples, from bridge monitoring [8] to aerospace structures [9] inspections performed using SHM systems. SHM systems are classified into active and passive based on their usage and measurement types. Passive SHM does not interact with the structures; it merely "listens" to them. Active SHM can be used whenever necessary, in which case structures are first excited using actuators in predetermined ways and then questioned by examining the structural reactions. An exemplary active SHM system is shown in Figure 1.1.

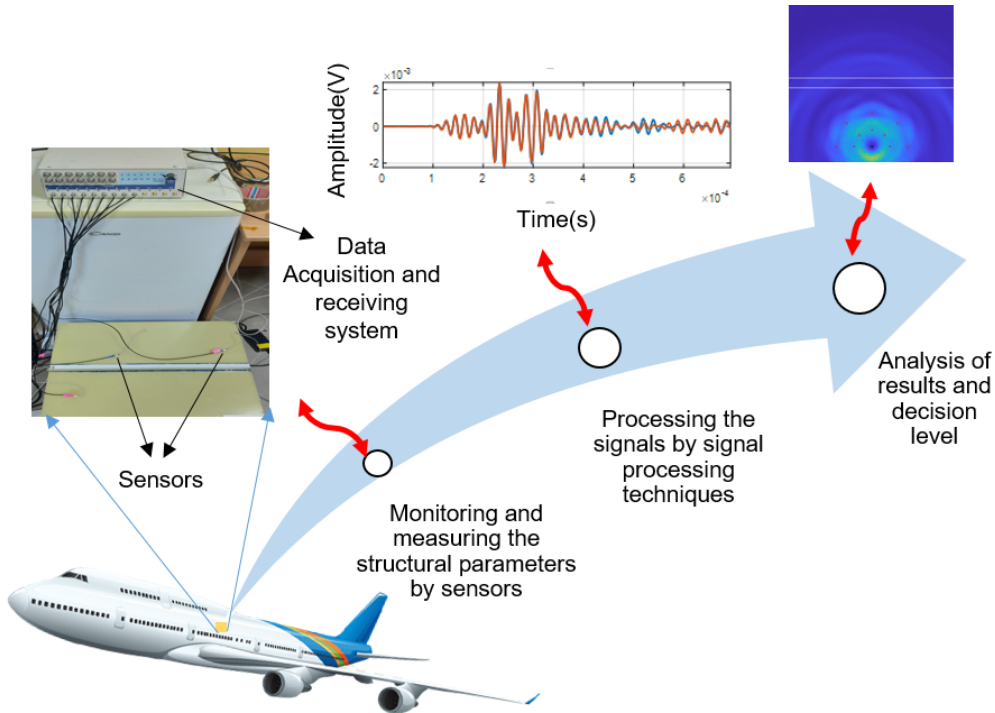


Figure 1.1: SHM systems overview: exemplary aeronautical application.

SHM methods are classified mainly based on the monitored quantity such as vibration, strain, guided waves (GW), acoustic emission, electromechanical impedance, etc. The research in this thesis focuses on the active GW-based SHM system and various types of damage that the system can detect effectively. GW in this system are excited using a piezoelectric transducer (PZT) and is detected with PZT, laser Doppler vibrometer (LDV), and fiber Bragg grating (FBG) sensors. The following are the most crucial reasons to use GW-SHM: high sensitivity to low-level damage [1], the possibility of non-contact, active sensing, and the potential to localize damage are very likely.

### 1.2.1 PZT and FBG sensors

PZTs as shown in Figure 1.2 are low-cost, lightweight, thin and can easily be integrated into any structure. PZTs can excite GW when voltage is applied [10], thereby generating continuous mechanical energy waves (due to strain) that propagate on the structures [3] in which they are attached. PZTs can also sense the GW in a reverse way from mechanical energy to voltage. A good signal interpretation method is required to process the data obtained from these PZT sensors [5]. PZTs can be arranged in a variety of arrangements or optimally placed, forming PZT networks or sensor networks for SHM systems to function.

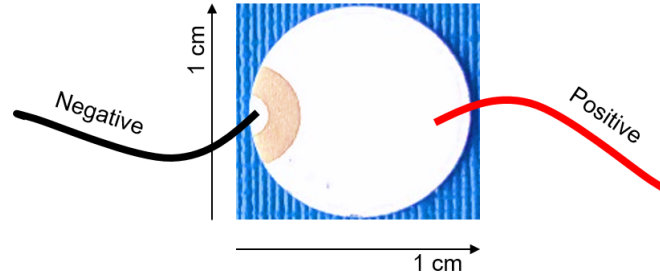


Figure 1.2: PZT used in the GW measurements.

FBG sensors are increasingly used in SHM studies of aerospace, automotive, and civil structures nowadays. The ability to easily embed, higher sensitivity, low electromagnetic noise, lightweight nature, and generation of a higher signal sampling ratio (when coupled with a photodetector) in GW detection are significant advantages of FBG over other sensors [11]. The FBG is a narrow band wavelength filter embedded/written in an optical fiber (shown in Figure 1.3) that transmits the other wavelengths while reflecting a specific narrow bandwidth [12] of light out of the total light input to the fiber, as shown in Figure 1.4. The reflection spectrum is usually centred along with a wavelength termed the Bragg wavelength ( $\lambda_B$ ). The refractive index of the FBG core is perturbed by the grating of the fiber which results in light reflections. The  $\lambda_B$  depends on the grating period and effective refractive index [12].

When any form of stress/strain is applied to the FBG (in this research work strain due to the GW excitation),  $\lambda_B$  shifts as shown in Figure 1.5. Based on the shift in the wavelength, the guided wave is sensed (healthy and damaged states get identified). Thus, FBG is capable of sensing the GW via changes in the reflected light spectrum caused due to the varying strain (GW sensed as strain). To distinguish optical return signals from a grating array, the optical

fiber system employs a wavelength-division multiplex (WDM) interrogation approach. The WDM was used to find the wavelength shift caused by strain in the Bragg-grating reflection spectra. There is evidence that this detection method can pick up very small dynamic stresses [3]. In recent times, the edge reflection-based technique [13] has been used to capture GW using the FBG. More details about the technique are mentioned in subsection 2.3.3. The bonding of the FBG to the structure is termed direct bonding [13] and is a tried and tested technique. The other technique is remote bonding, in which the FBG is kept free and only the optical fiber is bonded to the structure. More details on FBG GW sensing, direct and remote bonding configuration can be found in sections 6.3, 6.4 and chapter 7 respectively.

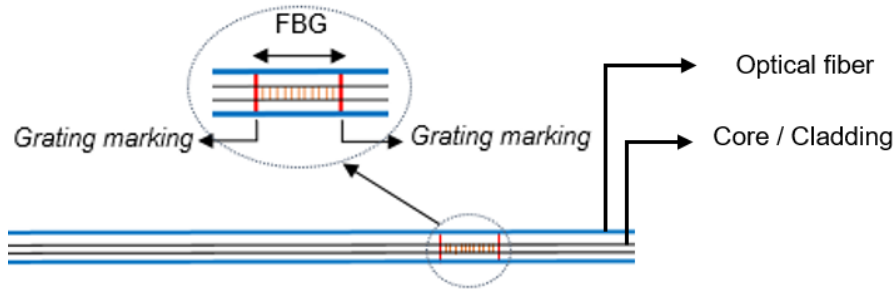


Figure 1.3: Schematic representation: optical fiber and FBG.

### 1.3 Elastic wave propagation in plates

Following the research of eminent scientists in the areas of waves in solid media over the course of a century, the elastic wave propagation in solid plates has evolved into a completely new shape. Many scientists like Rayleigh, Lamb, and Love did profound work in the areas of wave motions, and Rayleigh waves, Lamb waves (LW) and Love waves were named after their works. The following are the major wave motions that are studied in detail.

#### 1.3.1 Elastic wave motion: Rayleigh waves

Rayleigh's waves [14] are one type of surface wave that travels along the free surface of the solid medium (considered to be semi-infinite as shown in Figure 1.6). These waves are sensitive to smaller surface defects, such as cracks [15], as they could penetrate solid media [3]. In this case, the wave particle's magnitude reduces exponentially with respect to its surface movement (change in distance). The movement of the particles in these waves is confined within the vertical surface, and their motion path resembles an elliptical rotation [16].

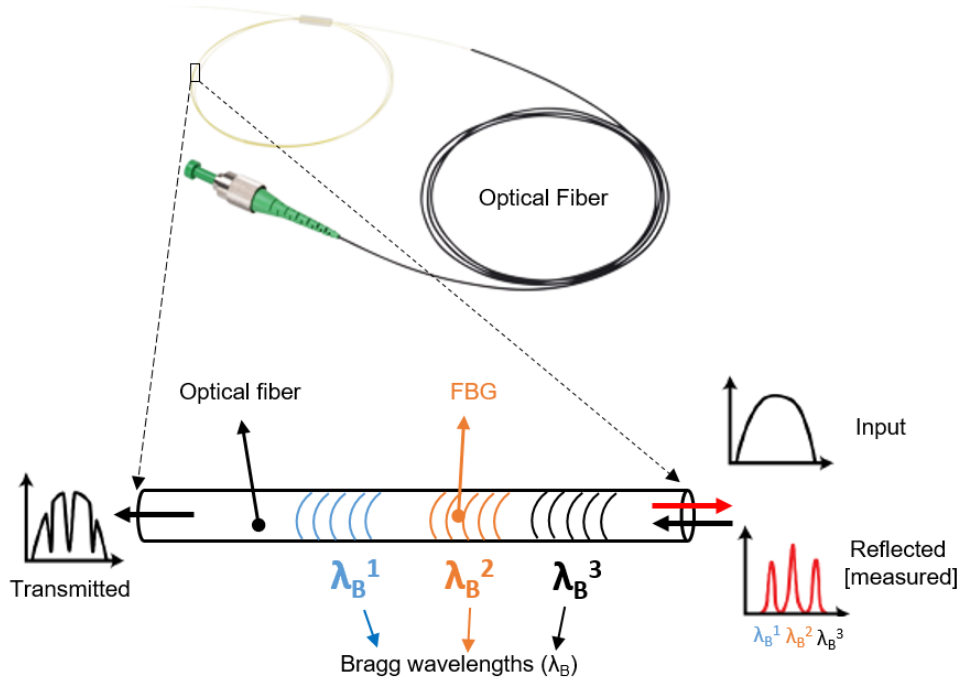


Figure 1.4: FBG used in the GW measurements.

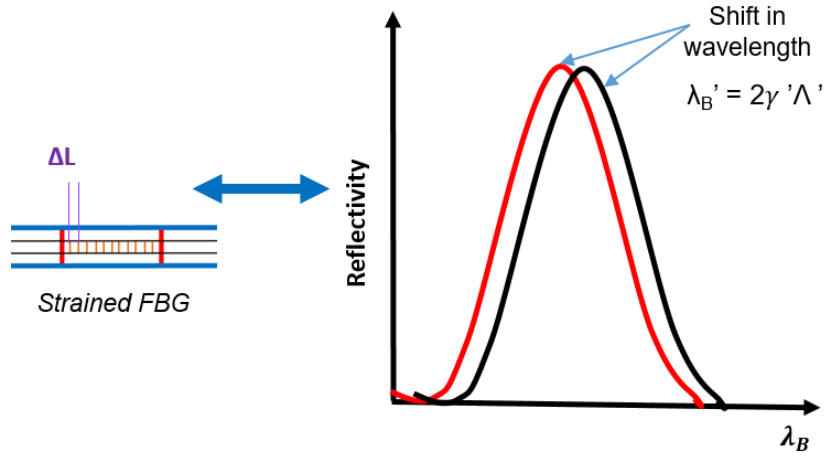


Figure 1.5: Exemplary FBG's response as a function of strain.

### 1.3.2 Elastic wave motion: Love waves

Love waves are also surface waves and were first studied by Augustus Love [17]. The movement of the Love wave particles is in a direction parallel to the medium's surface as shown in Figure 1.7. The particle motion in Love waves is perpendicular to the direction of wave propagation and parallel to the surface of the medium. Their wave amplitude decreases quickly with depth, just like Rayleigh waves do [16].

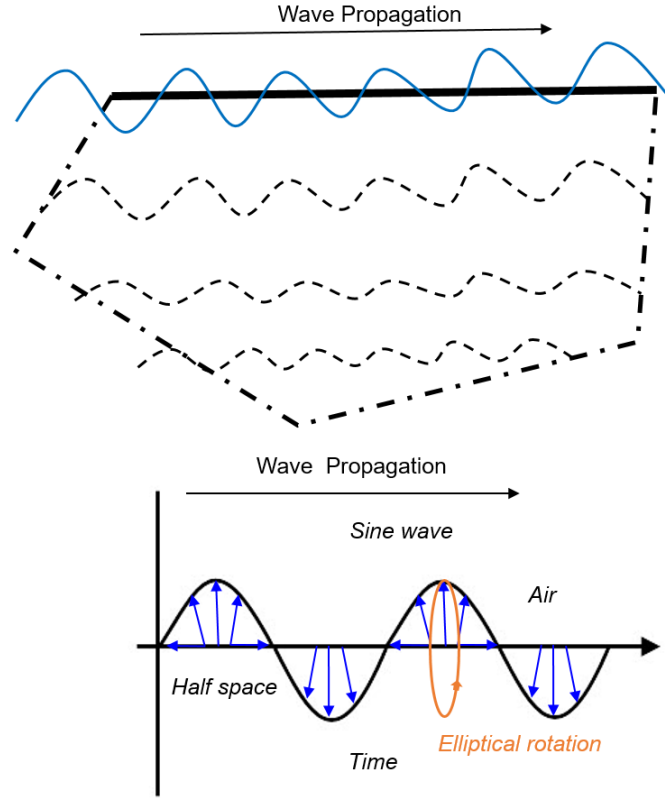


Figure 1.6: Rayleigh waves on a semi-infinite medium.

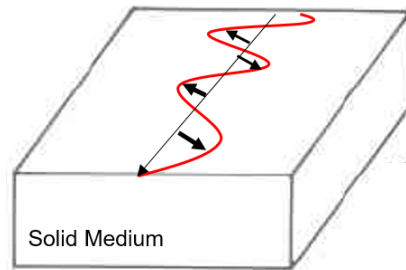


Figure 1.7: Love waves in a solid medium.

### 1.3.3 Elastic wave motion: Lamb waves

The theory of LW was studied in detail by Horace Lamb [18]. They are also termed GWs as they travel freely guided along the upper and lower layers of the medium with the same magnitude. The movement of the LW can be in longitudinal and transverse directions on plates. They vary depending on the media in which they propagate. LW propagation modes are mostly antisymmetric (A) and symmetrical (S) in plate-like structures, as shown in Figure 1.8.

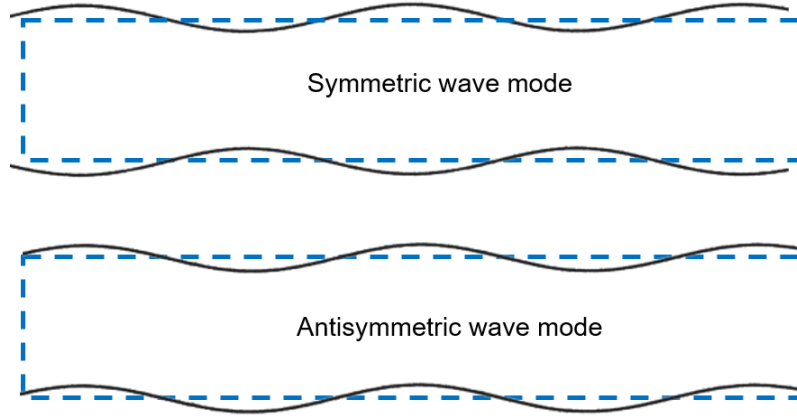


Figure 1.8: Fundamental LW modes in a thin plate.

The Anti-symmetric wave modes have opposite displacements on either side of the centerline (refer Figure 1.8), while symmetric LW has identical displacements on both sides of the centerline. These surface waves are highly dispersive in nature and depend on the thickness of the structure in which they move, the type of structure (material), the excitation frequency and the angle of propagation (in the case of multi-layered composites). LW has a long propagation distance and a low attenuation (loss of amplitude over distance), making it the primary choice of SHM engineers who deal with ultrasonic investigations to monitor huge and complicated structures.

The reflections of the LW along its propagation path assist in identifying the irregularity (damage) in the structure [19]. LW are effective at detecting damage through thickness and are capable of detecting multiple damages in larger structures [20]. Equation 1.1 provides a general description of LW in the homogeneous mediums, as mentioned in [1]. Equation 1.1 can be simplified into Equation 1.2  $S_i$  ( $i=0,1,2,\dots$ ) symmetric mode and Equation 1.3  $A_i$  ( $i=0,1,2,\dots$ ) anti-symmetric mode, based on the symmetric and antisymmetric properties of LW over a medium.

$$\frac{\tan(qh)}{\tan(ph)} = \frac{4k^2qp\mu}{(\lambda k^2 + \lambda p^2 + 2\mu p^2)(k^2 - q^2)}$$

$$q^2 = \frac{\omega^2}{c_T^2} - k^2$$

$$p^2 = \frac{\omega^2}{c_L^2} - k^2$$

$$\omega = 2\pi f$$
(1.1)

$$\frac{\tan(qh)}{\tan(ph)} = -\frac{4k^2qp}{(k^2 - q^2)^2} \quad (1.2)$$

$$\frac{\tan(qh)}{\tan(ph)} = -\frac{(k^2 - q^2)^2}{4k^2qp} \quad (1.3)$$

Where:  $h$  is homogeneous media (e.g., solid plate) half thickness;  $k$  is wavenumber;  $\lambda$  and  $\mu$  are the elastic constants of the material;  $\omega$  is the angular frequency;  $C_T$  shear bulk wave velocity;  $C_L$  longitudinal bulk wave velocity;  $f$  is the frequency.

#### 1.3.4 Elastic wave motion: SH waves

The propagation of shear horizontal (SH) waves is transverse (Figure 1.9) in nature and the shear wave particles move in a direction of in-plane w.r.t interface of the medium in which it propagates. SH waves are similar to LW and are also one type of GW, as they possess A and S modes [21] and the relative magnitude of such waves does not change on both sides of the structure [22].

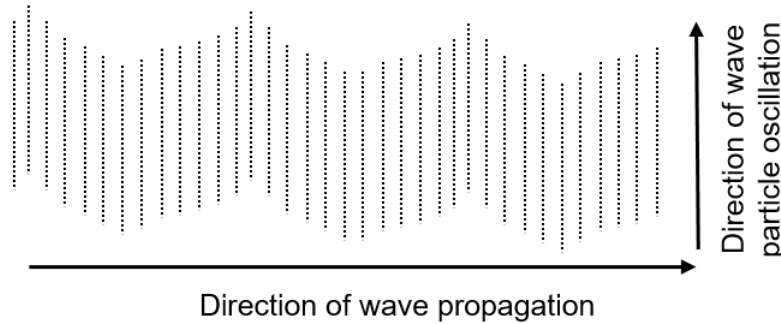


Figure 1.9: SH waves on a solid media.

#### 1.4 Analysis of structures using GW

GW are elastic perturbations that propagate along the free boundaries of a solid structure, adversely affecting the modes of propagation of GW [5]. GW has the ability to travel a greater distance through surfaces with little attenuation and aids in identifying damage through the phenomena of wave interaction and reflection [23]. Most GWs are dispersive in nature (Rayleigh waves and SH waves are exclusive) due to the varying velocities and other characteristics such as the geometrical and material properties of the medium in which

they propagate [3]. A change from one mode of propagation (e.g S) to another (e.g A) is referred to as a mode conversion in guided wave studies. This may happen if the waveguide's boundary conditions change. The particular mode conversion that takes place is determined by the wave's wavelength or geometry of the structure. Thus, they are characterized predominantly on the basis of the frequency, period, wavelength, wavenumber, and speed and amplitude/ displacement of the particles [4]. Methods such as pitch-catch and pulse-echo (refer to Figure 1.10) are frequently used in GW-NDT and SHM fields to examine and assess materials and structures for flaws or damage.

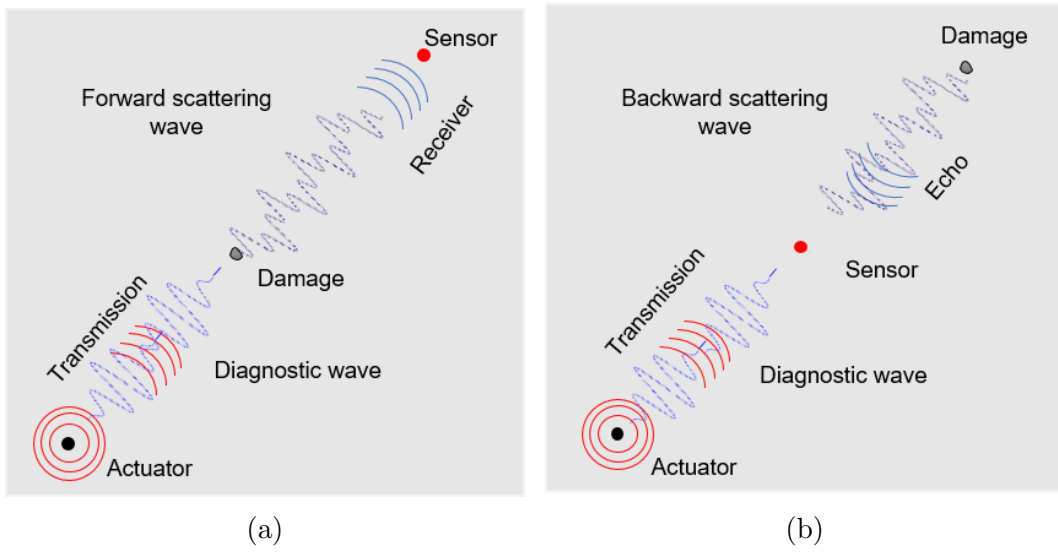


Figure 1.10: GW measuring systems: (a) Pitch catch, (b) Pulse echo.

In the pitch-catch method (Figure 1.10a), the GW signals are excited by the actuator (PZT in this research) and sensed by the sensor (PZT or LDV or FBG) on the other side. However, in the pulse-echo method, the actuator/sensor is mostly the same (or present on the same side) as shown in Figure 1.10b. The research thesis employs both pitch-catch and pulse-echo systems for damage identification and specifically examines the LW-type GW in detail, which will be referred to as GW in subsequent chapters.



## **Chapter 2**

### **State of the art in GW studies**

This chapter provides a brief survey of the literature on GW inspection studies, SHM techniques, NDT-based approaches, and SHM systems. A few examples created using SHM GW approaches are also included in this chapter as a part of understanding more of the literature works with an experimental approach point of view.

#### **2.1 SHM and NDE methods**

The NDT or NDE (nondestructive evaluation) based applications use some similar approaches to SHM-based techniques. Methods like analysis, identification of the damage and discussions fall into a similar category of interests (Figure 2.1) with both the techniques [24]. But, NDT techniques are mostly offline-based and need trained technicians to perform the inspection. SHM systems, on the other hand, are mostly online-based inspections. SHM is mostly a global area inspection and monitoring method, which analyses the entire area of the structure effectively. Whereas, on the other hand, NDE techniques are mostly local area inspection methods that check region-by-region of the large structure [25]. As said earlier, there is a correlation between the NDE and SHM methods but not all the NDE methods can be used or compared on par with SHM methods [26]. Additional details about the notable NDE methods are provided in the list that follows, along with a determination of whether they could be applied to SHM techniques.

Visual inspection requires higher operator skills and is not time effective. The technique is the most common form of testing the structures and is used as a standard practice in the inspection process [1]. This technique requires inspection of the structure with the operator's naked eyes (Figure 2.2) and then using other techniques like microscopes, magnification lenses, etc. This tech-

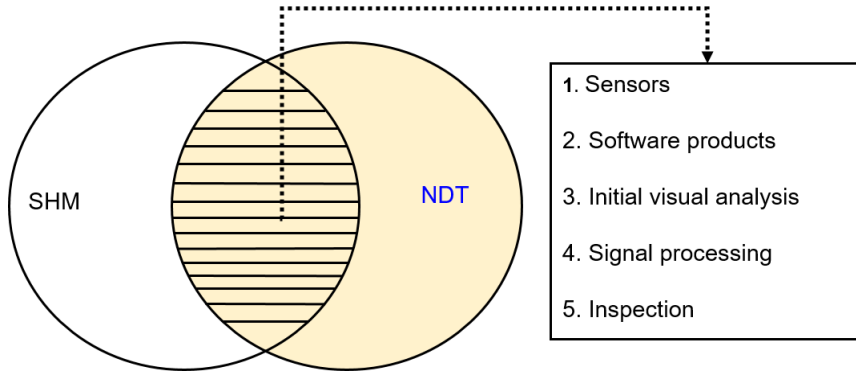


Figure 2.1: Comparison of SHM and NDT techniques.

nique cannot be incorporated into SHM methods as it is a laborious periodic inspection process.



Figure 2.2: Visual inspection done at IMP PAN.

Ultrasound inspection techniques (UT) help to investigate the thickness of the specimen or to characterize the structure internally. The frequency range that the UT technique uses ranges between 500 kHz to 30 MHz respectively. This works on similar techniques of pulse-echo as shown in Figure 1.10b and is effective in scanning the structures w.r.t thickness. They can be used on plastics, metals, polymers, additively manufactured specimens, etc. The disadvantage is again this method is a local area inspection technique that requires trained technicians, difficult to inspect complex geometries, calibration of the equipment w.r.t material being inspected, and has a higher purchase cost.

Infrared thermography (IRT) based inspection techniques are quite popular and require less processing time to inspect the specimens [27]. The IRT captures the radiation emitted by the object/ specimen and produces the images as thermograms [4] as shown in Figure 2.3. Similar to the UT process, it's

also a local area NDE method and requires trained technicians and periodical inspection.

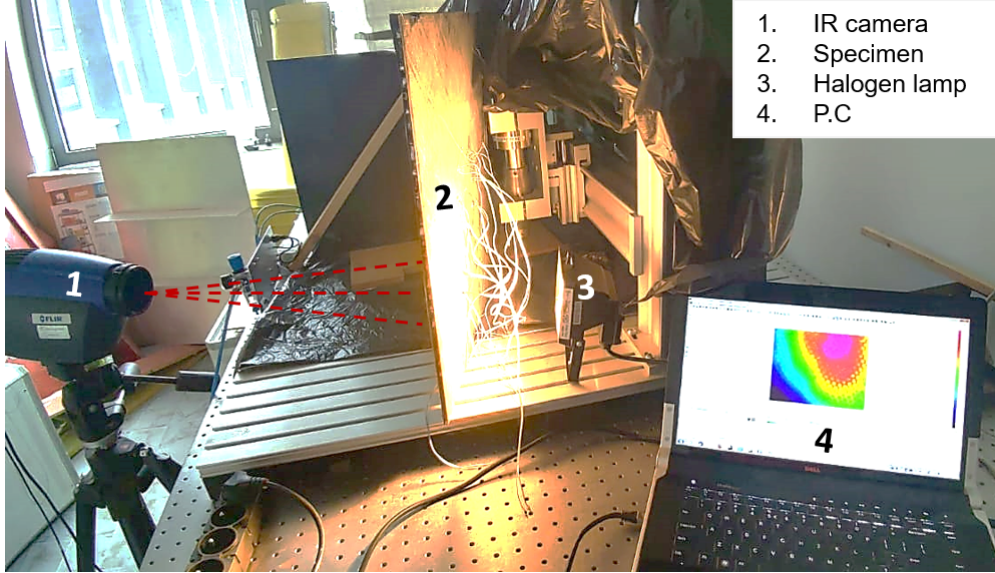


Figure 2.3: Infrared thermography experimental setup at IMP PAN.

The electromechanical impedance approach is based on electrical parameter measurements of a PZT connected to the structure under investigation [28]. Mechanical resonances of the host structure can be seen in the electrical properties of the piezoelectric transducer as a result of the electromechanical connection between the two components. This method allows for the recording and analysis of electrical properties such as impedance, admittance, their actual components (resistance and conductance), and their imaginary components (reactance and susceptance). According to the literature, imaginary electrical characteristics are used to diagnose the transducer itself or to monitor the bonding layer between it and the structure [29], whereas real electrical parameters are used to monitor the structure. Reactance, for instance, was used in [30] as a measure to detect transducer debonding, whereas resistance was used to evaluate the structure. Resistance and susceptance, however, were employed in [31] to identify sensor flaws.

Acoustic emission-based inspection technique comes under passive monitoring of the structure [32]. In this type of passive monitoring the testing works when there occurs sudden changes in the material properties due to stress/strain [33]. The method is highly sensitive, with real-time monitoring, and rapid detection of damage. But the major drawback of the method is that it requires the stress signals to be obtained from the material itself as shown in Figure 2.4 and thus

a constant or at least a periodic change in the material properties are required for the inspection process to function. This thesis work focuses on the online and active monitoring of the structures and thus inspection of the structures using acoustic emission is not considered.

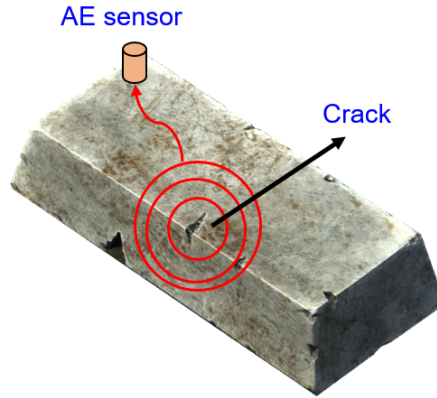


Figure 2.4: An exemplary acoustic emission-based monitoring.

SHM using GW techniques are online-based monitoring techniques. It employs waves from the excitation source (example: PZT-based actuators) that can propagate across the structure and can obtain the reflected signals from the damages via the sensor (example: PZT, LDV and FBG) to determine the state of the structure. The GW technique uses structure as a waveguide and thus can help in long-range inspection and this helps to identify damage located at a far location too. This proves to be a major advantage against the conventional NDE or UT techniques which require close-range inspection. An example of one such SHM GW monitoring method using DAQR in a CRFP specimen is shown in Figure 2.5. SHM techniques to continuously monitor strain (e.g., via FBG), monitor temperature, and vibration (e.g., via PZT) are also used in the industries. In this thesis, GW analysis measurements with LDV (vibration-based), PZT (vibration-based), and FBG (strain-based) sensors are used to monitor, detect and localize various kinds of damage in a variety of structures.

## 2.2 GW-based SHM methods

A detailed literature survey was conducted to get to know the state-of-the-art damage imaging algorithms and their pros and cons. Ultrasonic GW propagation-based SHM has demonstrated its ability to detect and localize structural defects [34]. GW has been widely used in detecting impact cracks [25], debonding analysis [35], delamination detection [20] etc.

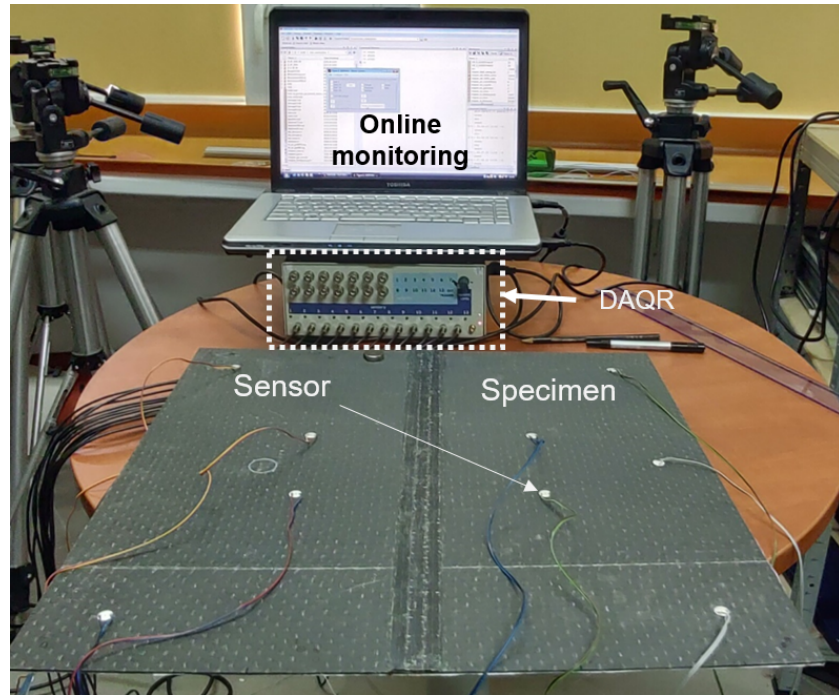


Figure 2.5: GW-based SHM monitoring using DAQR setup at IMP PAN.

### 2.2.1 Damage detection using GW methods

Researchers [36] examined the SHM GW-based amplitude value changes at the impact regions in carbon fiber reinforced polymer (CFRP) structures for damage identification. Boettcher et al. [37] used GW to assess the effect of energy dissipation in structures. Holst et al. [38] used changes in wavelet energy [39] and velocity variations to analyze CFRP structures (CFRPS) subjected to impact damage. Teflon inserts in plates were studied by [40] using GW zero group velocity differences. Lugovtsova et al. [41] investigated delamination in an aluminium-carbon fiber structure using GW-based wavenumber mapping. Munian et al. investigated GW scattering and reflection in CFRPS with impact delamination [42]. The GW-based time of flight (TOF) method was used to compare numerical to experimental damage results [43].

The duration it takes for a GW to move from its source (actuator) to its receiver (sensor) is known as the TOF. Numerous elements, including the structure's geometry, material properties, and the existence of damage, can influence the TOF [44]. TOF is widely used in many NDT applications such as ultrasound (i.e ultrasonic), LDV, and phased array. GW can travel over larger distances on the structure and helps in damage identification studies [4]. The change in the TOF of the waves aids in determining the damage by comparing it to



the reference signals (healthy signals) as shown in Figure 2.6. More details about the TOF method are shown in section 4.1, Equation 4.1 and Figure 4.3 in chapter 4.

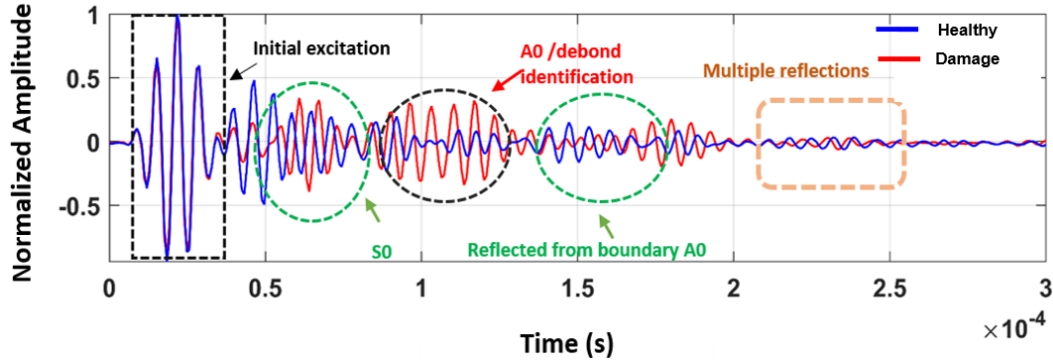


Figure 2.6: Exemplary TOF of GW modes.

By subjecting CFRPS to impact damage, Lambinet [45], Burkov [46], and Hameed et al. [47] investigated GW-based signal velocity and energy (amplitude), amplitude differences, and continuous wavelet transforms. In order to detect the impacts, the GW reflection coefficient, amplitude changes, and velocity differences were recorded in CFRP plates [48] as a damage index criterion. Lugovtsova et al. investigated the use of local and instantaneous wave numbers in distinguishing damage in CFRPS [41]. Sikdar et al. [49] combined the GW method and IRT-NDT methods in debond localization in bonded CFRPS.

### 2.2.2 Damage localization using GW methods

Mustapha et al. [50] used the time-reversal method to investigate similar finite element method (FEM) and experimental combinations in sandwich honeycomb composite structure (SCS) panels. Eckstein et al. [51] investigated multiple debonding delaminations caused by impact damage in a CFRP door panel using a tomography-based reconstruction algorithm for the probabilistic inspection of damage (RAPID) technique. Yue et al. [52] used tomography-based damage index calculations to analyze CFRP plates with circular sensor arrays and plot the localization. Zima [53] investigated structural cracks using a damage index (DI) based on wave reflections.

Segers et al. [54] used a GW-based nonlinear filtering method to localize damage in CFRPS, Sha et al. [55] used wavelet analysis to assess the damage, and Hervin et al. [56] looked into GW scattering and entrapment in the impact

damage crack zone of CFRPS. Dafydd et al. [48] found that the amplitude of the GW was directly proportional to the severity of the damage. Multiple damages were localized in a composite structure using an elliptical-based code [57]. Ziaja et al. [58] used an Artificial Neural Network-based amplitude difference formulation to show the change in the DI by comparing the healthy and damaged states of GW signals of steel structures. In the damage localization of CFRP structures, Azura et al. [59] used the RAPID. Damaged CFRP structures were studied and localized using delay sum, signal differences, RAPID, and Voronoi-based algorithms [60]. Impact damage on GFRP was analyzed using wavelet packet transform [61]. Alnuaimi et al. [62] performed impact damage sensing on glass fiber reinforced polymer (GFRP) plates using fast Fourier transform peak analysis, nonlinear sideband peak variations, and TOF analysis. The impact effects in the CFRPS were investigated using GW amplitude variation due to defect size, fiber breakage and a linear PZT network by Heesch et al. [19]. Zhang et al. [63] examined the GFRP structure (GFRPS) at various stages of impact using differences in mode conversion behaviour. The signal-to-noise ratio DI method and the probabilistic damage detection algorithm RAPID was used to compare BVID identification [64].

The wave filtering approach [65], DI-based on signal difference correlation coefficient [66], and probabilistic reconstruction approaches [67] were used for debond localization. The wave filtering approach, which requires more computation time, identified the debond based on the damage input from the full wavefield (FWF) GW studies (where the GW from propagation till reflection could be seen in animation 3D view rather than 1D GW signal view). De Luca et al. [68] investigated FWF-based debond analysis on a composite winglet. Sikdar et al. localized debonding in sandwich structures using signal difference based on the modal amplitude area method [69]. A similar localization scheme is used in [70] to locate the debond using linearly placed sensor networks. The debond analysis using the signal difference-based coefficient and probabilistic methods can identify damage only within the sensor network as their path coverage is significantly less.

### 2.2.3 Sensor optimization in GW studies

Another important aspect of SHM using GW is sensor optimization (i.e., placements of the sensors) for sensing the GW in structures. Previous research in GW analysis used an analytical approach to determine sensor placement [53]. Philibert et al. [71] investigated GFRP I-joint stiffener assembly using PZT arranged linearly. Fendzi et al. [72] investigated a genetic algorithm that was not

dependent on damage localization. The sensors were arranged in a  $2 \times 3$ -row column matrix with equal intervals. A method known as the Multiple Signal Classification (MUSIC) algorithm was studied in detail by Zuo et al. [73] with a phase array sensor network. Soman et al. used a genetic algorithm for PZT optimization in structures [74] and was then tested to study aluminium Nomex composite structure (ACS) in [75]. Nomex<sup>®</sup> is a heat-resistant fiber material and is largely used by fire fighters. The signal difference coefficient method is further improved to study breathing debonds in CFRP stiffener plates [76] with a linear array of equally spaced sensors. Memmolo et al. [77] used the probabilistic image reconstruction localization algorithm in studying stiffener-attached composite structures. Zima et al. [78] proposed an elliptical-based algorithm for crack size estimation from closely arranged transducer arrangements. Thus, sensor optimization is a key to localizing the damages [6]. The sensor paths should cover most of the specimen regions to continuously monitor for any kind of damage.

#### **2.2.4 Reasons for GW signals variation**

The changes in the GW signals, amplitude variation, velocity changes etc are caused by the presence of any kind of damage (i.e., delamination, debond, impact damage, etc). The other reason for the changes could be varying environmental conditions which include a change in temperature, more loads on top of the specimen, vibrational effects, water impregnation, etc to name a few [24]. Temperature effects (be it hot or cold) is one main reason for such changes in the GW signals. This is because GW signals are extremely sensitive to temperature effects and structures that are in constant exposure to varying temperature conditions can be monitored using SHM-GW systems for lifetime predictability assessments [79]. Better signal processing methods are needed to address these issues.

#### **2.2.5 Temperature effects studied using GW**

Nan Yue et al. analyzed CFRPS with impact damage from coupon to sub-component level [80] at varying temperatures and localized the damage using the GW imaging-based delay sum TOF method. Michaels et al. analyzed aluminium and composite samples with a sparse array network of PZT arrangement at varying temperature conditions using delay and sum and minimum variance imaging schemes to localize the damages [79]. Sikdar et al. studied debonding in an SCS at ambient temperature conditions using a baseline-induced mapping algorithm [66]. Li et al. [81] also analyzed temperature-



bounded aluminium structures (ALS). Lambinet et al. [60] studied composite structure with Teflon inserts [82] using a minimal intersection score algorithm subjected to ambient temperature conditions. Abbas et al. [83] investigated numerical and experimental methods for detecting damage in structures exposed to varying temperatures and other factors.

One example to show the GWs sensitivity to harsh environmental conditions is done by subjecting a CFRPS to varying temperature conditions. To perform the temperature based/dependent study the pristine CFRPS is kept in a temperature-controlled oven setup as shown in Figure 2.7 along with the glued 8 optimized PZTs. The oven can take a sample size up to 300 mm × 300 mm and can go up to a maximum temperature of 240°C. The industrial commercial temperature conditions used in this investigation ranged from 25° C (T1), 35°C (T2) till 105° C (T9). Additionally, the maker cautions against using PZTs after 160° C [84].

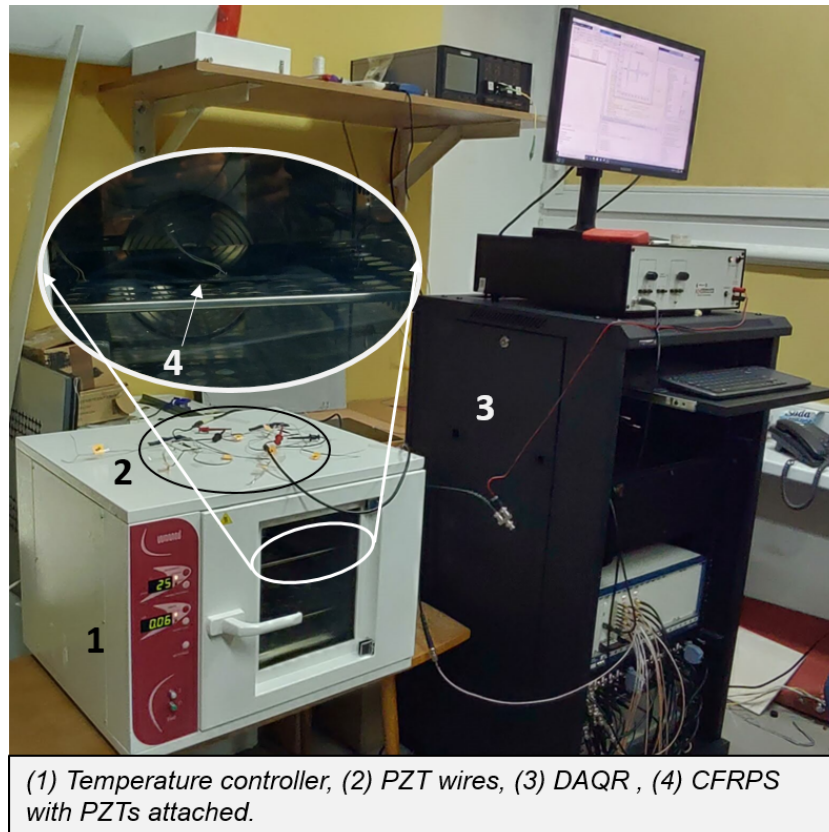


Figure 2.7: Temperature effects study using PZT network at IMP PAN.

Following the completion of the healthy temperature-based study on the structure, impact-based damage is created. CFRPS suffered intralaminar crack

damage [85] as a result of the impact energy of 33 J. The steel ball hammer hit method, as shown in [86], was used to introduce a 10 mm damage at (centre coordinate: 100 mm, 60.35 mm). Figure 2.8 depicts the damaged structure after the impact with optimized (using SenOPT [87]) PZT placements and a cross-sectional view of the CFRPS (for explanatory purposes only). The research is then carried out on CFRPS damaged state.

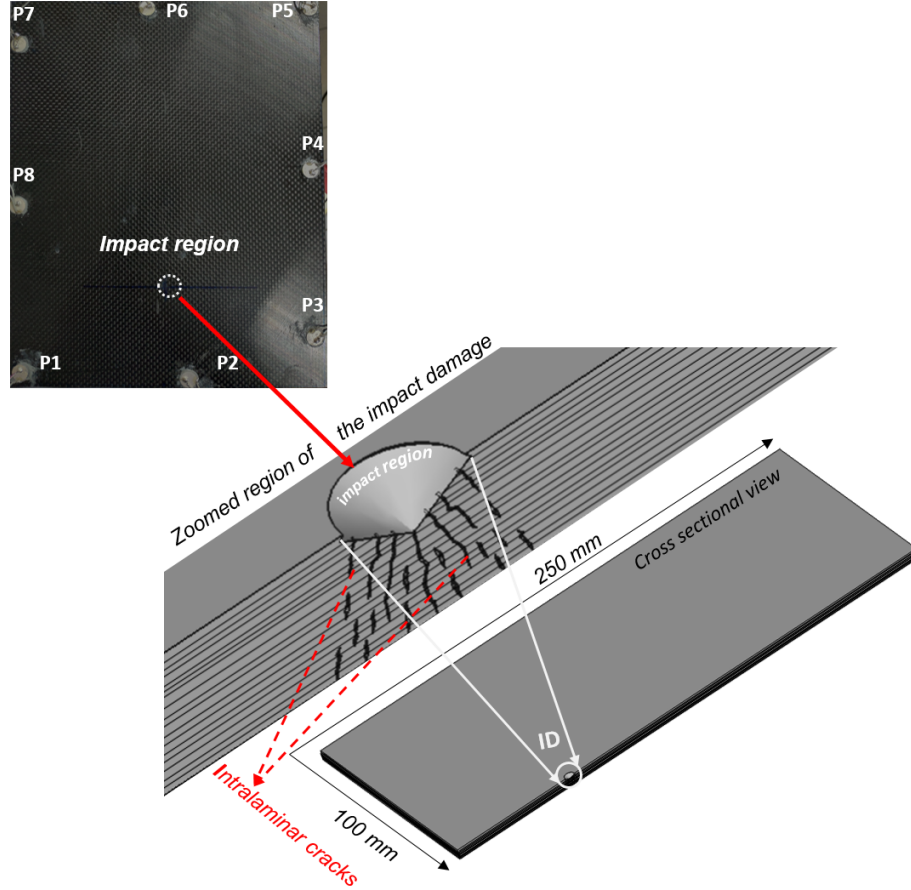


Figure 2.8: PZT positioned for SHM monitoring of CFRPS.

The GW TOF is related to temperature effects [24], as the TOF difference is directly proportional to the temperature difference and drops linearly (with rising temperature). A parametric-based graph study was performed on the healthy and damaged specimen. For this study, the peaks of the S0 mode (fundamental symmetric GW mode) are picked up as shown in Figures 2.9 and 2.10. As shown in Figure 2.11 for both the healthy and damaged sample at an exemplary 150 kHz, it was discovered that a change in the GW amplitude (decreasing trend) happens with an increase in temperature (in most of the curves). The amplitude values of crest peaks in GW signals differ significantly

between the damaged (Figure 2.11b) and healthy specimens upon closer inspection (Figure 2.11a), indicating possible structural changes in the damaged specimen.

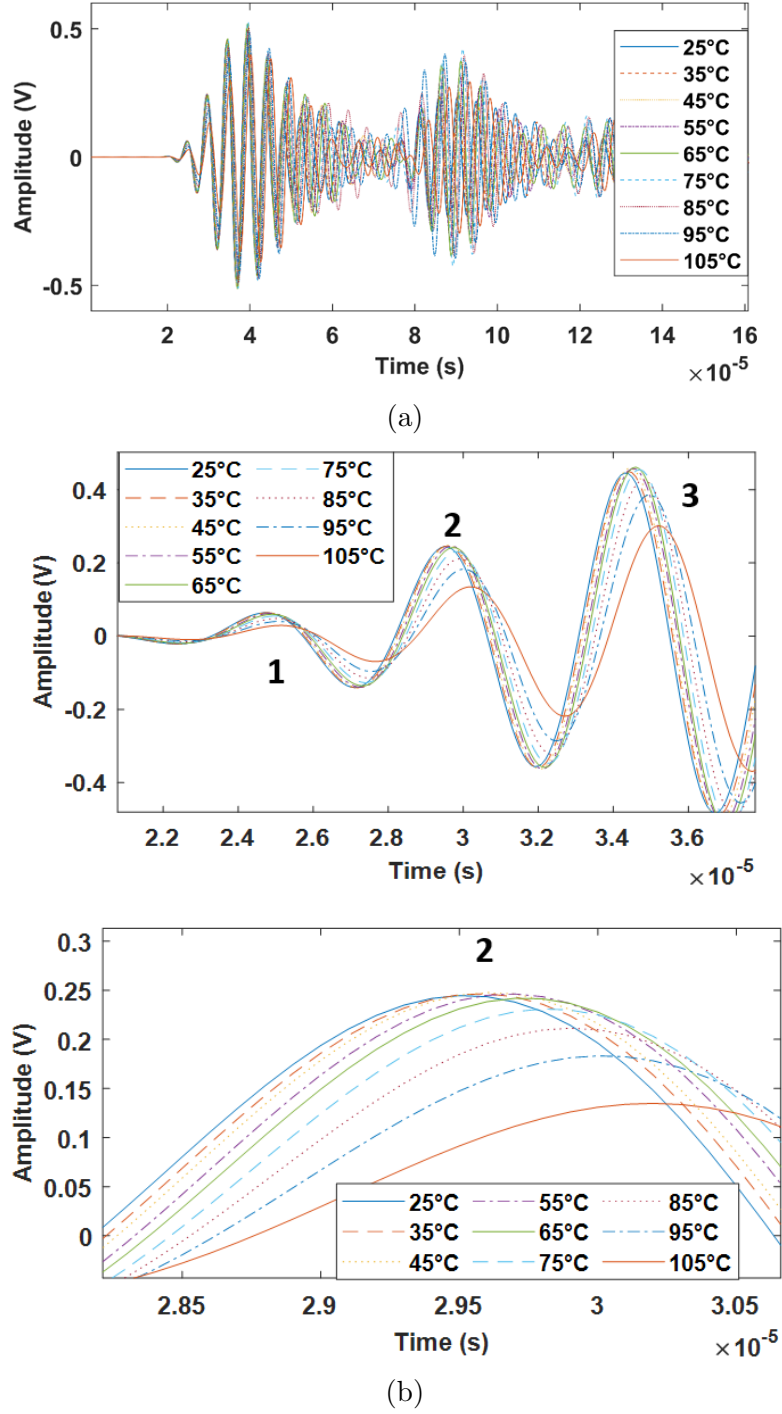


Figure 2.9: Healthy signals obtained (a) at different temperature conditions (b) zoomed in the first peak of (a) signals.

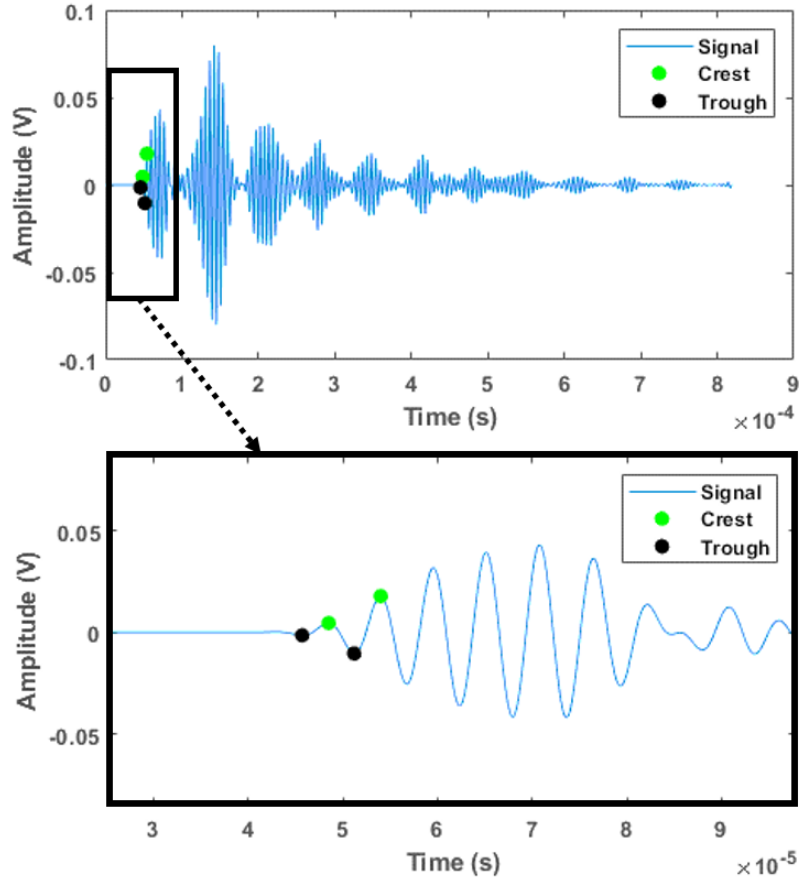


Figure 2.10: An exemplary peak picking crest and trough from GW signals at T1 25 °C .

### 2.2.6 GW studies using LDV

Analysis of structures using LDV GW techniques is gaining popularity because they help in FWF analysis which gives a 3D representation of the wave motion for the user to interpret, signal visualization from the measured scanning points (points or locations where LDV does the scan/map) and also can be used in analyzing complex structures [88]. Researchers investigated CFRP plate with stiffener attached using GW LDV methods in [89]. Maio et al. [90] used the GW LDV approach to perform damage detection analysis based on the varying velocity anisotropic nature of the specimen. Zheng et al. used GW LDV [91] technique to analyze a stiffened CFRP plate by comparing TOF of the waves obtained from various scanning points at various locations of the plate [92]. Apart from just visualizing the GW-FWF from the LDV data, the 3D data from the LDV can also be visualized as energy map/wave energy distribution [3] using root mean square (RMS) formulations as shown in Equation 2.1,

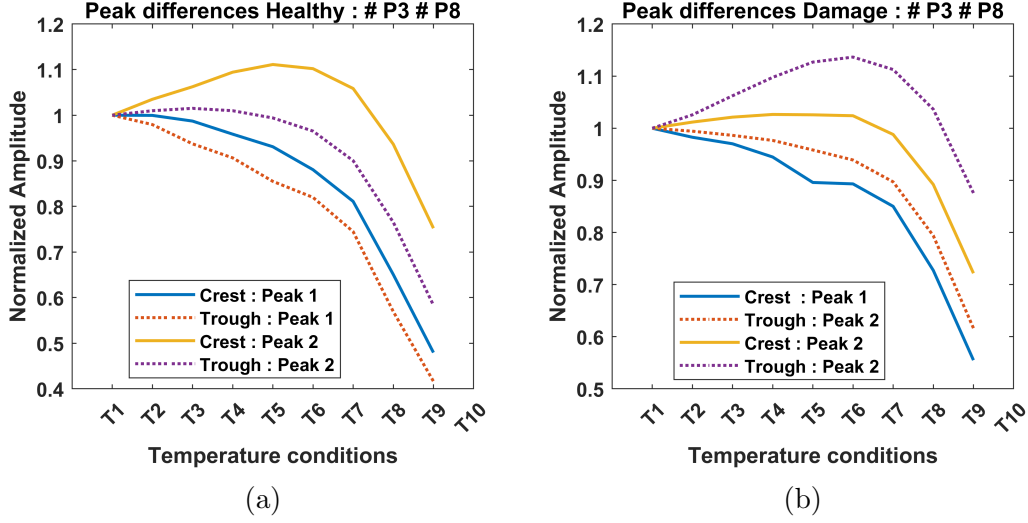


Figure 2.11: GW amplitude trend due to temperature effects excitation by P3 and sensed by P8 of sample in Figure 2.8 under (a) Healthy, (b) Damage.

weighted RMS (WRMS) as shown in Equation 2.2, radial RMS (RRMS) as in Equation 2.3 to gain more insights from the data like damage shape, size, and even quantification.

The wave energy is primarily related to the 3D signal data obtained from LDV, and RMS aids in its visualization. The RMS provides the signal energy distribution. However, if more energy accumulates in a specific region, the RMS [93] value increases. This occasionally causes the damage zone to blur. In such cases, an RRMS function is added, improving the results. The residual weight factor (RWF) is the radially weighted factored value for each scanning point, and an is the weight factor's power. The excitation points in this function are the origin point  $(x_0, y_0)$ , and the radial/Euclidean distance from it is measured for all the points  $(x_i, y_i)$ , as shown in Equation (2.4).

$$\text{RMS} = \sqrt{\frac{\sum_{i=1}^N (k_i(x, y, t))}{N}} \quad (2.1)$$

$$\text{WRMS} = \sqrt{\frac{\sum_{i=1}^N (k_i(x, y, t) \cdot i^k)}{N}} \quad (2.2)$$

$$\text{RRMS} = \sqrt{\frac{\sum_{i=1}^N (k_i(x, y, t))}{N}} \times [\text{RWF}]^k \quad (2.3)$$

$$\mathbf{RWF} = \sqrt{(x_0 - x_i)^2 + (y_0 - y_i)^2} \quad (2.4)$$

Where: ' $k_i(x, y, t)$ ' is the sample amplitude for points along with the x, y-axis and N is the number of time (t) samples, ' $k$ ' is the power of weighted factor.

Wojtczak et al. [94] investigated the use of the RMS energy of GW in damage detection. In addition to RMS energy studies, the author of [95] investigated damage detection using WRMS. RRMS formulation using LDV data was investigated by Saravanan et al. [93] to quantify the size of the damages in steel structures. To study the effectiveness of the LDV GW a small case study was conducted to locate the debond in an L-shaped stiffener (2 cm thick) attached to a GFRP plate of dimensions  $50 \times 50 \times 3 \text{ cm}^3$ . In this case, the FWF-GW results obtained from LDV are used. Two PZTs were attached to excite the GW and sensed using LDV. The GFRP specimen is shown in Figure 2.12 along with the identified debond region from PZT1 as a contour RMS plot (coloured to show the debond differentiation). More details about using LDV and RMS study can be found in subsections 2.3.1, 5.2.3, A.3.1 and also in the author's research paper [86].

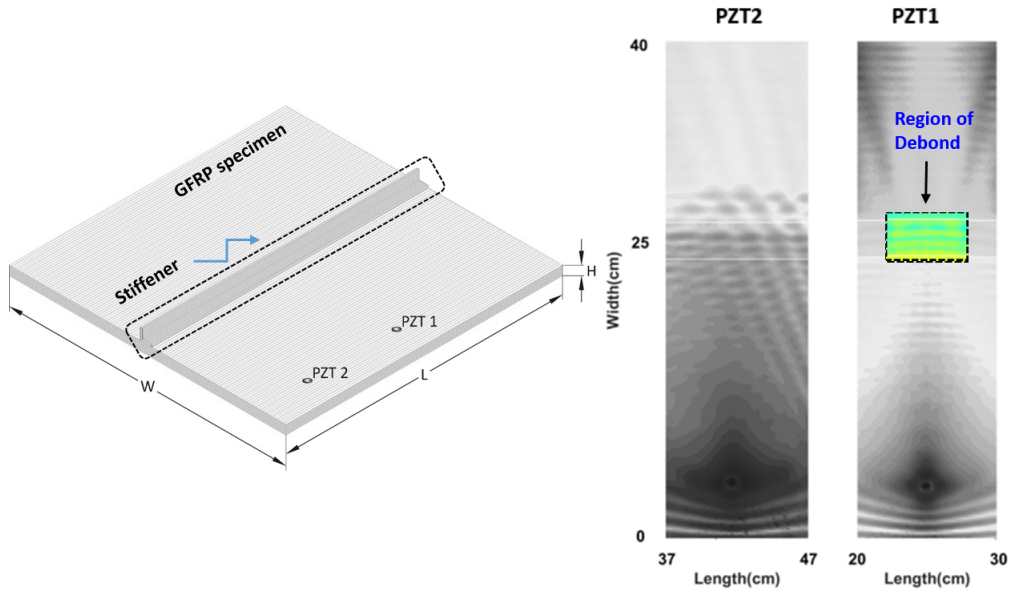


Figure 2.12: GFRPS with stiffener assembly and located debond using LDV-RMS study.

It was clear the methods are effective at obtaining localization after studying the LDV GW method with FWF techniques. However, the major disadvantage of such an approach is that they take a long time (based on the total

no. of scanning points used) and LDV-based techniques cannot be used in the continuous monitoring of the structures. The alternative to such is using sensors and placing them around the structure to monitor it continuously. Thus, the SHM with GW continuous monitoring technique involves placing the sensors, checking the signals and TOF of the waves, applying DI, localizing the damage, and quantifying the defects.

### **2.2.7 GW studies using FEM**

Researchers also used FEM simulations before conducting and after conducting experiments to check the GW propagation numerically. FEM simulations come in handy when the cost of the equipment to perform the test is huge, unfavourable circumstances to conduct the experiments, etc. Saravanan [96] developed a root-finding method based on the waveguide Padé approximation technique for predicting dispersion curves of fundamental modes [97]. Researchers also used stiffened composite models based on FEM to examine the GW's dispersion behaviour [98]. The varying dispersion values between the debond region and the perfectly bonded region were demonstrated using predicted and modelled dispersion curves in these studies. This information may not always be available, reducing the effectiveness of the proposed methods. Numerical-based spectral elemental (SEM) codes were also used in studying impact damage [99]. A combination of experimental and numerical SEM methods was used in detecting the impacts in composite structures [25].

### **2.2.8 Summary**

Based on the research conducted, the study draws a conclusion that certain SHM methods require both healthy and damaged samples to compare damage indices, and as such, cannot be regarded as reference-free techniques. Additionally, there are few studies available that have employed a common SHM methodology to analyze various damage types, utilizing different sensor types. Addressing the limitations identified in the study, chapter 3.1 outlines the SHM-GW multistep method, a comprehensive common approach that integrates multiple sensor types and analysis techniques to facilitate the detection and monitoring of diverse types of structural damage.

## **2.3 GW sensing instruments used in the study**

Before starting to discuss the proposed techniques to counteract the drawbacks, the equipment used in the research thesis should be discussed. This



section discusses the working principle of the instruments used in the research thesis work. The research study is primarily focused on analyzing the GW and its propagation, interaction, and significance of it in visualizing different damages. The following are the instruments used in the entire SHM GW study for assessing various structures.

### 2.3.1 GW analysis using LDV

The Polytec PSV400 LDV type is used to sense the GW in the experiment, as depicted in Figure 2.13. It uses a single laser head to register signals and detect the out-of-plane velocity component based on the Doppler Effect. The LDV provides real-time temporal signatures of surface velocity by analyzing the frequency shift between the incident and reference beams, which is recorded by the interferometer via a photodetector in the LDV head. As the laser head was kept at a distance from the object being measured, the measured response primarily represents the out-of-plane velocity component.

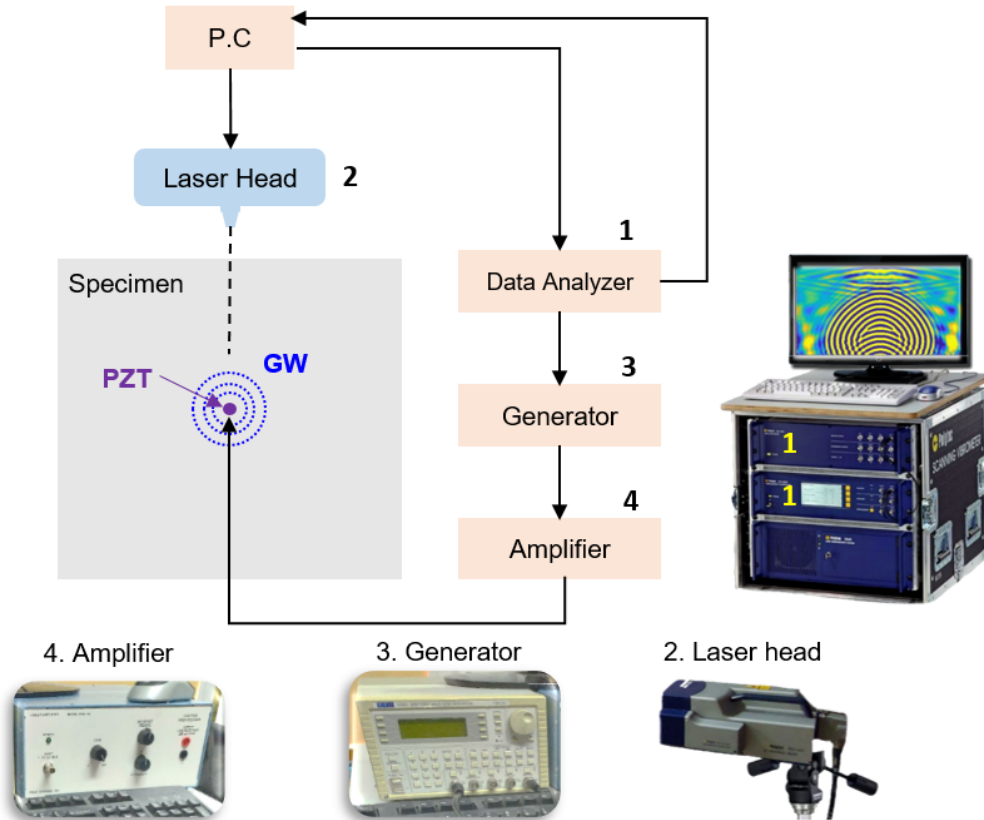


Figure 2.13: Schematic LDV setup for GW acquisition.

Figure 2.13 shows that the PZT attached to the structure's surface produces excitation. To decrease the signal-to-noise ratio, the structure being tested is



covered with a retroreflective film. The laser beam is focused on the specimen panel, and the structures are typically attached to a stand with nylon strings or placed on soft foams or specialized pads to minimize noise and vibrations [25]. The LDV instrument is set to a proper filter cutoff frequency to eliminate unwanted frequencies or those outside the excitation range. The PZTs are excited using an N (mostly 5 or 10) cycle Hanning window sine modulated pulse, and each signal is averaged multiple times (roughly 10 or 20 times). Measurements were taken for a set of evenly distributed scanning points across the panel surface

An arbitrary waveform generator TTI TG was used in exciting the GW signals by sending a continuous voltage of 16 V<sub>pp</sub> (peak to peak voltage) with a gain amplification (amplifier EP-104 from *Piezo Systems*) of 20 times ( $16 \times 20 = 320$  V) is applied to PZT. To capture the shortest of the wave, a dense mesh of grid points was created, adhering to the Nyquist-Shannon (N-S) sampling theorem. The sampling frequency was chosen to be ten times greater than the carrier frequency (excitation frequency) in most of the cases [88]. Throughout the process, a constant room temperature is maintained. The experiments were carried out at various frequencies.

### 2.3.2 Data acquisition using DAQR

A USB cable connects the 13-channel DAQR setup [100] to a Matlab-controlled computer. It has 13 connections and can connect up to 12 PZTs for actuation and sensing. Figure 2.14 shows a schematic setup of DAQR and its connecting configuration with PC and specimen. The Matlab code appears as a toolbox, allowing users to enter the following information;

1. Frequency: Input the frequency in kHz.
2. Number of cycles: Input the required sine cycles.
3. Number of channels: Input the number of PZTs connected.
4. Window: Select the window type (Hann/rectangle/square) used for the modulation.

### 2.3.3 GW analysis using PZT and FBG hybrid method

A tunable laser (*Apex AP1000*) coupled with FBG (*Femto Fibertech*) is used in this experimental research study [101]. Figure 2.15 shows the FBG experimental schematic setup. The sensitivity/ increased magnitude of the signals

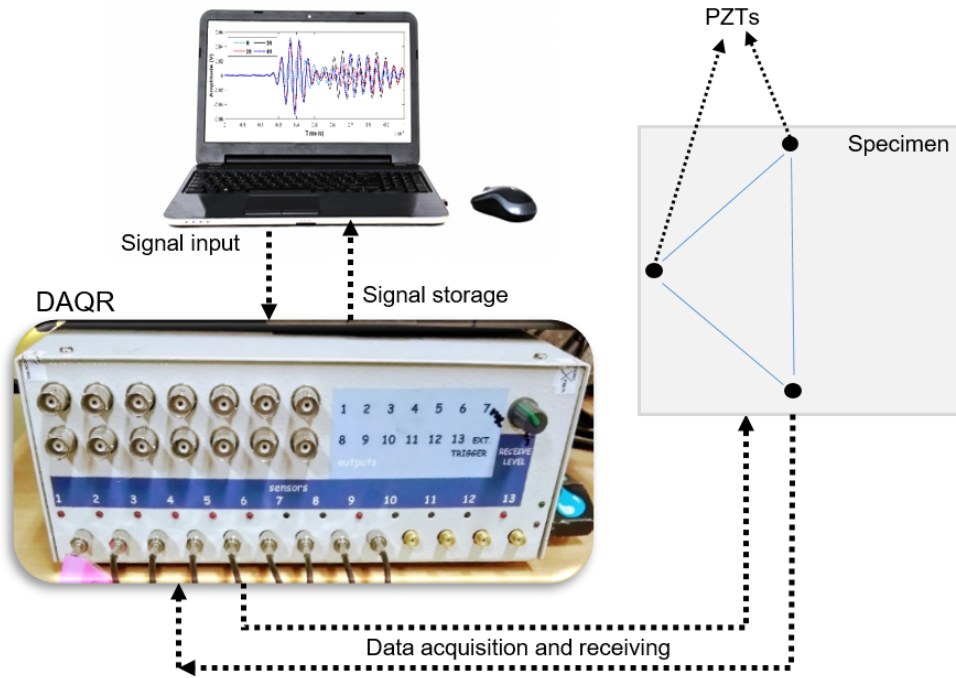


Figure 2.14: DAQR Schematic setup.

can be obtained using the edge filtering technique (Figure 2.16 region of study) when using FBG sensors. In this setup, the laser is tuned on the linear section of the FBG reflectivity spectrum [102].

Due to the steep slope of the spectrum, even a small shift in the reflectivity spectrum leads to a large change in the reflected optical power. FBG measures changes in wavelength ( $\lambda_B$ ) caused by axial strain caused by excited waves. To sense the GW signals via optical coupling and at a higher sampling frequency, a pre-amplified photodetector is used in conjunction with an oscilloscope (*National Instruments, PXI 5105*). A waveform signal generator is used to generate an N sine cycle Hann window signal. The signals are amplified by an amplifier (*Krohn Hite 7500*) before being fed into PZTs. The edge reflection configuration demonstrates increased/ improved sensitivity [13].

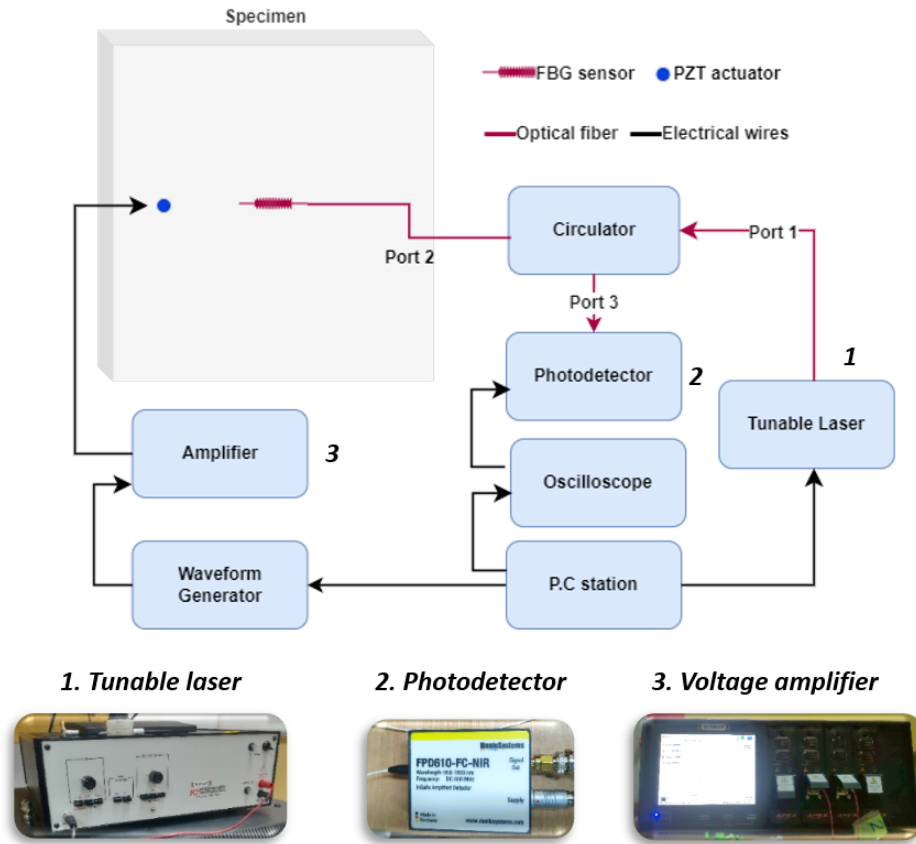


Figure 2.15: Fiber optics GW experiment schematic setup.

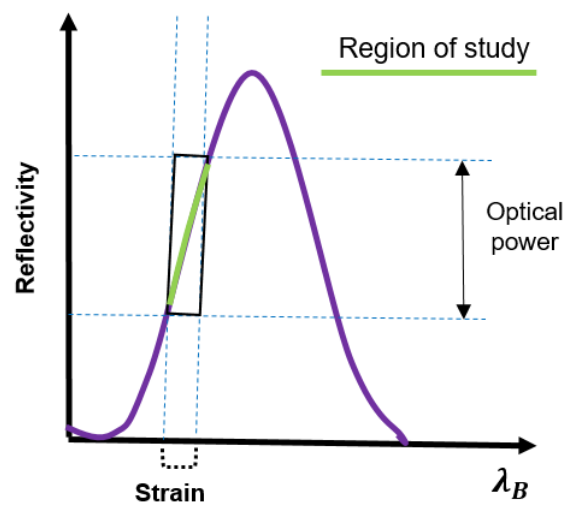


Figure 2.16: Reflectivity spectrum slope.

## Chapter 3

### Motivation/objectives of the research

#### 3.1 Research gaps and objective

Most methods for detecting and localizing damage in structures involve analyzing GW signal patterns in the sensor-actuator paths or within the sensor network. In such cases, SHM-GW analysis can provide a damage contour plot of the entire structure, which involves assessing the entire surface of the structure to map and visualize the distribution of damage. This increases the calculation time, so a method needs to be formulated to remove other regions (so that to carry out the simulation restricted to some regions) not involved in damage (healthy region) and use only identified regions for damage mapping. Researchers are constantly developing new techniques to improve the accuracy and efficiency of these methods. Furthermore, in most studies from the literature survey, the damage was either located far from the actuator or sensor (so that its reflections could be picked up) or was in the middle of the structure, within the sensor's field of vision.

There has not been a thorough investigation of scenarios in which the damage is very close to the PZT sensor. The reason being the higher energy produced by the PZT masks the damage. Also, there are cases in the SCS involving multiple damages (e.g., debonding and impact combined) that were not localized. Larger system-level structures require a quick damage detection DI to zero in on the damaged region in order to carry out local area-based NDT applications such as IRT, terahertz (THz) spectroscopy, and so on. Higher sensitivity, ease of installation, immunity to electromagnetic interference, quick reaction time, multiplexing stability, and long-term stability are reasons to think about using FBG as a sensor against PZT in recent years. Thus a PZT-FBG hybrid combination (summing the pros of both the PZT and FBG) was tested in the later stages of the research project to check its sensitivity to damage. Differ-

ent adhesive bond lengths also were not investigated in much detail using FBG bonding types, which was identified as a research gap to study further.

The purpose of this research thesis is to investigate and solve the aforementioned difficult scenarios using a common multi-step method that is applicable to different sensor types, different materials and damage types. Rytter [103] proposed a four-step approach (Table 3.1) to classify the damages and a similar but improved methodology is developed as a common multi-step methodology in this research thesis. The thesis proposes an improved SHM common methodology in damage identification (detection, localization and quantification) analysis that is applied to any material type (aluminium, CFRPS, GFRPS, SCS), sensor type (PZT, LDV, FBG) and damage type (crack, debond, impact, stiffness change).

S.No	SHM levels	Steps and specifications
1	SHM Level 1	Damage detection
2	SHM Level 2	Damage localization
3	SHM Level 3	Damage quantification
4	SHM Level 4	Prognosis (structure's remaining life cycle)

Table 3.1: SHM levels for damage study.

### 3.1.1 SHM-GW common multi-step method

The common multi-step approach is elaborated as follows; the damage detection (step 1) and localization (step 2) followed by quantification (step 3) based studies. The damage detection step involves identifying the damage sensor paths when assessing the GW signals. A DI using root mean square deviation (RMSD) [5] is performed when PZT sensors are used to identify damage. It is challenging to use the RMSD technique because of the directional sensitivity [102] of the FBG sensor.

The FBG sensors show directional sensitivity, and the sensitivity follows a cosine-squared relation, so in the directions perpendicular to the sensor, the sensitivity is very low [4] as shown in Figure A.14. So any amplitude-based metric [13] such as RMSD or other signal difference techniques for quantifying the change in the healthy and damaged signal will be affected by the different angles of the incident wave (increased contribution of noise to the metric) as shown in Figure 3.1b. A damage metric which takes into consideration the

similarity of the signals (not the amplitudes) will allow us to overcome this issue.

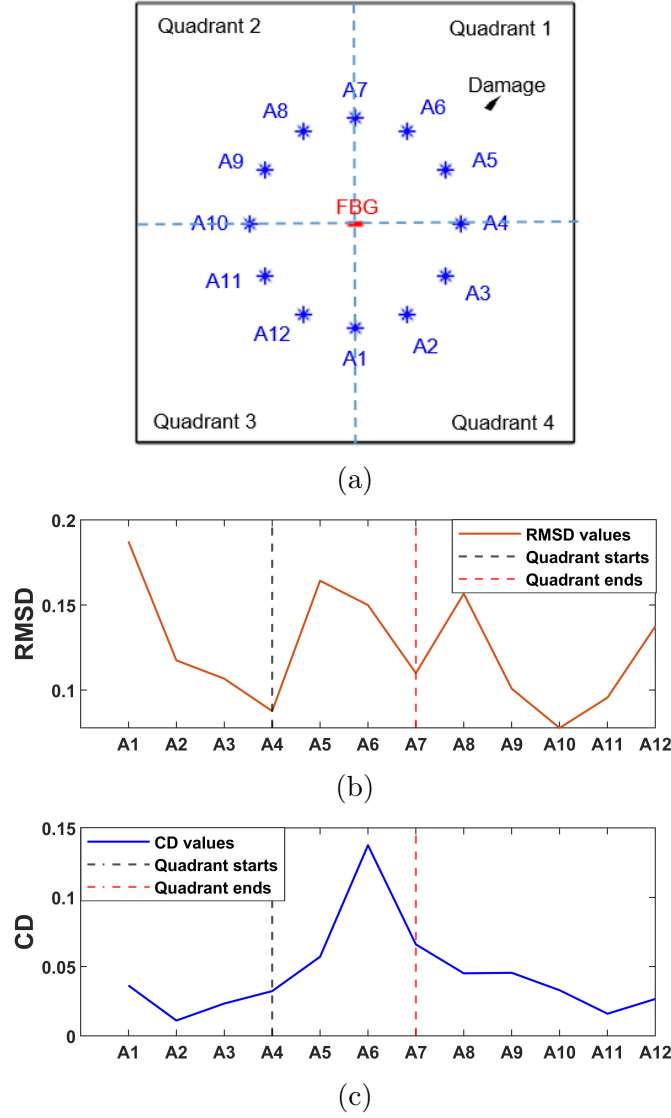


Figure 3.1: DI study : (a) Schematic plate, (b) RMSD, (b) CD.

The cosine distance (CD) similarity-based method [104] is used (as shown in Equation 3.1) in such cases to detect damages in the signals obtained from the FBG sensor because it is independent of amplitude or scaling. An exemplary Figure 3.1 shows an ALS plate with a single FBG sensor, 12 PZTs (actuators), and damage was positioned between A4 and A7 (referred to as Quadrant 1) to evaluate GW effects. The values of the RMSD showed no differences (Figure 3.1b), however, the values of the CD with cosine squared relation picked up the likely damage region well by exhibiting increasing values at the Quadrant 1 region (Figure 3.1c).

The CD calculations are used to compare the healthy (H) and damaged (D) path time signals treated as vectors and ascertain the difference in the signal paths. To identify the damaged regions, all potential actuator-sensor pairs are investigated using the improved CD formulation with a range of  $0 \leq CD \leq 1$  (where 0 signifies identical signals and moving towards 1 shows larger varying signals). The damage detection step 1 (Figure 3.2) aids in determining which regions are vulnerable to damage. In this way, the other regions are isolated, and possible damage zones are grouped together as sectors.

$$CD(H, D) = 1 - \left| \frac{HD'}{\sqrt{(HH')(DD')}} \right| \quad (3.1)$$

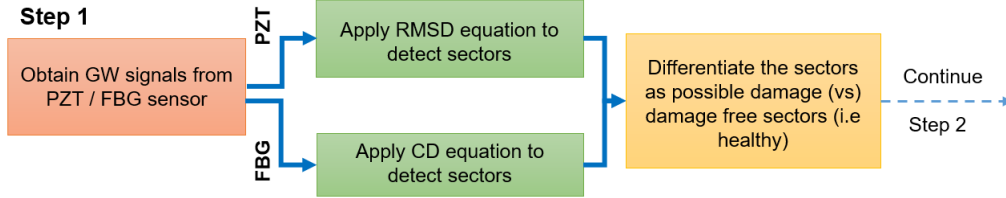


Figure 3.2: Damage detection: Step 1.

The damage localization step 2 (Figure 3.3) is accomplished by employing a quick DI-based formulation with ellipses termed as sector elliptical (SEC) method (elaborated in subsections 4.1 and 4.2) to locate sectors. The sector calculation aims to reduce calculation time by introducing angular and circular sector-based damage indices calculations. The calculation time is reduced because the localization step is applied only to the identified sectors and not to the entire model. The SEC with effective path coverage is applied to sectors identified in the damage detection step to pinpoint the location of the damage in the damage localization step. The method works by utilizing the symmetry of the proposed circular network of PZT actuator-sensor or PZT actuator and FBG sensor arrangements or PZT-LDV sensing units to identify the damage locations. The sector calculation aims to reduce calculation time by introducing angular and circular sector-based damage indices calculations. The calculation time is reduced because the localization step is applied only to the identified sectors and not to the entire sensor-actuator paths. Thus, the shortcoming mentioned earlier were solved using the SEC step. SEC helped to localize the damages near the actuator, far from the actuator, and multiple damages in bonded specimens rapidly.

In this SEC study, a circular sensor network is used to examine various struc-

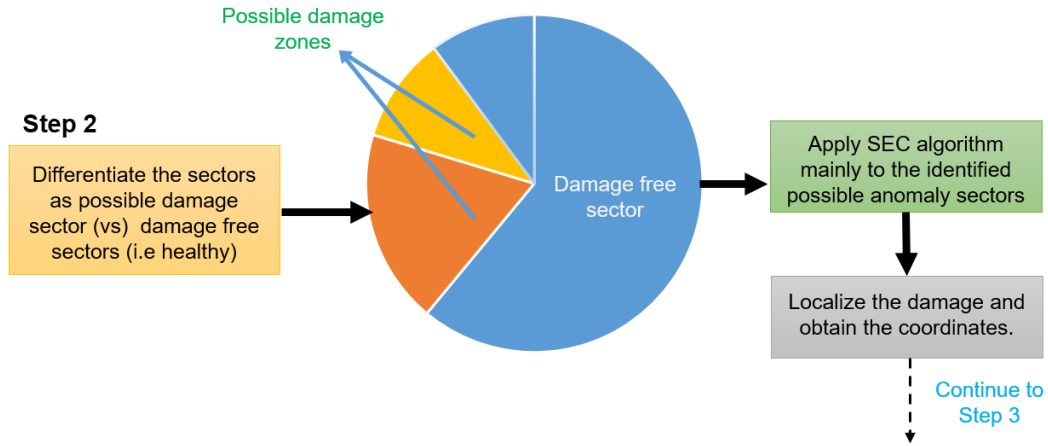


Figure 3.3: Damage localization: Step 2.

tures with different damage scenarios. Based on the analysis to identify the damages present both inside and outside the network (an elaborated diagram of the procedure is shown in Figure 6.1), such a network was selected. For detecting the damage inside the sensor network RMSD (in the case of PZT as a sensor), CD (in the case of FBG as a sensor) is applied to signals up to the first wave peak (first wave arrival) and for detecting the damage outside the sensor network full wave signals are used in step 1 to detect the sectors. This type of network is preferred for most cases in the thesis, as it was required to locate damages at multiple locations, near the actuator, and near the boundaries. Such a kind of network was previously used by many researchers [79], [87], [50] to localize damage within the sensor network. In this research work, a single PZT sensor is used (mostly at the centre of the structure) as shown in Figure 3.4a surrounded by circular PZT actuators. A similar circular network is used with FBG (Figure 3.4b) at the centre for sensing and PZTs acting as actuators.

It was discovered that the majority of GW-based research works focus primarily on damage detection or localization, with only a few works dealing with damage dimension estimation/quantification. Damage size measurements are critical in industrial engineering. A clear understanding of the extent of the damage is required before deciding whether to continue using the structure or repair it. The quantification of impact damages and cracks is critical in estimating the remaining life of the structure [105]. To check the damage quantification confusion matrix (CM) based studies were applied to the SEC results to approximate the size of various kinds of damage (step 3 - Figure 3.5).



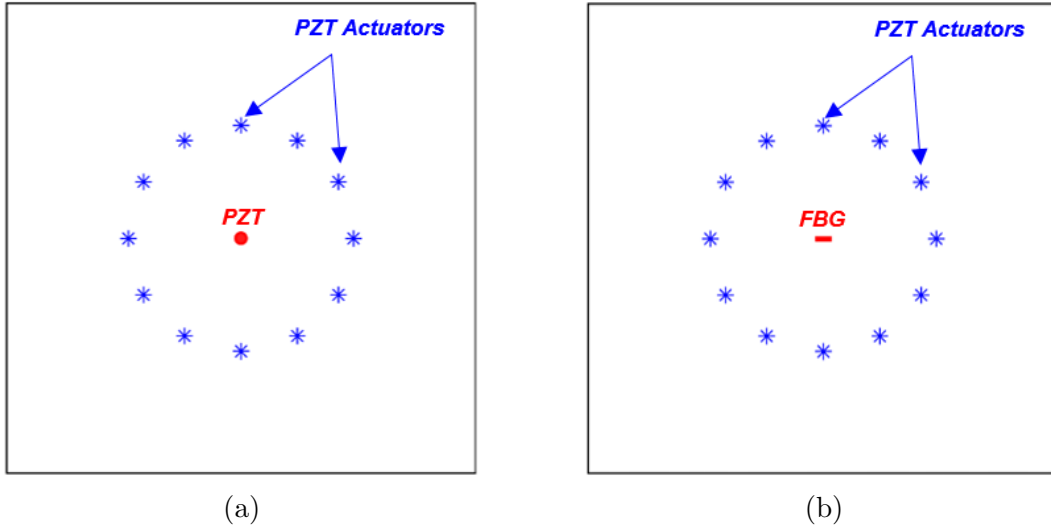


Figure 3.4: Sensor network: (a) PZT-PZT, (b) PZT-FBG.

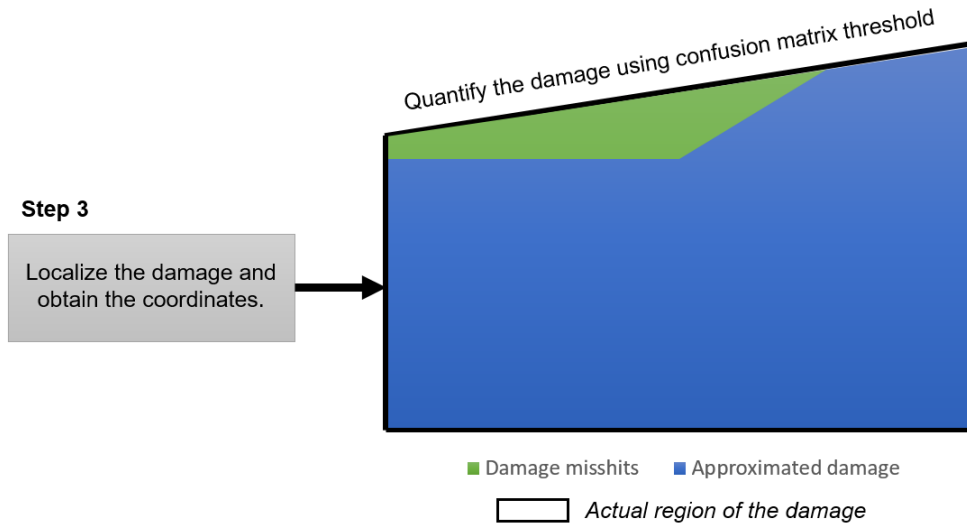


Figure 3.5: Damage quantification: Step 3.

### 3.1.2 SHM-GW analysis using FBG remote bonding

Another important contribution to the FBG sensing GW is the changing adhesive bond lengths in a remote bonding FBG configuration study as shown in Figure 3.6. The research also compares bonding configurations with different PZT connections that were performed on an ALS. The findings are elaborated in chapter 6.3.

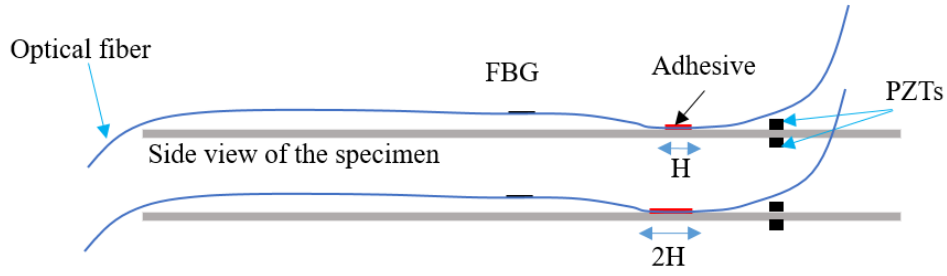


Figure 3.6: Changing FBG bond length with remote bonding configuration.

### 3.2 Research objectives achieved

The research studies various GW modes and their usefulness in analyzing different materials. The ultimate aim of the research work lies in developing time-effective damage identification techniques (common multi-step method) in analyzing various isotropic and anisotropic structures with different kinds of damage sensed with different sensing units. The developed SEC method helps to locate the different types of multiple damages present both inside and outside the structures. The research motivation also aims to check the method in the developed FBG-PZT hybrid models and to effectively locate the damages by embedding FBG into the structures. The summary of the objectives is as follows;

#### 1. Analysis of GW signals and classification of GW modes.

- Studying the GW multi modes in assessing different composite types and aluminium structures as shown in Table 3.2.
- Visualization of FWF results which includes GW modes, and GW interactions with the damages.
- Comparing the theoretical dispersion values against the experimental results obtained.
- Develop and test signal processing methods in studying GW signals and their interactions with the structures.
- Implementing rapid DI in damage detection studies that use PZTs, LDV and FBGs.
- Implementing unidirectional GW-sensitive damage detection methods when using FBG sensors.

2. Improved elliptical damage localization using SEC.

- Implement the elliptical approach in damage localization of structures.
- Addition of amplification factor to the elliptical method (more details in section 4.1) in damage localization.
- Studying the TOF of fundamental modes and in addition, reflection peaks to improve the damage localization algorithm.
- Testing/evaluating the developed SEC method in numerous composite and aluminium samples with different kinds of damage.
- Evaluating the developed SEC method with coupled FBG-PZT sensor networks.
- Testing the efficiency of the developed method in terms of computational time and storage space.

3. Adhesive bond length studies using FBG sensing measurements.

- Studying bond lengths and bond types using GW-assisted FBG sensing.
- Checking analytical equations to study FBG strains.
- Graphical user interface (GUI) tool development for checking the FBG strains effectively (shown in Appendix A.6.1).
- Study of different PZT configurations (shown in Figure 7.1) to study the effective GW FBG sensing phenomena.
- Comparison of studies of bond length and bond types to check the relative magnitude of GW.
- Implement the developed bond length studies in studying FBG embedded structures.

4. Comparison of numerical FEM simulations with experimental studies.

- Develop a 2D, 3D FBG PZT hybrid numerical model (FEM) of the structure to compare against the experimental results.
- Apply directional sensitivity [3]-based DI schemes (CD) to locate the damaged regions when using FBG sensors.
- Implement the developed SEC method to FBG-PZT hybrid FEM models with multiple damage scenarios.

- Develop FEM model for FBG embedding studies and compare the theory of in-plane wave interaction through structures [1].

### 3.3 List of material specimens investigated

A variety of material/structural samples from the subsystem and system levels were chosen to perform the multi-step SHM methodology. The specimens used, damage types and measurements performed are shown in Table 3.2 and are also thoroughly explained in this section.

S.No	Material /structure	Damage specification	Studied with	Shown in chapter
1	GFRP	Debond	LDV	2
2	GFRP	Impact damage	LDV	5
3	CFRP	Impact damage	LDV	6
4	CFRP	Impact at different temperature conditions	DAQR	2
5	ACS	Impact damage, mm holes	LDV	5
6	SCS	Debond	LDV, DAQR	6
7	ALS	Multiple mass placements	FBG	6
8	ALS	Bond length	FBG	7
9	ALS	Stiffness change	FEM	6
S.No	Material /structure	Checked	Studied with	Shown in chapter
10	ALS	Through thickness GW mode profile	FEM	7
11	ALS	GUI and directional sensitivity	FEM	A

Table 3.2: Selected materials/structures for the SHM-GW analysis.

1. The adhesive failure (debond) of the GFRPS with stiffener assembly was tested. LDV was effectively used to detect the presence of the debond region. Results obtained are shown in subsection 2.2.6 and in Figure 2.12.
2. The GFRPS was subjected to low energy impact defects and the LDV-based GW method was used in examining the specimen. The presence

- of damage was visualized using the RMS and RRMS energy maps. An SHM study was started to determine the coordinates of the damage using only a few sensing points. The results obtained are shown in section 5.2.
3. A CFRPS was subjected to impact cracks and the crack was assessed using LDV-based SHM studies. The results obtained are shown in section 6.2.
  4. DAQR was used to test impact-damaged CFRP material at various temperatures. This experiment also investigates the temperature effect on GW with and without impact damage. Results obtained are shown in subsection 2.2 and Figures 2.7-2.11.
  5. ACS with impact damages and mm size holes were successfully analyzed using LDV and the location of the damages was also successfully verified using SHM studies. The results obtained are shown in section 5.1.
  6. SCS with multiple debond failures were successfully studied using DAQR-based SHM studies and the failure was also quantified. The results obtained are shown in section 6.1.
  7. FBG SHM experimental GW study was implemented in this case to study the effects of multiple mass placements causing changes to material properties in an ALS. The location of multiple damages was predicted using the SHM studies. Results obtained are shown in subsection 6.3.3.
  8. The varying adhesive bond length and its effect on guided waves were experimentally studied using FBG. Results obtained are shown in subsection 7.1.
  9. Change in stiffness matrix-based damages on the modelled aluminium structure was checked using SHM damage identification and localization schemes. The results obtained are shown in chapter 6.3.
  10. GW and its effect through the thickness of the ALS structure were checked using FEM studies. Results obtained are shown in subsection 7.2 and in Figures 7.8-7.11.
  11. GUI toolbox was developed for sensing different strains obtained from numerical studies quickly. GW directional sensitivity of the FBG sensor [3] study was performed using GW FEM studies on the modelled 1D structure. The results obtained are shown in subsection A.6.

### 3.4 Thesis outline

The thesis outline consists of in total eight chapters (including the introduction, literature review and motivation/objective of the research) dealing with damage detection, localization, and quantification schemes as follows;

- Chapter 4: The proposed SEC method is explained in detail in this chapter.
- Chapter 5: The effectiveness of the ellipse-based damage localization algorithm is discussed in this chapter. ACS and GFRPS structures were used to demonstrate the algorithm's effectiveness with regard to increased amplification factor and threshold limits.
- Chapter 6: This chapter details the multistep methodology and its effectiveness in identifying various types of damage in various structures. It covers the methodology's adaptability in locating multiple damages both inside and outside the sensor zones using circular sensor networks. The chapter also shows the CM-assisted quantification approach used. Additionally, the chapter includes the investigation of FEM models with multiple damages and the development of an Abaqus-Matlab link code to automate the GW-SHM process (shown in Appendix A.5).
- Chapter 7: The chapter focuses on the direct FBG and remote FBG bond type configurations and sensing of GW using different PZT configurations and with increasing bond length types. FEM embedded model was also done to check the direct bonding effect of GW studies.
- Chapter 8: The chapter summarizes the overall results and outcomes of the research thesis.
- Appendix A: The appendix chapter showcases the NDT methods used to verify the analyzed SHM damage scenarios. This appendix also demonstrates GUI development to identify the reflectivity spectrum from the strain inputs of the FEM results (shown in Appendix A.6.1), which is then used to extract the GW signals and further signal processing.

### 3.5 Thesis to be proven

"It is possible to develop a common multi-step SHM methodology for reliable and accurate damage identification for piezoelectric-based, fiber optic-based and vibrometer-based sensing."

The aim of the thesis is to develop and evaluate the effectiveness of a common multi-step hybrid PZT-FBG method for damage identification in structures. This method involves the use of LDV, PZT and FBG sensors to monitor structural health and detect potential damage. Utilizing a common multi-step method aims to improve the accuracy and reliability of damage identification (till SHM level 3) compared to traditional single-step methods. The ultimate goal of this thesis is to provide a more efficient and effective method for detecting and diagnosing structural damage, which can improve safety and reduce maintenance costs.

## Chapter 4

### GW-based damage localization in structures

Damage localization is an important part/level of the SHM studies (SHM level 2). The location or the coordinates of the damage is important to proceed further with quantification (SHM level 3), repair and prognosis studies (SHM level 4). In the research study, an improved version of the elliptical function known as the SEC method is used for damage localization purposes.

#### 4.1 Elliptical method in damage localization

The SEC damage localization algorithm uses an elliptical convergence scheme to identify damaged regions in a structure. The method employs a TOF-based elliptical algorithm, which is based on the elliptical intersection and convergence method to highlight wave reflections corresponding to damaged regions. Figure 4.1 shows exemplary GW signal paths (path 1: P7-P4 and path 2: P1-P4 from Figure 2.8) with the incident (initial propagation (or) first wave arrival) and reflections.

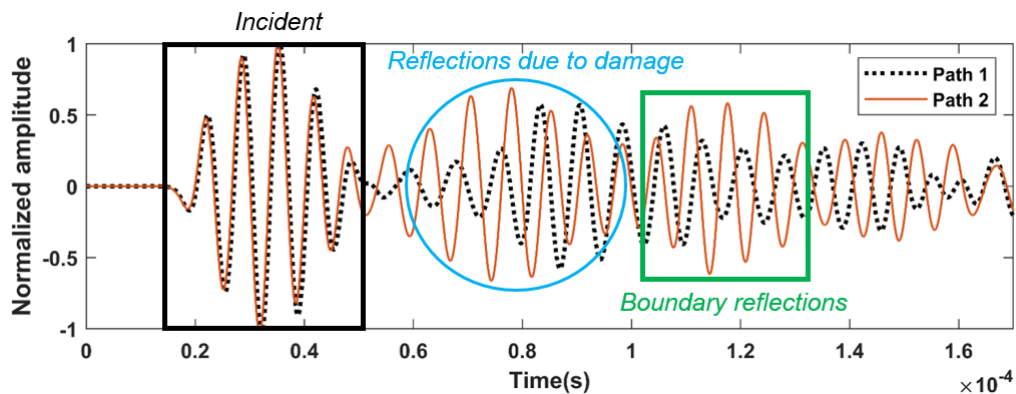


Figure 4.1: Signal paths showing incident and reflections in healthy and damaged structure.



The elliptical convergence concept is explicitly described in [72],[106] and is further improved in the thesis with a sector-specific localization strategy. The resulting output is assigned to grid points during this process. The number of grid points affects the smoothness of the visualization as well as the computational time. Fine horizontal and vertical mesh grid steps are used in this investigation to visualize the results. Following this method, the theoretical TOF denoted as  $TOF^{ref}$ , is calculated for the waves to travel from the actuator to an arbitrary grid point and then to the sensor, as shown in Figure 4.2 and Equation (4.1).

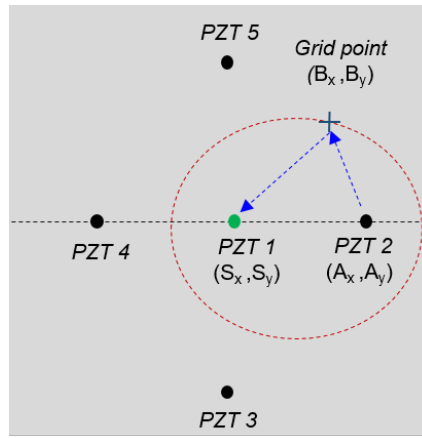
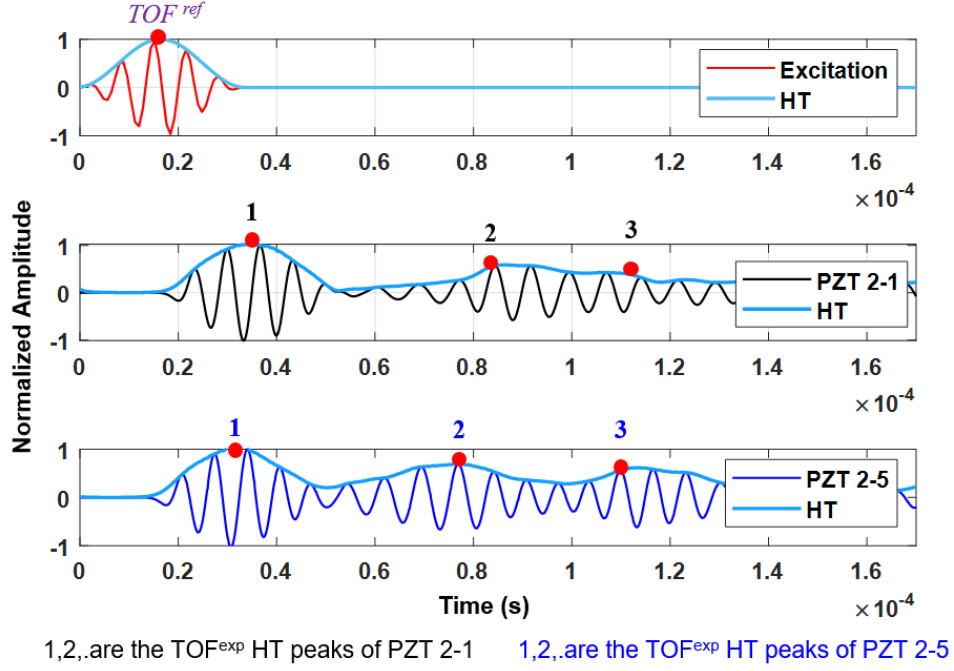


Figure 4.2:  $TOF^{ref}$  distance approximation using elliptical method.

$$TOF^{ref} = \sqrt{\frac{(B_x - A_x)^2 + (B_y - A_y)^2}{V_A}} + \sqrt{\frac{(B_x - S_x)^2 + (B_y - S_y)^2}{V_S}} \quad (4.1)$$

Where:  $B_x, B_y$  are the grid point coordinates,  $A_x, A_y$  are the actuator coordinates,  $S_x, S_y$  are the sensor coordinates,  $V_A$  and  $V_S$  is the wave group velocities from the actuator and sensor to the grid point coordinates, respectively. The group velocities are computed by knowing the distance between the actuator and sensor in the numerator, and the TOF of the wave from the actuator to the sensor in the denominator part. The group velocity is mostly the same for isotropic structures (i.e. steel, aluminium) and varies for anisotropic structures as it is angle-dependent (velocity varies w.r.t ply orientation of the composite fibers).

The Hilbert transformation (HT) envelope [3] is applied to the measured (obtained) GW signals, yielding various amplitude peaks. The peaks are then


 Figure 4.3:  $TOF^{ref}$  and  $TOF^{exp}$  peak picking calculation.

arranged in ascending magnitude order (1, 2, ...) as shown in Figure 4.3. This constitutes the  $TOF^{exp}$  which is the TOF obtained from peak values of the experimental GW signals. The actuator-pixel-sensor path's overall distance and the wave's group velocity are used to calculate the  $TOF^{ref}$  Equation 4.2.

$$L(x, y) = \sum_{n=1}^{AS} Exp \left[ -\frac{TOF^{ref} - TOF^{exp}}{\tau} \right] \quad (4.2)$$

Where:  $L(x, y)$  is the localization index,  $AS$  is the total number of actuator sensor paths used. According to the literature [72], the decay factor  $\tau$  with a value of  $5 \mu s$  is used for both anisotropic and orthotropic material types.

The  $TOF^{exp}$  is then correlated with the obtained peak  $TOF^{ref}$  values. When the  $TOF^{ref}$  agrees with the peak location ( $TOF^{exp}$ ) identifying the damage region, a higher value in the grid location is identified. Figure 4.3 shows an example of  $TOF^{ref}$  and  $TOF^{exp}$  correlation between the excitation signal, path (PZT 2-1), and path (PZT 2-5) signals. The elliptical distribution area (decay factor) of each sensing path is scaled by a quantity denoted by  $\tau$ . If  $\tau$  is set too low or too high, the resolution will be lost. Exemplary Figure 4.4 is shown to explain the resolution loss for  $\tau$  value of  $3 \mu s$  and a similar loss was also noticed

at  $\tau = 4 \mu s$ . This poor resolution in turn reduces the artefacts which makes it difficult to process the results. A better resolution image was obtained for  $5 \mu s$  of  $\tau$  and higher values. The value of  $5 \mu s$  is thus taken as a trade-off value. Figure 4.5 shows a simplified flowchart of the elliptical algorithm.

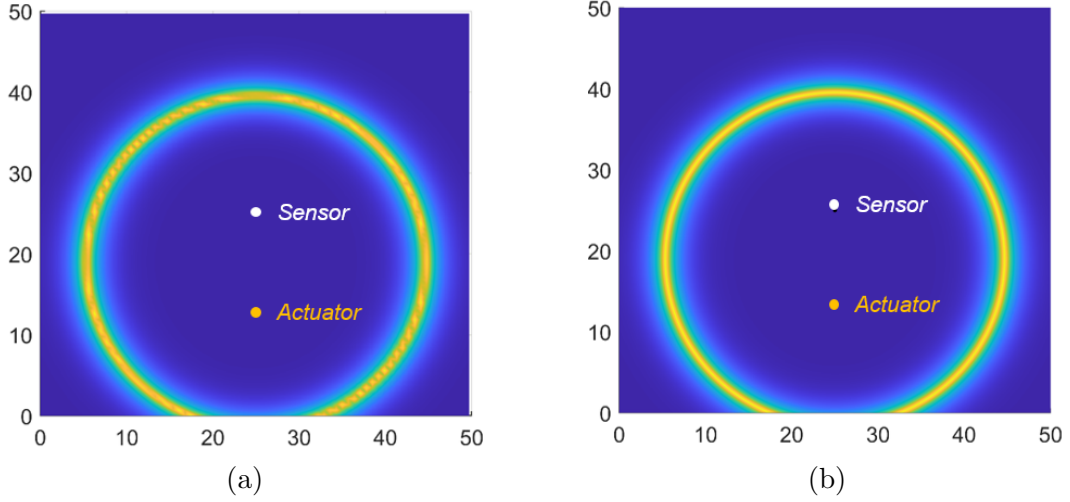


Figure 4.4: Ellipse resolution for  $\tau$  at: (a)  $3 \mu s$ , (b)  $5 \mu s$ .

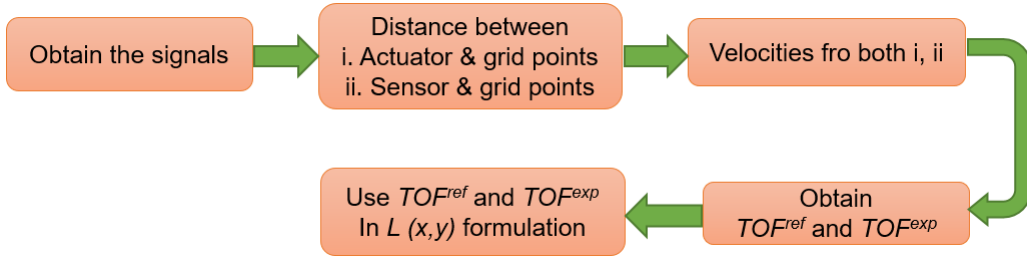


Figure 4.5: Flowchart of the elliptical algorithm.

## 4.2 Sectorial Elliptical (SEC) method in damage localization

The following are the important modifications done to Equation 4.2 for improving the damage visualization with amplification factor (Equation 4.3), the addition of a threshold factor for quantification analysis (Equation 4.4) and improving the calculation time (Equation 4.6) by segmenting the regions with healthy and damaged sectors.

- Introducing the amplification factor to the Equation 4.2

$$L_A(x, y) = \sum_{n=1}^{AS} (AF) \exp \left[ -\frac{TOF^{ref} - TOF^{exp}}{\tau} \right] \quad (4.3)$$

Where:  $AF$  is the amplification factor, which is the maximum peak amplitude picked up after every iteration run. The amplification factor multiplication helps to improve the resolution of the ellipses for damage imaging purposes.

- Introducing the  $AF$  with a threshold limit (Equation 4.2).

$$L_N(x, y) = \sum_{n=1}^{AS} (AF) \text{Exp} \left[ -\frac{TOF^{ref} - TOF^{exp}}{\tau} \right] \quad (4.4)$$

Apply a threshold limit based on the CM factors (for example, true positive, false negative, precision, error rate, specificity, etc [107]).

$$L_N(x, y) \geq N$$

Where:  $N$  is the predicted threshold value to plot the contours of the damage index.

- Applying the elliptical algorithm (exemplary case Figure 4.6 shown with steps 1 and 2) to DI results (e.g RMSD Equation 4.5) obtained from the detection step.

$$RMSD = \left( \sqrt{\frac{\sum_{i=1}^N (H - D)^2}{\sum_{i=1}^N (H)^2}} \right)_{WAS} \quad (4.5)$$

$$L_{SA}(x, y) = \sum_{n=1}^{AS} A^T \text{Exp} \left[ -\frac{TOF^{ref} - TOF^{exp}}{\tau} \right]_{SA} \quad (4.6)$$

Where:  $H$  and  $D$  are healthy and damage signals,  $WAS$  in Equation 4.5 denotes the entire area of the sensor network analyzed and  $SA$  denotes the small sectorial area captured using Equation 4.6 and also explained in Figure 4.7.

After completing damage detection Step 1 (Equation 4.5), the area for further study is selected. This is based on the calculation that the value of the selected damage detection method (RMSD, mean absolute error (MAE), etc.) increases for signal paths that are closer to or cross the damage zones. This demonstrates that changes in signals occur as a result of any type of damage. Following the identification of damage-influenced paths, the sectors are determined to perform an SEC-based localization (step 2—Equation 4.6 and are also shown as identified sectors in Figure 4.6).

The sector for which the SEC method is applied is determined with a precision of  $45^\circ$ , which is equal to the angular separation of the sensors on the circumference (a circular sensor arrangement). So, for example, if the S9S2 (9th PZT as actuator and 2nd PZT as a sensor) signal path is found, the sector borders are defined at the neighbouring sensors (S1 and S3). In this way, the algorithm is applied only to isolated sectors, thus reducing the overall calculation time and the grid counts to a great extent.

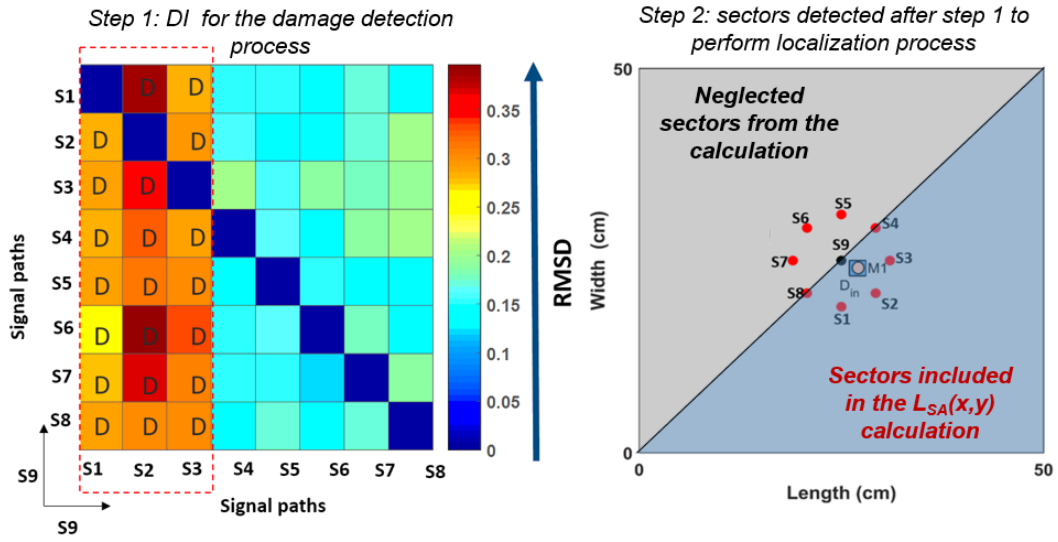


Figure 4.6: Exemplary approach for Step 1-RMSD detection and Step 2-SEC localization.

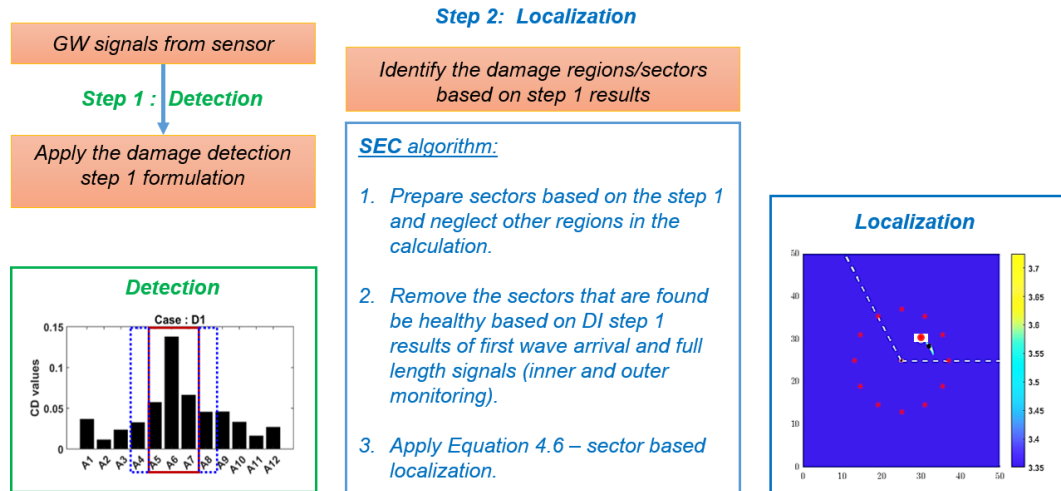


Figure 4.7: Exemplary flowchart of the SEC-SA method.

The defect size can thus be estimated by using image processing techniques, such as carefully choosing a threshold limit, for the defect estimation image (as

shown in Equation 4.4). This is then used in the CM-based pixel quantification approach as explained in Figure 3.5 and also elaborated in subsection 6.1.3.5.

The following are the important improvements in the SEC method;

1. Amplitude peaks from the GW other modes (apart from the fundamental S0, A0 GW modes) and reflections were considered in the study.
2. Improvement in the elliptical algorithm by adding an amplification factor (Equation 4.3) and threshold value (Equation 4.4).
3. Applying the improved elliptical algorithm only to the sector/segmented area (Equation 4.5) obtained from step 1.
4. Applying the method developed to FBG-PZT coupled sensors (chapter 6).

Advantages noticed in using the proposed multi-step methodology;

1. The multi-step methodology is versatile and can be applied to various structures and sensor types for damage identification (till SHM level 3) analysis.
2. The methodology is effective in detecting (step 1) and localizing (step 2) damage present both within and outside the circular sensor networks (elaborated in chapter 6). This means that even if the damage is not located directly within the sensor network, it can still be identified and located accurately.
3. The methodology (step 2) can also identify damage located very near the actuator, which is a significant advantage (chapter 6 and subsection 6.1.3.4).
4. The methodology (step 2) is designed to reduce the number of mesh/grid points required for the calculation, which leads to more efficient and accurate results. This reduction is achieved by dividing the region into sectors (step 1), as shown in Table 6.5.
5. The methodology (steps 1 and 2) offers a good time reduction in the overall calculation, which is beneficial in many applications (Table 6.12).
6. Damage isolation is achieved using a CM-assisted threshold application (step 3). This means that the methodology uses a specific threshold value to isolate the damaged area accurately, as shown in subsection 6.1.3.5) and Figure 6.13.

## Chapter 5

### Elliptical algorithm damage analysis with experimental cases

#### 5.1 ACS: impact damage analysis using LDV scanning points

ACS materials are widely used in the automotive and aerospace industries due to their strength-to-weight ratio. BVID caused by drop impacts or improper tool handling can result in indentations in the material, and ACS core assembly may experience alterations due to core crushing. Innovative solutions involving new materials and designs are being developed to tackle this challenge [108]. This section examines BVID in a semi-sandwich ACS panel using the LDV-based GW method. The A0 mode at 150 kHz accurately predicted damages and was chosen as the primary mode (shown in Figure A.1). An impact force of 4 and 10 J created protrusions, and the acquired data were processed using the elliptical algorithm approach for damage localization. LDV and signal processing techniques were used to investigate the material based on scattered waves.

##### 5.1.1 Methodology

The flowchart in Figure 5.1 illustrates the methodological steps needed to evaluate the ACS using the SHM-GW approach. The SHM analysis employs an array of scanning points (assumed to be PZTs) and the elliptical method to locate the damages. The steps in the procedure include damage visualization and localization.

##### 5.1.2 Details about ACS and damages

A Nomex honeycomb core and an aluminium skin (facet) make up the examined ACS. Low energy (4 and 10 J) impacts from the Nomex core side created the BVID (on the side of the facet). Crushing the Nomex cells produced a BVID with a diameter of 1.4 cm (BVID 1) and removing the Nomex cells

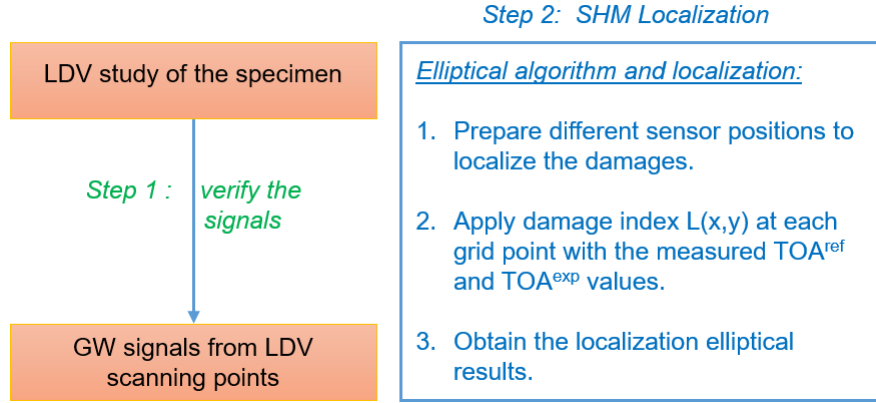


Figure 5.1: Methodological flowchart in ACS analysis.

produced another BVID with a diameter of 1.8 cm (BVID 2). The BVID was produced using a circular impactor with a 10 cm diameter. Apart from the BVIDs, a small hole of diameter 0.5 cm was also introduced to the specimen via drilling. Figure 5.2 depicts the specimen used in the investigation of 50 cm in length and 50 cm in width dimensions. The figure also shows the zoomed BVID 2, and the cross-section of the plate with the Nomex core and an aluminium facet on one side. Figure 5.3 displays the Nomex core attached to the facet along with the location where the BVIDs were created. A bonding epoxy adhesive was used to attach the PZT to the ACS plate. In this thesis research work PZT obtained from *CTS corporation* [84] is used as shown in Figure 1.2 and GW sensing was performed by LDV. The excitation was created by a sine tone burst signal with 10 cycles at 16 V<sub>PP</sub> amplified 20 times. Measurements were carried out in a controlled environment at 21 °C. Table 5.1 provides a summary of the ACS's material properties.

Material	E (Gpa)	$\nu$	$\rho$ (kg/m <sup>3</sup> )
Nomex cell	9	0.30	1384
Aluminium	68	0.33	2600

Table 5.1: Material properties of the ACS.

Where : E is the Young's modulus,  $\nu$  is the Poisson ratio, and  $\rho$  is the density.

### 5.1.3 Damage localization discussion and results

The implementation of the elliptical algorithm (Equation 4.2) in the location of the damage is the main topic of this part. Table 5.2 displays the scenarios with



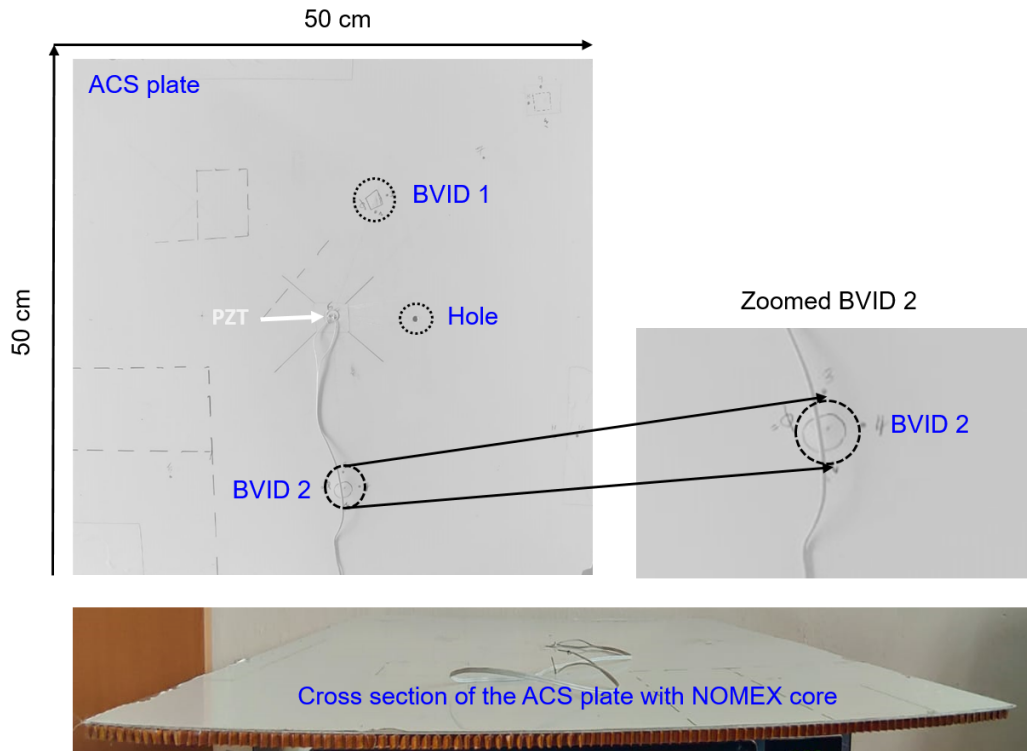


Figure 5.2: ACS facet with damages and cross-section of core ACS.

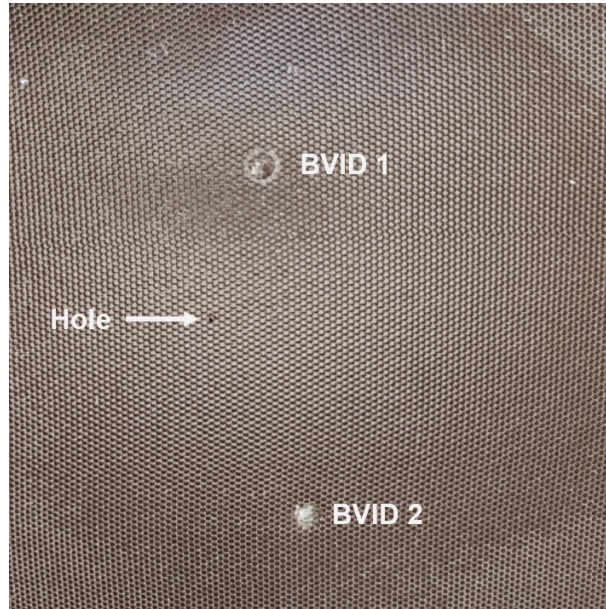


Figure 5.3: ACS backside with Nomex core and damages.

various sensor placements to localize the damage mentioned. Case 1 (Figure 5.4a) is based on optimal sensor placement published in [109]. The scanning points are placed at a distance of 10 cm in each of the cases [75].

Case	Sensor Placement	Sensing points
1	Quadrant I, II, III, IV	P1-P8 (Figure 5.4a)
2	Quadrant I, II	P7-P8, P5-P6 (Figure 5.4a)
3	Quadrant III, IV	P1-P2, P3-P4 (Figure 5.4a)
4	Quadrant II	P1-P6 (Figure 5.4b)

Table 5.2: Case models studied using the elliptical algorithm.

A velocity profile (Appendix subsection A.1.1) must be established for the elliptical algorithm to function because the velocity may be angle-dependent. Beginning with the whole experimental case 1 with two BVIDs and a hole depicted in Figure 5.4a, the elliptical localization approach is used. The region where the damage map maximum is identified is indicated by the junction of white dotted lines in all the figures with results (Figure 5.5). As can be seen in Figure 5.5a, the outcome for case 1 reveals that only the location of the hole was reported. The zone of convergence of energy close to BVID1 was found by scanning points in quadrants I and II (case 2), as illustrated in Figure 5.5b. The zone of convergence of energy close to BVID2 was discovered by scanning points in quadrants III and IV (case 3), as illustrated in Figure 5.5c. In case 4, a different sensor configuration (quadrant II; Figure 5.4b) revealed where the hole was (Figure 5.5d).

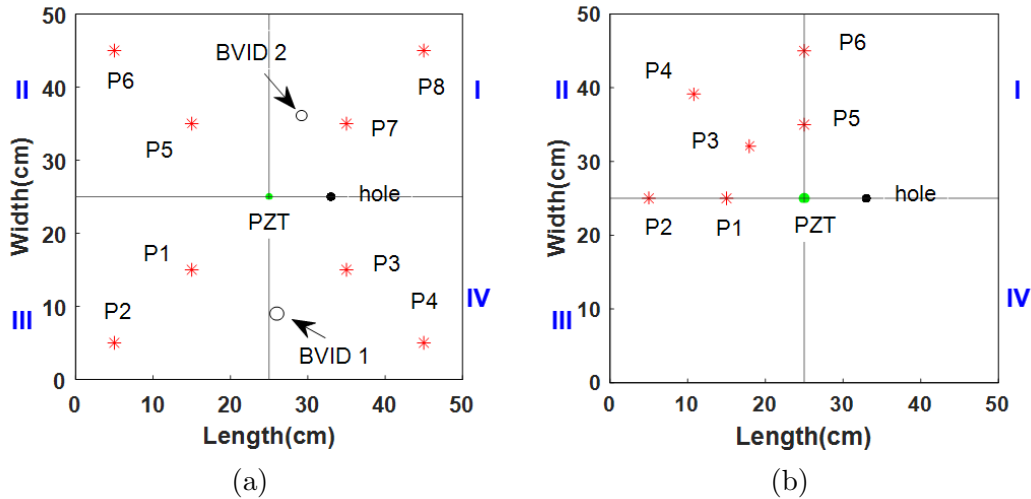


Figure 5.4: Sensor arrangements: (a) Case 1 quadrant I-IV, (b) Case 4 quadrant II.

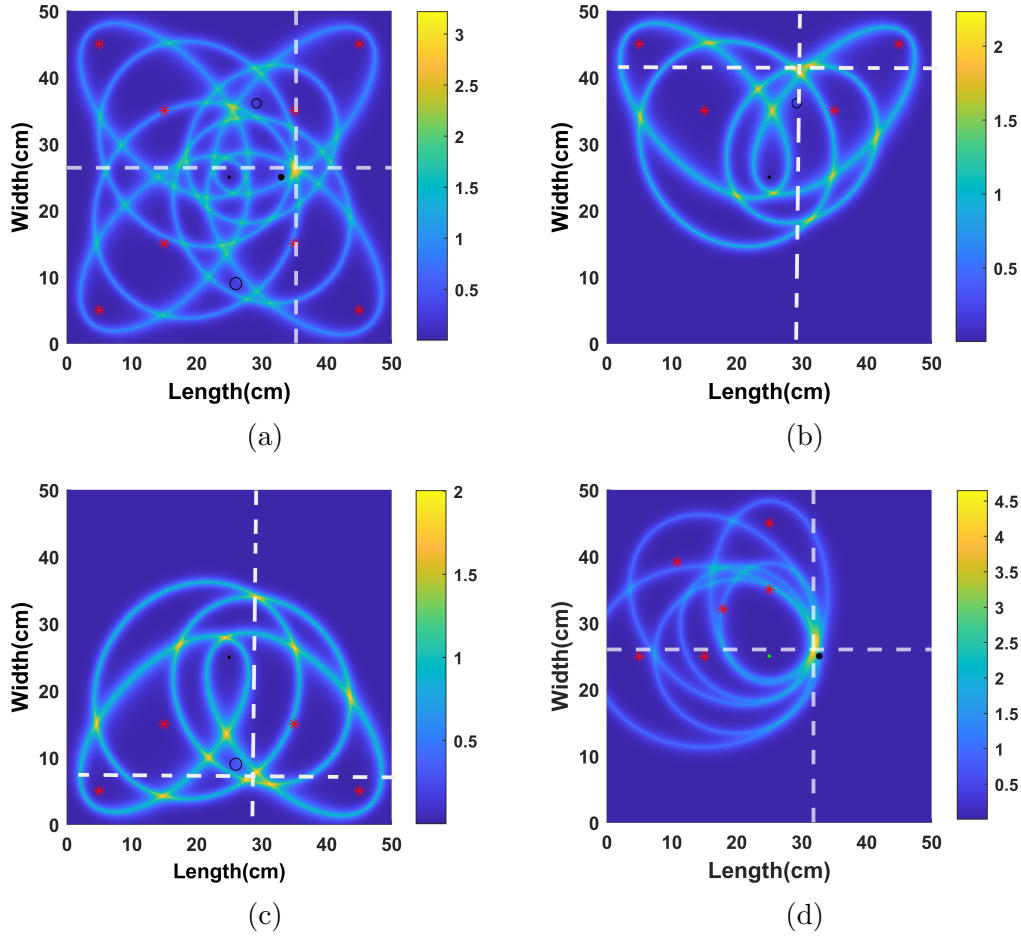


Figure 5.5: Experimental elliptical algorithm results with different sensor arrangements: (a) Case 1, (b) Case 2, (c) Case 3, (d) Case 4.

The elliptical algorithm results (values in cm) are compared to the original damage coordinates and are grouped together in Table 5.3. The error was low as 0.22 cm and proves that sensor placements of semi-circular sensing positions (Figure 5.4b) are better in predicting the damage coordinates. The circular sensor placement is studied in detail in the later part (chapter 6).

#### 5.1.4 Sectional conclusion

Testing for low-energy impact damage on the ACS was performed using the LDV GW visualization method. To pinpoint the locations of multiple damage sites using only a few sensing points, an SHM investigation was conducted using an elliptical algorithm. Overall, the combination of LDV and SHM-GW using an elliptical algorithm is used for detecting and locating the damages.

Case studies	Damage coords (cm)	Estimated coords (cm)	Error (cm)
Case 1	(33.0, 25.0)	(34, 26.2)	1.56
Case 2	(29.1, 36.2)	(29.1, 41)	4.8
Case 3	(26.0, 9.0)	(27.7, 7.7)	2.14
Case 4	(33.0, 25.0)	(33.2, 25.1)	0.22

Table 5.3: Error estimated using the elliptical algorithm.

## 5.2 GFRPS: Multiple BVID analysis using LDV scanning points

As a result of their lightweight and corrosion resistance, GFRPS are frequently used in civil and mechanical domains. However, a small impact hit with relatively little energy can cause harm to these structures. The goal of this section of the thesis is to use GW-based SHM tools to locate and identify multiple BVID damages in a GFRPS. In this study, GW measurement based on LDV is used. To efficiently pinpoint damages, a threshold-based elliptical algorithm was implemented. Research on damage detection has primarily focused on detecting a single damage location [110], [111], [61], while there is relatively less research on detecting and evaluating multiple-site damage, which can occur when a structure experiences numerous closely spaced impacts. However, since multiple-site damage can be equally critical to a structure's safety, researchers are exploring new methods to improve its detection and evaluation. To illustrate the multiple damage locations, LDV signal data was processed using the RRMS technique. Using SHM elliptical algorithm threshold method, multiple damage coordinates were localized effectively.

### 5.2.1 Methodology

The methodological steps involved in assessing the GFRPS utilizing combined SHM and NDT techniques are explained in the flowchart shown in Figure 5.6. Damage detection and localization are the steps in the process. The LDV signals from the healthy and damaged states are subjected to the RRMS (Equation 2.3). In the preliminary research, damages are visualized using RRMS. The next step is SHM analysis using a series of scanning points (assumed to be PZTs) and the elliptical algorithm to determine the coordinate locations of multiple linear damages with a threshold limit.

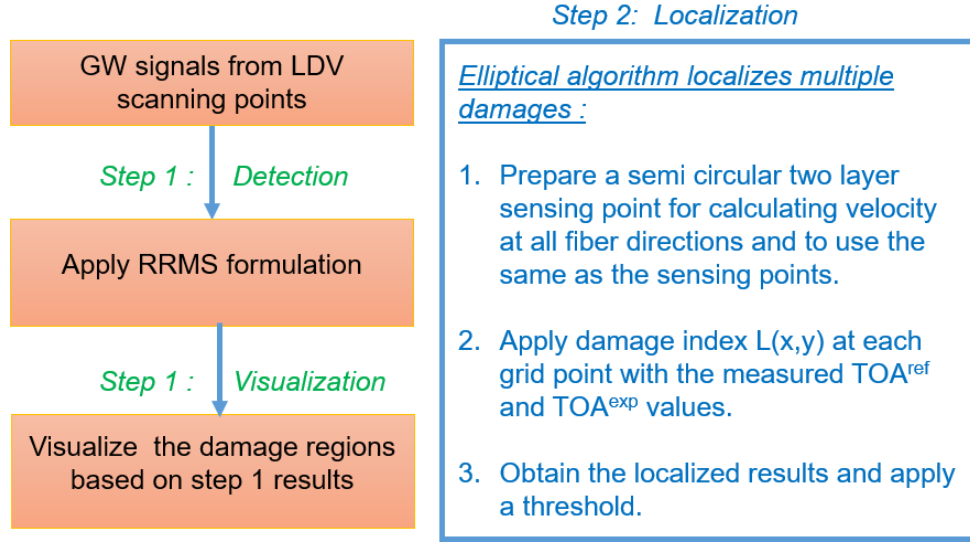


Figure 5.6: Methodological flowchart in GFRPS analysis.

### 5.2.2 Details about GFRPS and damages

The 12 layups of the 0.2 cm thick GFRPS (procured from [112]) are stacked in a  $[0/90]_{3s}$  configuration and bonded together by *HEXCEL-212Na* adhesive. The mechanical and construction industries are the main users of these materials. The GFRPS has dimensions of 50 cm in length, 50 cm in width, and 3 cm in thickness. With an impact force of 20, 25, and 30 J, several linear BVIDs of diameter 0.9 cm (BVID1), 1.2 cm (BVID2) and 1.3 cm (BVID3) are produced. To do this, a steel ball attached to a steel beam is dropped at various heights while being guided by a pipe [75]. Cyanoacrylate glue is used to attach all four PZTs (each measuring 1 cm in diameter and 0.1 cm thick) to the GFRPS and to excite GWs that are detected by the LDV at various scanning points. Figure 5.7 shows the positions of PZT1-PZT4 and BVIDs.

### 5.2.3 Damage localization discussion and results

RRMS investigations are carried out using LDV data to visualize the damage. All computations are performed using a constant power/weight factor value of  $a = 0.5$  (Equation 2.3). It was found that the LDV RRMS 200 kHz graphs were able to distinguish all the BVIDs (Figure 5.8) after checking the frequencies 50 to 200 kHz in 50 kHz steps. Hence, SHM research is limited to a frequency of 200 kHz. After checking the RRMS results from PZT1 (Figure 5.8), similar BVID identification, and visualization checks were also done for other symmetrically located sensors, as shown in (Figure 5.9), using the RRMS based weightage formulation.

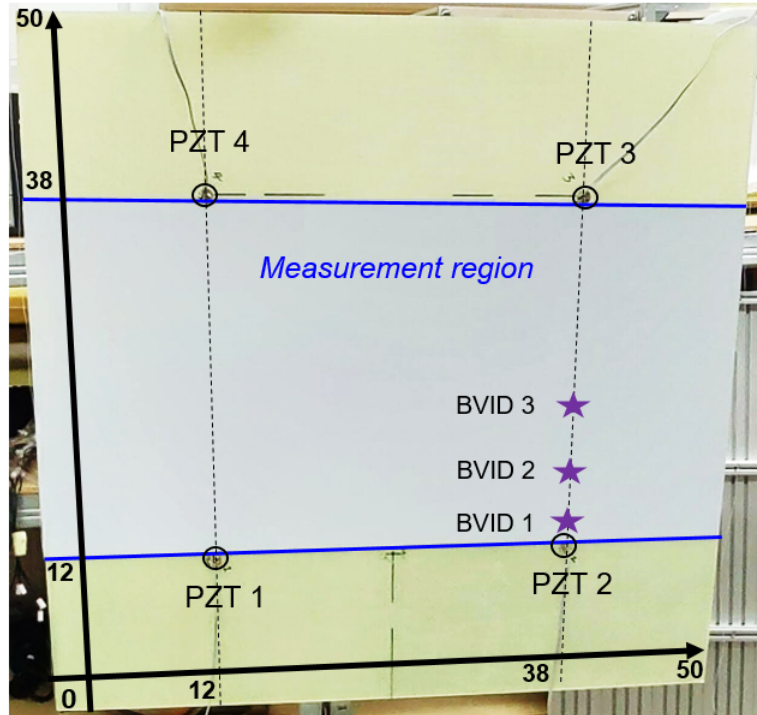


Figure 5.7: GFRPS with PZT positions and BVIDs.

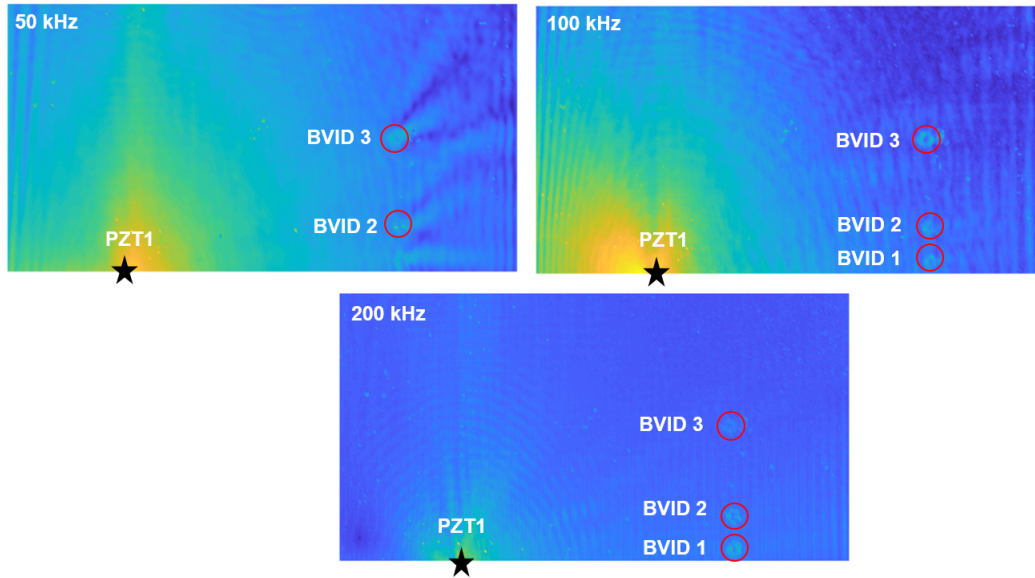


Figure 5.8: LDV-RRMS plots excitation from PZT1 at different frequencies.

The elliptical algorithm uses a threshold value (90%) to segregate the higher values in the grid during the run (Equation 4.4). In this study, the threshold value was based on engineering judgment and previous experience. Usually, a large number of measurements in different operational conditions would be



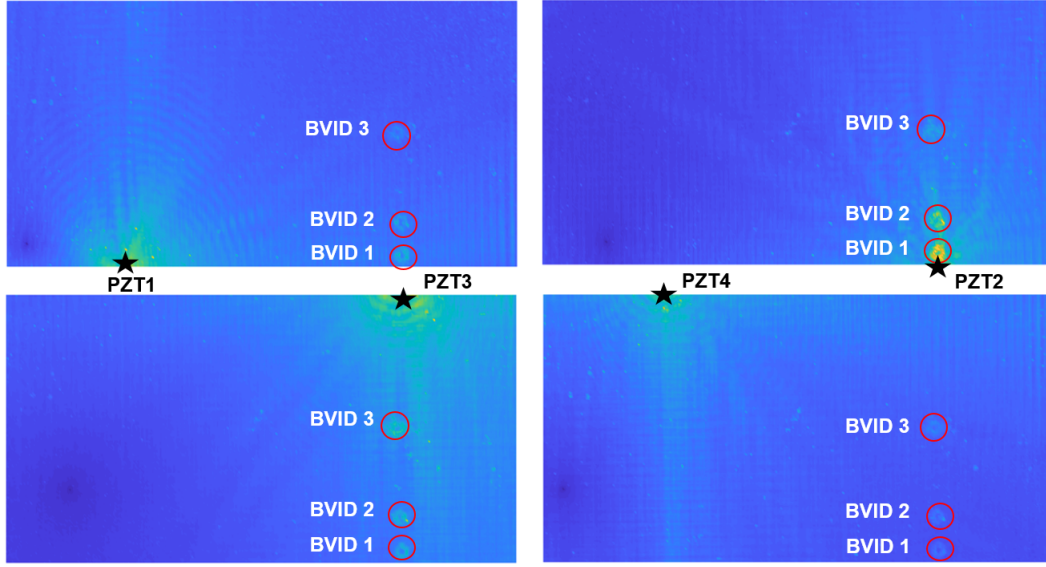


Figure 5.9: LDV-RRMS plots excitation for 200 kHz from PZT1-PZT4.

needed to establish a better threshold value. In the later part of the study, a sensitivity-assisted CM method (step 3 as shown in subsection 6.1.3.5) is developed to arrive at the threshold value. For the purpose of locating damage, the elliptical algorithm with amplification and threshold factor addition is performed on GW signal data. Using PZT1 (Figure 5.10) as an excitation source, the equidistant nodal points (P1–P10) are extracted from the results of the LDV area scan. PZT2 and PZT3 are not taken into account for the SHM investigation because they are in a straight line with respect to the detected damages.

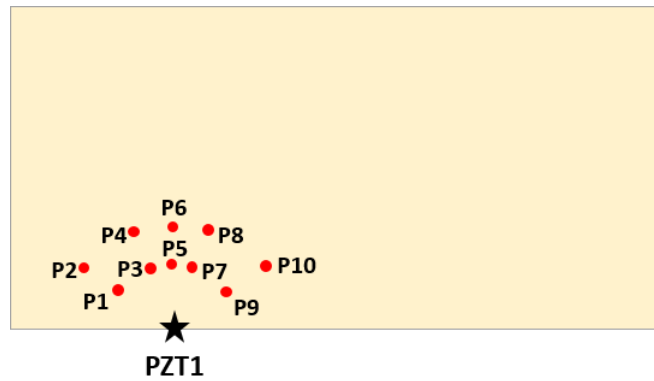
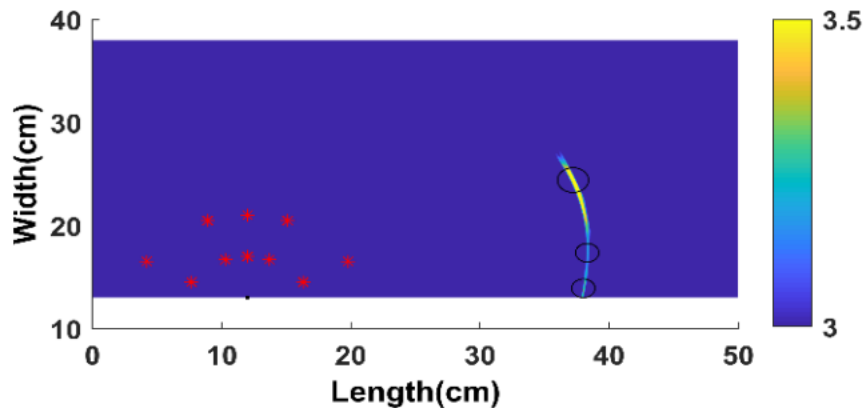


Figure 5.10: Distribution of circular scanning nodal points for SHM study.

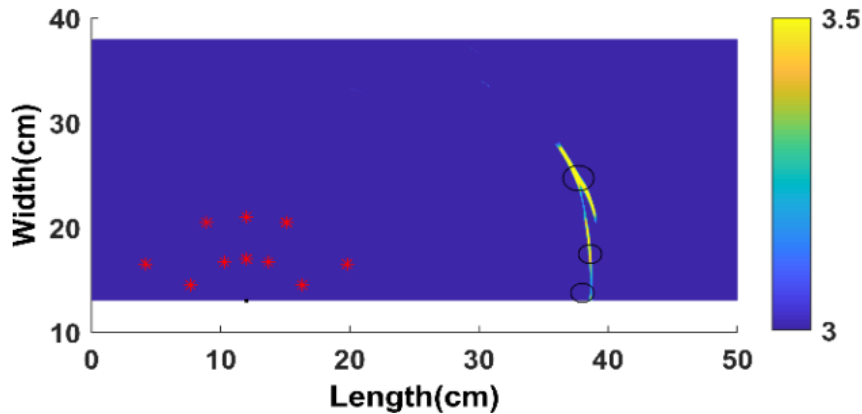
As stated above, the frequency selected for this study is 200 kHz. The A0 GW mode was chosen for future analysis based on the results shown in [82]

on a similar GFRPS analysis. For the computations, the velocity values of the A0 mode for the LDV acquired from the scanning sites at  $90^\circ$  and  $0^\circ$  are 2231 m/s and 1768 m/s, respectively. By fitting the velocity measurements to an elliptical function and calculating the  $360^\circ$  velocity profile, the velocity profile is obtained (as shown in Appendix A.1.1). SEM numerical data obtained from [113] was also checked as an additional process to verify the effectiveness of the algorithm. The velocity values obtained from the SEM calculations are 2135 m / s and 1677 m / s for  $90^\circ$  and  $0^\circ$ , respectively.

Figures 5.11a and 5.11b display the damage localization graphs. Higher energy zones are isolated with threshold values on the maps that were plotted. The area demonstrates that the newly produced BVIDs are closer to higher energy (circled in black). Tables 5.5 and 5.4 are used to display the error estimation. The results obtained are within a maximum error marginal range of less than 1 cm difference and are closer to the BVID zones.



(a)



(b)

Figure 5.11: Localization threshold results (a) SEM data,(b) LDV data.



<b>LDV</b>	<b>BVID1</b>	<b>BVID2</b>	<b>BVID3</b>
Damage coords (cm)	(38,14)	(38,17.5)	(38,24)
Estimated coords (cm)	(38.3,13.9)	(38.3,17.3)	(37.2,24)
Error (cm)	0.32	0.34	0.89

Table 5.4: SHM elliptical threshold damage localization on LDV data.

<b>SEM</b>	<b>BVID1</b>	<b>BVID2</b>	<b>BVID3</b>
Damage coords (cm)	(38,14)	(38,17.5)	(38,24)
Estimated coords (cm)	(38.7,13)	(38.6,17)	(37.7,24)
Error (cm)	0.74	0.60	0.76

Table 5.5: SHM elliptical threshold damage localization on SEM data.

#### 5.2.4 Sectional conclusion

In this section, an SHM-GW method was proposed for detecting and locating multiple BVIDs in GFRPS. The method utilized a threshold-based elliptical algorithm. The experiments were conducted using a 200-kHz frequency range. The results of the RRMS investigations identified damaged locations, even in areas of higher energy. The data from PZT1 was analyzed thoroughly, and scanning points were taken to examine the damage zones. The error range was found to be less than 1% in all cases analyzed, as demonstrated in Tables 5.4 and 5.5. The estimated error in all cases showed that the proposed method was effective in accurately detecting and localizing multiple BVIDs in GFRPS.

## Chapter 6

### SHM-GW common method: damage identification analysis

#### 6.1 SCS: multiple debond identification using PZTs

The scenarios in which the debonding is very close to the sensor have not been thoroughly investigated in the literature survey. Cases involving multiple damages (e.g., debonding, impact combined) in the SCS were not thoroughly investigated. The research in this section is motivated by the desire to investigate and solve the aforementioned scenarios using a multistep GW approach involving damage detection, localization and quantification methods. The study focuses on inspecting the SCS that has multiple damages (debonding and artificial mass placements). In the SCS, debonding of varying sizes and magnets placed in different locations are considered damages. To analyze these damages, a circular sensor network is built. The damage detection step 1 aids in determining which sectors are vulnerable to damage. It is accomplished by employing a quick RMSD-based formulation to detect the damaged regions (i.e., sectors) based on RMSD variation.

The improved SEC with effective path coverage is applied to sectors identified in the damage detection step 1 to pinpoint the location of the damage. The methodology is developed and improved over the state of the art to include the inside and outside localization of damage by taking threshold values from the healthy structure. Thus, using the localization step, damages near the actuator, far from the actuator, and multiple damages were successfully localized. Because only the precise localization is performed in sectors with the identified damage, the proposed multistep approach reduces the computational cost. It is discovered that the proposed SHM strategy is capable of locating hidden debonding regions and damages in the SCS. The quantification of the damages using the CM term TPI (total positive index) is added as step 3 which requires the results of step 2.

### 6.1.1 Methodology

A multi-step SHM process is proposed to analyze the damage present inside and outside the sensor network (refer to Figure 7.1). Figure 6.1 shows a graphical methodological illustration of the procedure. The flowchart is an elaborated flowchart mentioned in Figure 4.7 and includes steps to classify damage regions' outer, inner and combined localization strategies. The quantification is added as step 3. The sensor network is formed by a circular arrangement of 9 PZTs (1 actuator, 8 sensors-based configurations). Such circular PZT configuration is also proposed and continued in the hybrid FBG PZT configuration studies (sections 6.3, 6.4). The configuration helped to overcome many limitations (mentioned in subsection 3.1) and localized multiple damages effectively.

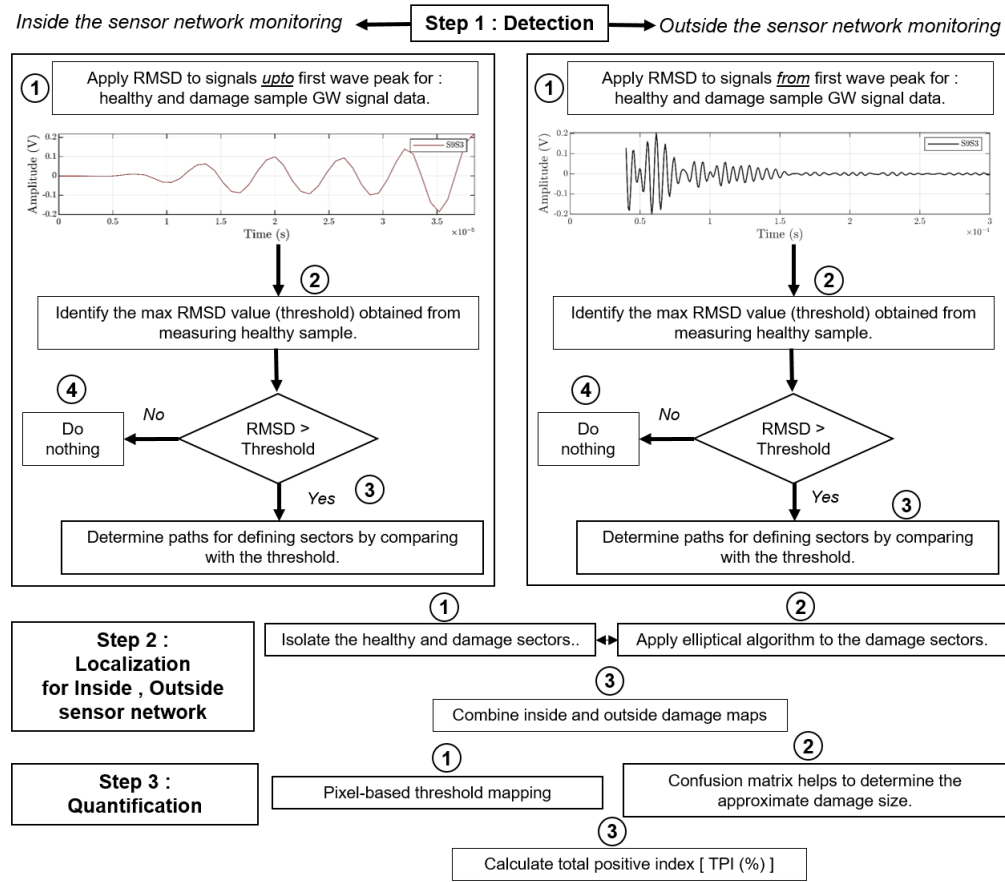


Figure 6.1: Proposed common multi-step methodology in damage identification analysis.

- Damage detection step 1: It is used to determine whether the damage is internal or external to the sensor network. The detection is performed by comparing the RMSD value obtained from a damaged specimen against a healthy sample (as shown in [57]). To detect the damage within the

sensor network DI up to first wave arrival is considered and for detecting damage outside the sensor network full-length signal is considered.

- Damage localization step 2: SEC-based localization is used to obtain damage coordinates in the specified sectors. This step also combines the results of inside and outside monitoring. If there is no damage inside, the output is outside the localization result and vice versa.
- Damage quantification Step 3: This step uses CM terms to arrive at the approximate threshold which in turn estimates the damage size.

### 6.1.2 Details about experimental setup, SCS and damages

PZT was used in the GW study to excite and sense the waves. A DAQR setup (previously shown in Figure 2.14) was used to conduct laboratory experiments on a sample SCS (50 cm  $\times$  50 cm  $\times$  0.7 cm). Figure 6.2 shows the experimental setup, which includes a DAQR system, sample SCS, a cross-sectional view, and a network of PZTs. The aluminium SCS honeycomb core has a thickness of 0.5 cm and a cell size of 1/8 inch. As face sheets, the 0.1 cm thin CFRP laminates layup  $[0/90]_{3s}$  are bonded to the core with *HEXCEL-212Na* adhesive. The SCS is made up of two debonding: D1 (2 cm square area with centre coordinates 39 cm, 19.5 cm) and D2 (0.5 cm square area with centre coordinates 15.5 cm, 28.5 cm). Debonding was introduced during manufacturing without the use of adhesive in some areas between the CFRP laminate and the aluminium core. Later in the experiment, a magnetic mass (1.5 cm diameter and 10 g weight) was placed at three different locations, as shown in Figure 6.3 as M1 (located at the centre coordinates 27 cm, 24 cm), M2 (located at the centre coordinates 30 cm, 33.5 cm), and M3 (located at the centre coordinates 30 cm, 33.5 cm). The experimental cases investigated are shown in Table 6.1.

Cases	Damages
1	D1 and D2
2	M1 with D1 and D2
3	M2 with D1 and D2
4	M3 with D1 and D2

Table 6.1: Experimental cases studied.

Along with this, four other cases were investigated [57] using data from numerical simulations (data taken for validation purposes only) with models in the

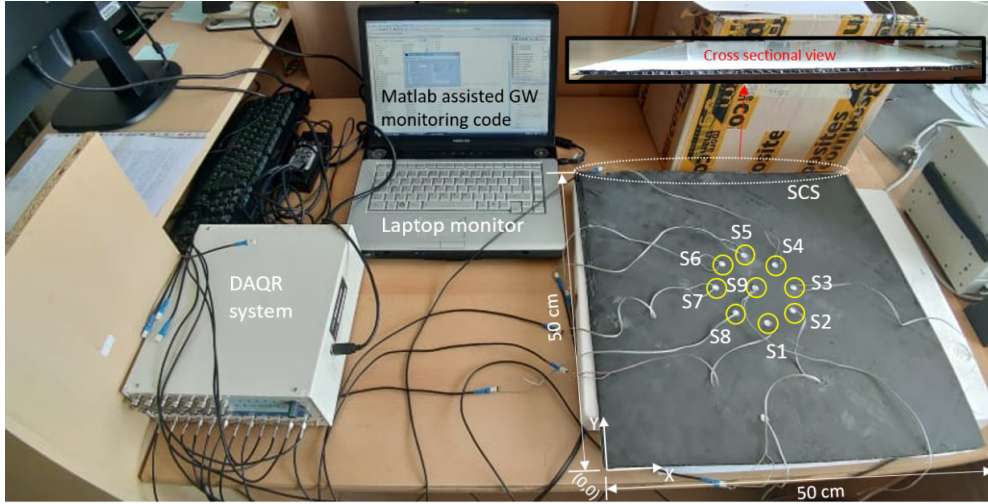


Figure 6.2: Experimental setup with DAQR.

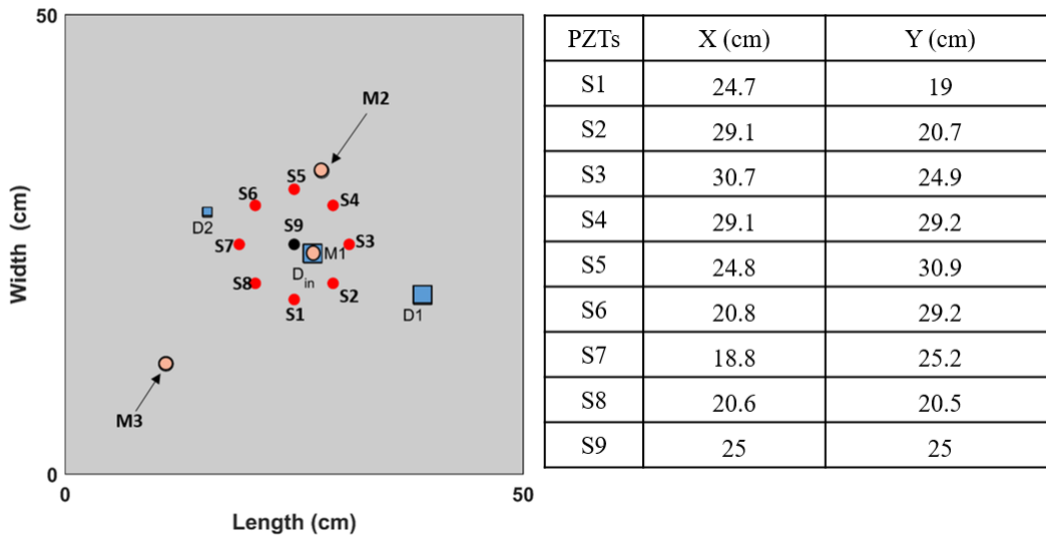


Figure 6.3: Schematic representation of the SCS with debonding [square] and artificial masses [M], positions (coordinates of the centre) of PZTs.

healthy state,  $D_{in}$ ,  $D1$ ,  $D2$ , and  $D1$  alone.  $D_{in}$  is located at the coordinates 27 cm, 24 cm in the centre.  $D_{in}$  is a new debonding model (which does not exist in the experiment) that is used to investigate the proposed SEC approach for a damage case closer to the sensor network. To prevent external vibration, the SCS was placed on a polyurethane thermoform sheet. The PZTs were actuated with a 5-cycle sine Hanning pulse with frequencies ranging from 25 to 250 kHz (in steps of 25 kHz) for the experimental study. The PZT network is made up of 9-PZTs that are bonded to the SCS using a cyanoacrylate-based adhesive. The 8 PZTs (sensors S1-S8) in the network are arranged in a circular

array around a centric PZT (i.e., S9-actuator) with a radial distance of 6 cm. Excitation was handled by the S9, while sensing was handled by the S1-S8.

### 6.1.3 Results and discussion

This section discusses all the frequencies investigated in the experiment, as well as the process of determining the optimal frequency.

#### 6.1.3.1 Choice of the GW mode and frequency

Amplitude values are calculated by selecting the maximum peak values of A0 mode for all frequencies measured with DAQR ranging from 25 kHz to 250 kHz. The A0 mode was chosen for the study because it detected debonding (based on reflection and interference phenomena) when visualized with LDV-based GW-FWF studies (as shown in Appendix Figure A.4). Another reason is that, due to the higher propagation velocity, S0 mode sometimes gets mixed up with the initial excitation (cross talk) and is not always identifiable. Figure 6.4 shows one method for obtaining the A0 mode amplitude value for the S9S1 (excitation at sensor S9 and sensing at sensor S1) with an HT envelope. Figure 6.5 shows the amplitude (vs) frequency plot for the actuator S9 and sensors (S1-S8) over the entire 25-250 kHz range. The amplitude plot demonstrates that the maximum amplitude response is obtained at 150 kHz and is visible with all eight sensors. As a result, the 5-cycle, 150 kHz frequency range is chosen as the excitation frequency in the following section of the experiment.

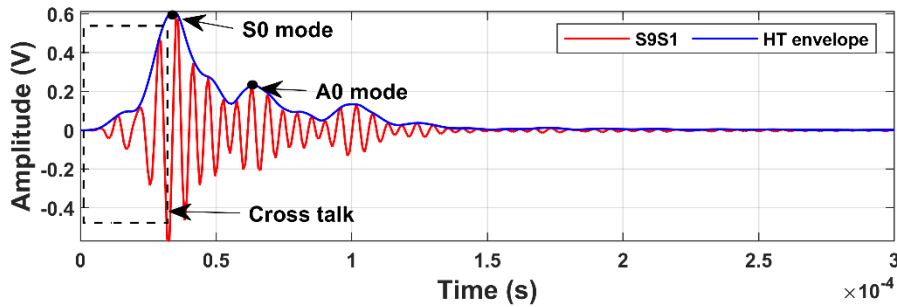


Figure 6.4: Peak peaking of A0 mode from 150 kHz excitation.

#### 6.1.3.2 Damage detection step results: Step 1

This section concerns the damage detection step of the four experimental cases studied. The experimental case consists of the initial state debonding (case 1 in Table 6.1). To further evaluate the proposed multi-step methodology, three cases with artificial mass placements are added (cases 2, 3, 4). According to

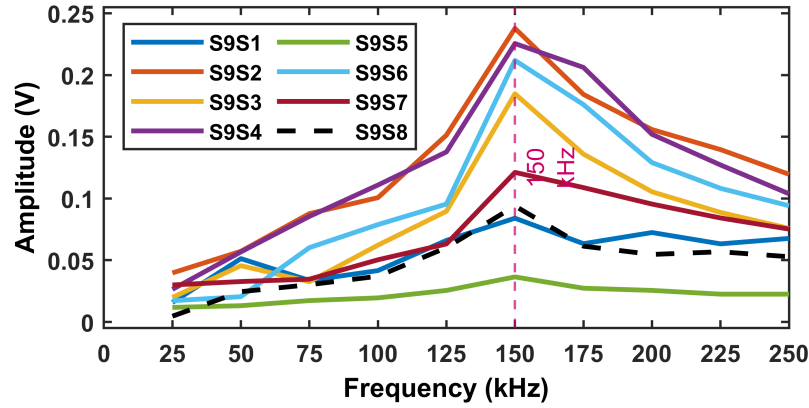


Figure 6.5: Amplitude (vs) frequency plot of A0 mode.

the findings of the experimental case study, (Figure 6.6 and Table 6.2), case 2 experimental models use the inside monitoring technique (cut of signals up to first peak maximum), and M1 is identified in the inner sensor network area. In cases 3,4, the matrix maps showed similar values below the threshold values, implying that no damage is present within the sensor network. Table 6.3 and Figure 6.7, scenarios observed scenarios in the experimental case study. The term 'D' in the figures represents the probable damage regions obtained in the damage detection step.

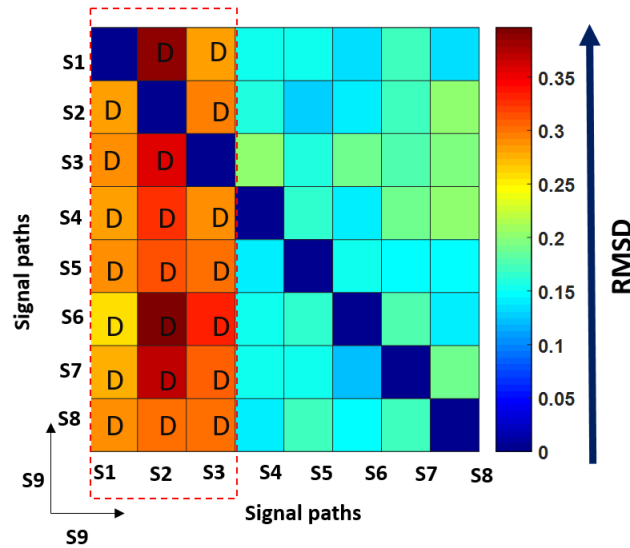


Figure 6.6: Damage detection step for inside monitoring: DAQR results of Case 2.

Case	Figure	Higher RMSD columns	Identified damage
2	6.6	S9S1, S9S2, S9S3	M1

Table 6.2: Damage detection step for inside monitoring: DAQR data.

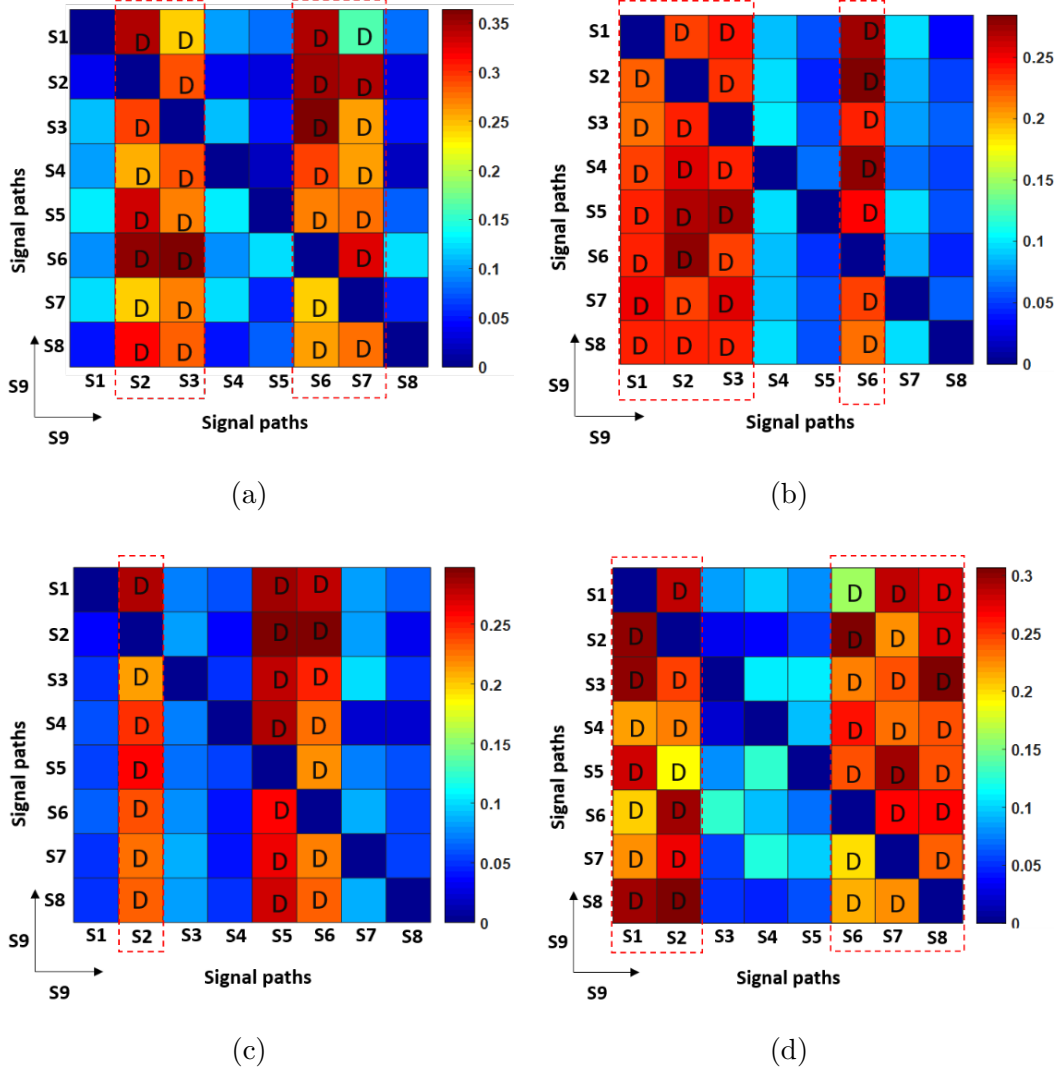


Figure 6.7: Damage detection step for outside monitoring: DAQR experimental: (a) Case 1, (b) Case 2, (c) Case 3 and (d) Case 4.

### 6.1.3.3 Damage localization using SEC: Step 2

Figures 6.8 and 6.9 show the experimental SEC results for the identified sector results (Figure 6.7 a-d). As previously stated, Figure 6.7(b) is an example of how the RMSD matrix maps showed damage inside and outside the sensor network (case 2 with M1, D1 and D2) with higher value column sectors, neces-



Case	Figure	Higher RMSD columns	Identified damage
1	6.7a	S9S2, S9S3, S9S6, S9S7	D1, D2
2	6.7b	S9S1, S9S2, S9S3, S9S6	M1, D1, D2
3	6.7c	S9S2, S9S5, S9S6	M2, D1, D2
4	6.7d	S9S2, S9S3	M3, D1, D2

Table 6.3: Damage detection step for outside monitoring: DAQR data.

sitating the use of a combined final step  $45^\circ$  sector separation scheme (Figure 6.8c) to reduce the calculation time in localizing the damage present inside and outside the sensor network. Figure 6.8a, which shows the SEC results for DAQR data with D1 and D2 (case 1), shows the location of debonding where the ellipses intersect. Because of the intersection of the ellipses, this is the region of higher energy. Case 2 SEC results show M1 inside the sensor network and D1, and D2 outside the sensor network (Figure 6.8c). Figure 6.9a identifies D1, D2, and M2 from Case 3, followed by Case 4 (Figure 6.9c), which identifies D1, D2, and M3, respectively. The threshold value is applied to sectorial Figures 6.8(a,c), 6.9(a,c) in order to display only the damage locations shown in Figures 6.8(b,d), 6.9(b,d) respectively.

The numerical results from the FEM calculations are also checked with the SEC step 2 localization algorithm to check the efficiency of the SEC method in localization. The numerical SEC results for the identified sectors are shown with intersecting ellipses indicating the location of debonding (Figure 6.10). The obtained velocity profile is shown in Appendix A.2 w.r.t SEC calculations in the debond analysis. Figure 6.10 analysis shows the region of higher energy obtained from the intersection of the ellipses. The models from the Abaqus are studied with the developed SEC algorithm for verification purposes. Figure 6.10a identifies the  $D_{in}$  using a combination of sector schemes (angular and circular), while Figure 6.10c identifies both D1 and D2. SEC results of the D1 alone model are shown in Figure 6.10e. For  $D_{in}$  numerical study first SEC angular sector was used, but since in this case direct first wave peak was employed, a circular section was also made even shortening the sectors to reduce the calculation time. To show only the damage locations in Figure 6.10, a threshold percentage value of 75% is applied to sectors Figure 6.10(a, c, e) to obtain Figure 6.10(b, d, f). The threshold value was determined using miss-hits and threshold calculations, as shown in [86].

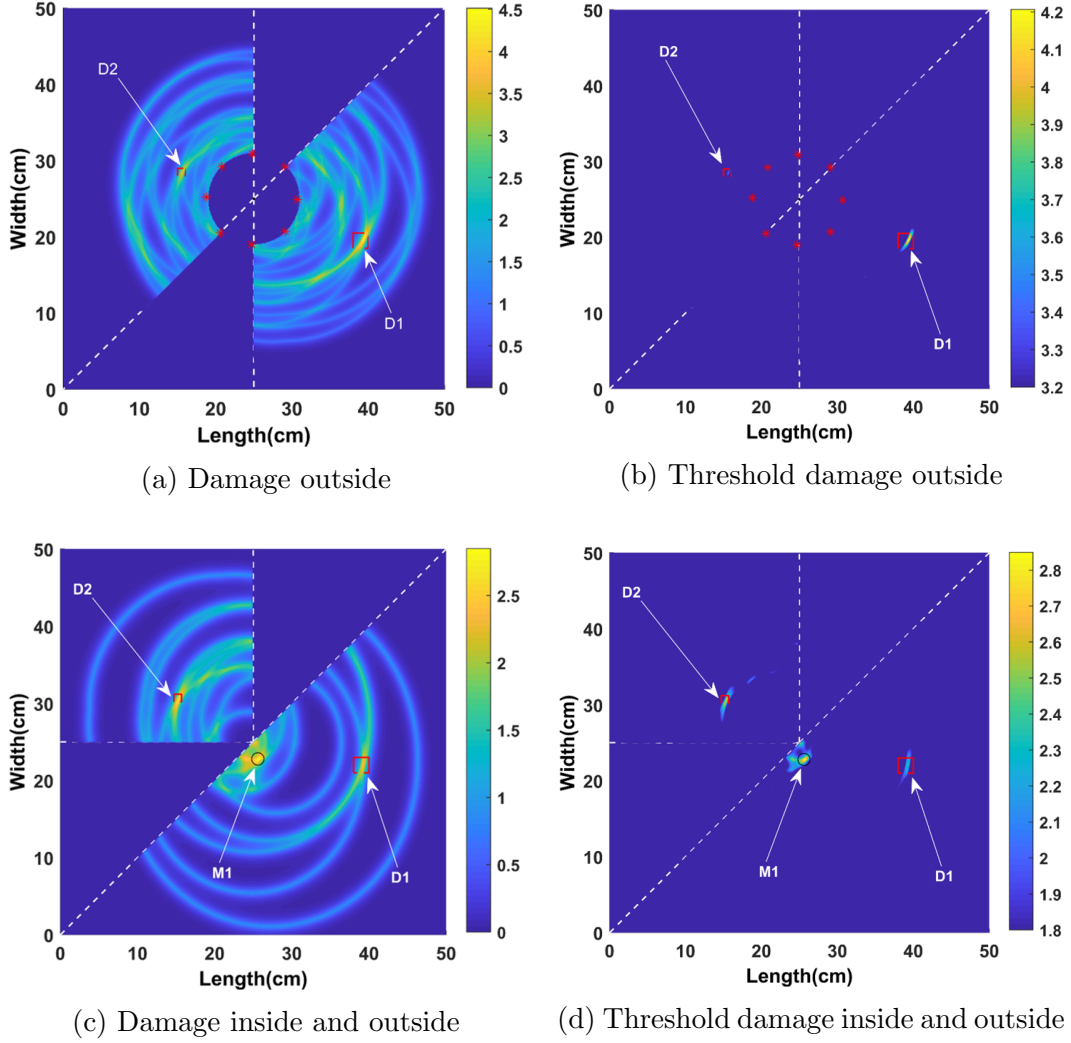


Figure 6.8: SEC experimental results: (a) Case 1, (c) Case 2, Threshold of SEC results: (b) Case 1 (d) Case 2.

#### 6.1.3.4 Computational efficiency and accuracy studies

The original debonding and mass locations with the estimation locations from the SEC method are shown in this section. Table 6.4 shows the estimated location (centre coordinates) of SEC values, and the error estimation ( $\delta P$ ) represents the difference between the estimated location and the actual location using experimental data. Table 6.5 shows the overall reduction in the grid points and time in minutes using experimental data. The actual centre coordinate of D1 is at (39 cm, 19.5 cm), D2 is at (15.5 cm, 28.5 cm), M1 is at (27 cm, 24 cm), M2 is at (30 cm, 33.5 cm), and M3 is at (12 cm, 12.5 cm) respectively.

Studying the values obtained from Table 6.4, one can see that the localization

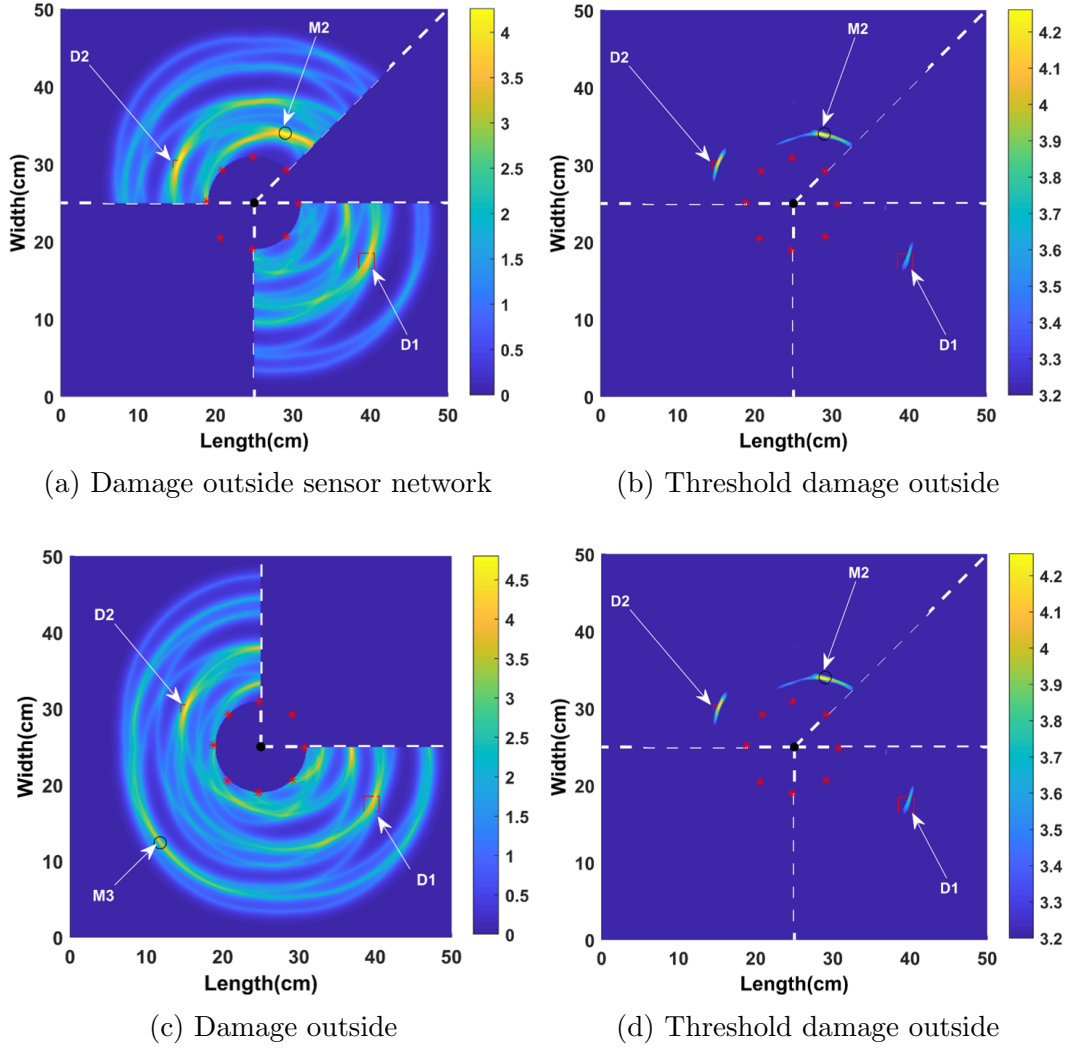


Figure 6.9: SEC experimental results: (a) Case 3, (c) Case 4, Threshold of SEC results:(b) Case 3, (d) Case 4.

Case	SEC D1	SEC D2	SEC M1	SEC M2	SEC M3	$\delta P$ D1	$\delta P$ D2	$\delta P$ M1	$\delta P$ M2	$\delta P$ M3
1	40.1, 20.3	16.9, 29.3	-	-	-	1.3	1.6	-	-	-
2	38.8, 21.1	15.2 ,29.4	26.6, 22	-	-	1.6	0.9	1.4	-	-
3	39.6, 17.9	14.8, 29.0	-	29, 34	-	1.7	0.8	-	1.1	-
4	39.8, 17.8	15.0, 29.8	-	-	11.6, 12	1.8	1.3	-	-	0.8

Table 6.4: Experimental cases: damage localization and error estimation.

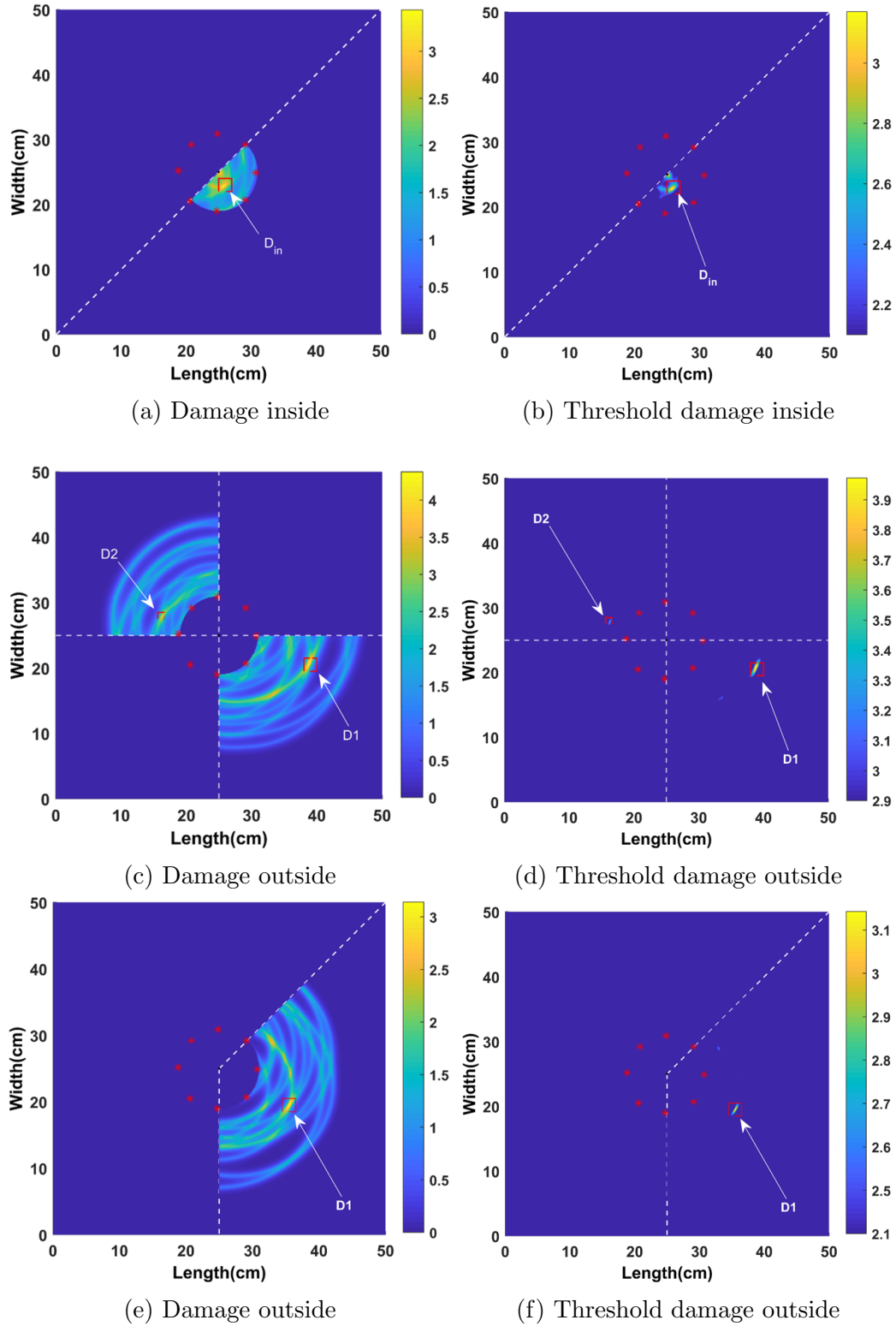


Figure 6.10: SEC numerical results: (a) Case 6 (c) Case 7 and (e) Case 8.  
Threshold of SEC results: (b) Case 6 (d) Case 7 and (f) Case 8.

Case	Points without SEC	Points with SEC	Reduction in grid points	Time without sectors	Time with SEC
1	251001	179992	28.29	13.1	8.5
2	251001	201052	19.89	12.6	8.9
3	251001	150227	40.14	12.9	6.8
4	251001	179594	28.44	13.4	8.3

Table 6.5: Experimental case study: grid points and time reduction.

precision was good, and in the case of larger debonding (D1), the error is less than the edge length of the debonding (2 cm). This proves to be handy in later NDT studies, where only a short region can be scanned to verify the damages. Similar studies were also carried out for numerical cases, as shown in Table 6.6 and Table 6.7, showing good localization result values (all units in cm) similar to experimental results. Since case 5 (numerical results) is a healthy model, it is not shown in the table of calculations. The entire numerical calculations were performed using MATLAB (R2020a) on a desktop PC, Intel i7 processor with 32 GB RAM.

Case	SEC D1	SEC D2	SEC M1	$\delta P$ D1	$\delta P$ D2	$\delta P$ $D_{in}$
6	-	-	26, 22.8	-	-	1.56
7	38.5,20.5	16.5,29.1	-	1.11	1.16	-
8	39.6,17.9	-	-	1.92	-	-

Table 6.6: Numerical cases: damage localization and error estimation.

Case	Points without sectors	Points with SEC	Reduction in grid points	Time without sectors	Time with SEC
6	251001	5600	97.76	12.6	4.3
7	251001	119856	52.24	12.8	6.9
8	251001	89883	64.19	12.5	6.1

Table 6.7: Numerical case study: grid points and time reduction.

### 6.1.3.5 Damage quantification using CM: Step 3

The TPI-based damage quantification was carried out in SCS. Based on the calculation of miss-hits and TPI of pixel counts shown in Equation 6.1, a threshold value of 75% was chosen for damage localization. The best threshold percentage is determined by the percentage with the fewest miss-hits (false predictions). This indicates the pixels that correspond to damage and are regarded as damaged pixels (true positive). Figures 6.11, 6.12 present the various threshold (%) values plotted to determine which percentage had the lowest miss-hit values.

$$\text{TPI [\%]} = \frac{D_e}{D} \quad (6.1)$$

Where:  $D$  is the actual debond size (in pixel numbers), denoted by a red square of D1 in Figure 6.10e of size  $30 \text{ mm} \times 50 \text{ mm} = 1500$  pixel numbers,  $D_e$  = SEC estimated size (after threshold) of the pixel numbers present within the  $D$ .

In Figure 6.12, 75% of the threshold covers the best possible  $D_e$  for  $D$ . ' $D$ ' pixel number is significantly lower within the 80% range in Figure 6.12b. Figure 6.13(a) shows 80% of mishits are zero, but TPI is lower than the previous threshold percentage (75% in Figure 6.13(b)). Table 6.8 estimates errors based on binary pixels from threshold maps compared to  $D$  pixel numbers. Figure 6.11(a-c) is excluded in Table 6.8 due to a high number of distributed mishits. Thus, 75% is selected as the desired threshold to minimize mishits.

### 6.1.4 Sectional conclusion

This section presents the ultrasonic GW propagation characteristics and a multi-step debonding assessment approach for the SCS. The study is also expanded to assess the damage (magnets) placed at various locations in the SCS. The amplitude curves obtained are based on the experimental signals that indicate the presence of multiple GW modes in the registered GW signals at 150 kHz. From the analysis of the results, the following findings are drawn. The presence of debonding in SCS significantly changes the amplitude of the A0 wave mode. This objective of the research is not only focused on the detailed assessment of the damage that is away from the actuator-sensor arrangement but also when present at a close distance, identifying multiple damages using RMSD based matrix map method, localizing the damages with reduced cal-

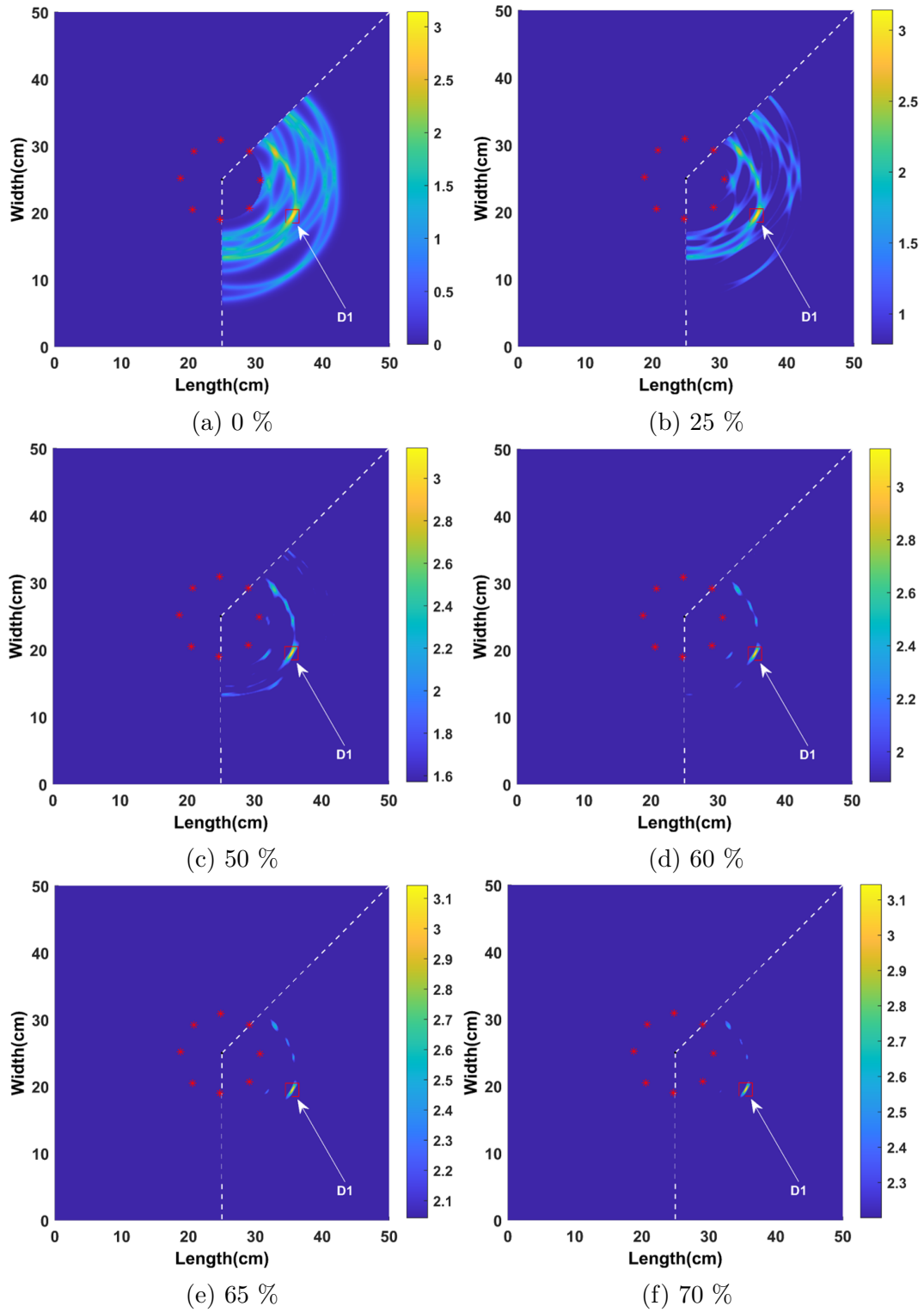


Figure 6.11: Case 8 of Figure 6.10 damage map at different percentages (thresholds).

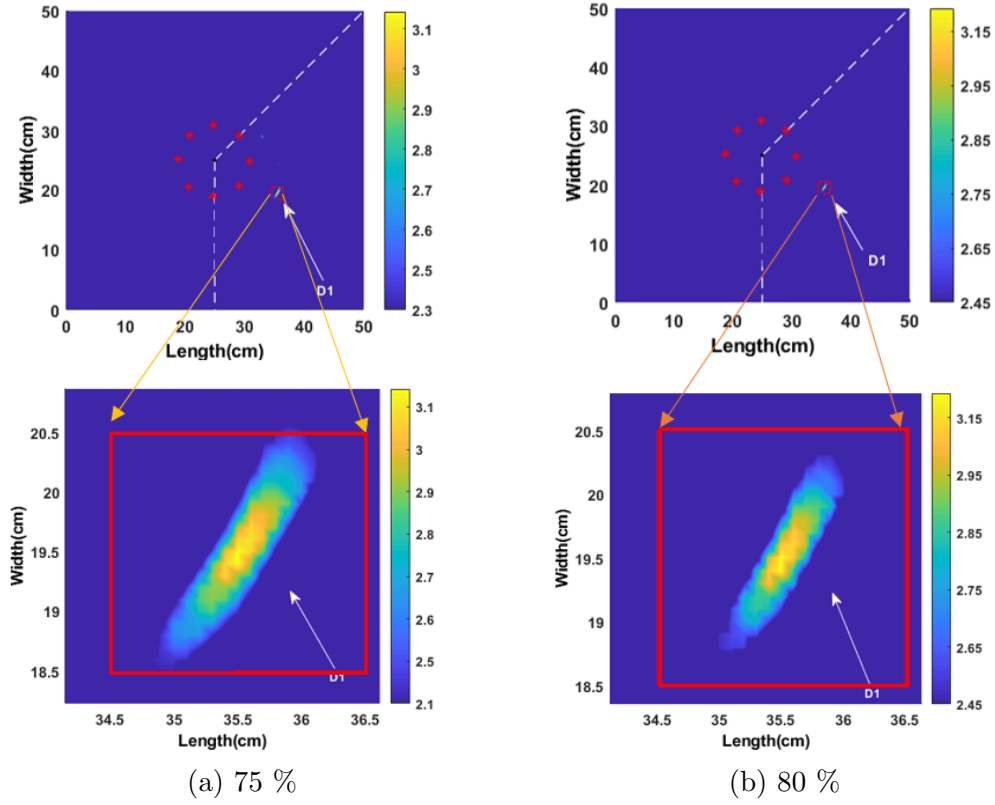


Figure 6.12: Zoomed Case 8 of Figure 6.10 damage map at different percentages (thresholds).

Figure	$D_D$ Pixels	Total Debond SEC pixels	$D_E$ Pixels	Miss hits Estimation	TPI (%)
(a)-0%	400	-	-	-	-
(b)-25%	400	-	-	-	-
(c)-50%	400	-	-	-	-
(d)-60%	400	202	109	93	27.25
(e)-65%	400	145	106	39	26.5
(f)-70%	400	132	104	28	26
(g)-75%	400	106	103	3	25.75
(h)-80%	400	85	85	0	21.25

Table 6.8: Pixel count-based error estimation.

culation time and grid numbers using sector-wise SEC. The benefit of using the damage detection step (RMSD maps) is that it allows for a quick dam-



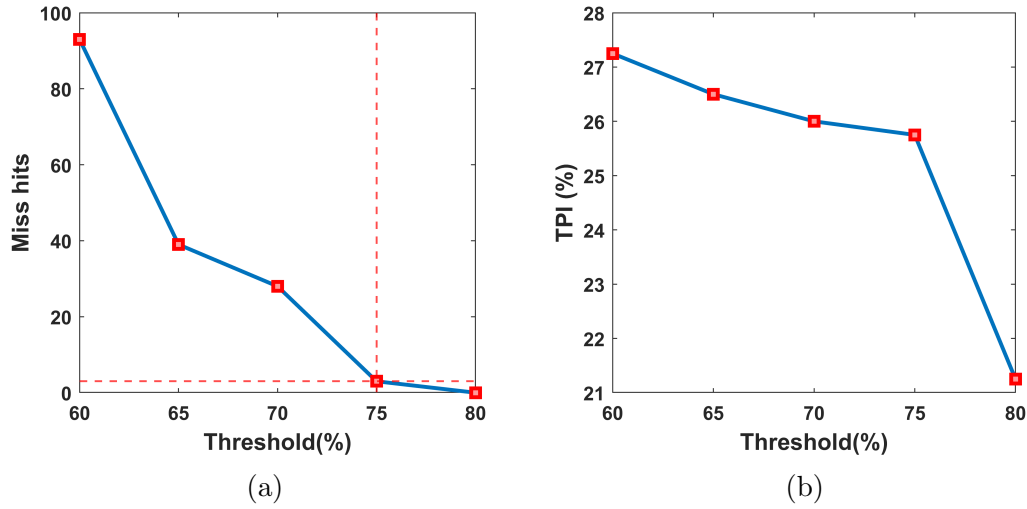


Figure 6.13: Threshold (vs): (a) Miss hits, (b) TPI.

age check without executing velocity estimation. It is noticed that the RMSD matrix map values near damages are higher when compared to the cases away from the damage. The detection step helps avoid higher false-negative results in the damage localization step. The damage detection step helped identify the damages (debonding, magnets) using both inner and outer monitoring approaches. Sectors (angular, circular) were created based on the detection step results later in the SEC localization step.

The SEC-based SHM strategy has proven its potential to localize multiple debonding with different sizes along with multiple randomly placed mass locations in the SCS. Numerical models were also developed to validate the experimental modes using the proposed multi-step strategy. The SEC process localized the damages with an error estimation value of roughly 0.8 cm and cut the calculation time to 52%, and grid numbers to 97%. The SHM results were then cross-verified using the NDT methods. The overall benefits of the proposed SHM approach are total time reduction and fewer computations in SEC analysis due to quick sector analysis of the RMSD-based damage detection step. The quantification using TPI helped to quantify the damages and to arrive at a proven threshold value.

## 6.2 CFRPS: multiple impact damage identification using LDV scanning points

Many GW studies have been conducted on thin CFRPS [46], [48], [114] to identify the damages. It is difficult to quantify the damage severity of an

impact crack damage (ICD) using only GW methods. Thus, NDT methods such as ultrasound C scan (shows contour image) may be used in such instances [48]. This section aims to study several ICDs on thick CFRPS using the proposed common multi-step method. The ICDs were created by dropping a steel ball with impact forces of 24 and 31J respectively. Wave propagation was investigated using a single PZT sensor to detect and localize various-sized ICDs in a multi-layer CFRPS. The GW A0 mode was utilized to detect the damage. The experimental data were quantified using FWF and RMS. SEC aids in the rapid localization of ICDs by utilizing a small number of sensing points (14 points) and reducing overall calculation time. The method works by applying the improved elliptical algorithm to the sectors calculated from the RMSD of the signal data. After performing a directional dependency RMSD test on the signals, the sectorial RMSD calculations were considered. This test is necessary to demonstrate that the value is constant for the direct time of wave arrival and varies for the entire signal.

### 6.2.1 Details about experimental setup, CFRPS and damages

The study employs a multi-layered CFRPS panel with dimensions of  $20 \times 50 \times 0.5 \text{ cm}^3$  with a 16-ply orthotropic structure of layup sequence  $[0/90]_{4s}$ . Table 6.9 displays the material properties that were used. As shown in Figure 6.14(a), the PZT is attached in the centre ( $10 \text{ cm} \times 25 \text{ cm}$ ). The impactor steel ball ( $1.1 \text{ cm}$  dia) was glued to two steel bars (impactor setup) and dropped from various heights on CFRPS by placing them in a pipe that guided the impactor. The impactor caused two impact damages: ICD1 with a 31 J impact (centre coordinates  $10 \text{ cm} \times 8 \text{ cm}$  and diameter  $2.4 \text{ cm}$ ), ICD2 with a 24 J impact (centre coordinates  $10 \text{ cm} \times 38.5 \text{ cm}$  and diameter  $1.2 \text{ cm}$ ), and internal cracks in the CFRPS. Figure 6.14b shows a two-dimensional schematic representation of CFRPS with circular (refer to section 3.1 and Figure 3.4a) scanning points for SEC analysis.

Material	$\rho$ (kg/m3)	$\nu_{12}$	$\nu_{23}$	$E_{11}$ (GPa)	$E_{22}$ (GPa)	$E_{33}$ (GPa)
Carbon fiber	1900	0.2	0.2	275.6	27.5	27.5
Epoxy matrix	1300	0.35	0.35	3.43	3.43	3.43

Table 6.9: Material properties of CFRPS.

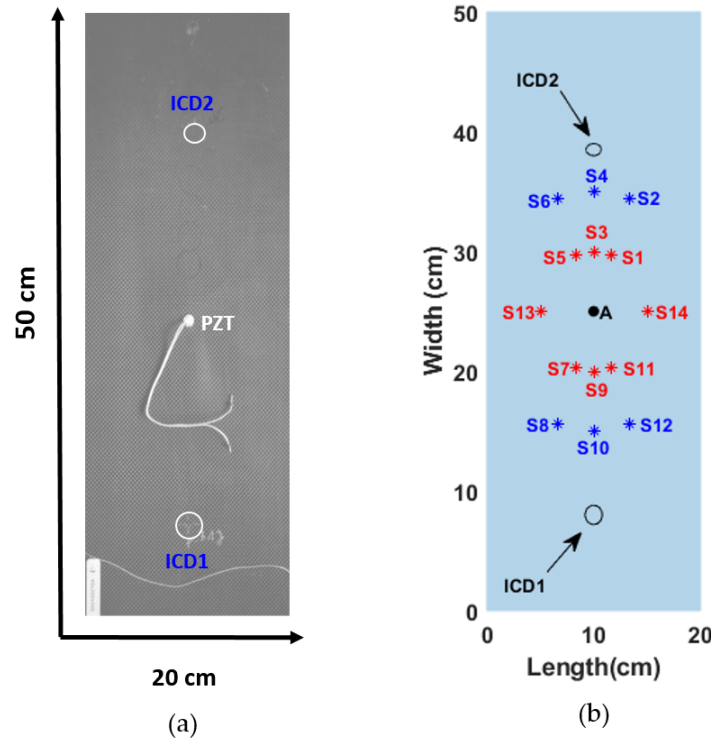


Figure 6.14: Damaged:(a) CFRPS, (b) Sensing points for SEC study.

### 6.2.2 Initial discussion

The multi-step methodological process shown in Figure 6.1 was utilized in this case too. This section combines GW analysis with the signal processing method (RMS) and the visualization of the ICD with FWF results. The choice of the frequency and mode and the FWF analysis of the structure is shown in Appendix A.3. The tests were expanded further to include an SEC-based study in determining ICD locations. To test the effectiveness of the proposed SEC, two cases from LDV (Case 1) and data from SEM were examined (only for validation purposes).

### 6.2.3 Damage localization results and discussions

This section discusses the results of the SEC method (described in section 4.1), and the damage estimation is based on the scanning point selection. The sensing /scanning points S1-S14 used in this study are 5 cm apart and equally spaced. For this SEC study, circular point arrangement, as shown in Figure 6.14(b).

### 6.2.3.1 RMSD analysis of signals: Step 1

The RMSD of the signals from healthy and damaged scanning points was calculated. At first, only the inner perimeter scanning points with a close radius to the actuator (A) were considered (shown in red in Figure 6.14c)). The RMSD is calculated only up to the first wave arrival to test GW's directional dependency (as mentioned in subsection 6.1.1). This is based on an assumption that there is no damage in the inner part of the sensing array. It is done to remove the influence of GW reflection caused by the boundaries and ICDs. The obtained RMSD values are roughly equal and allow for comparison of different wave propagation directions. Figure 6.15 shows how it is analyzed for both LDV and SEM data obtained only to check for validation purposes).

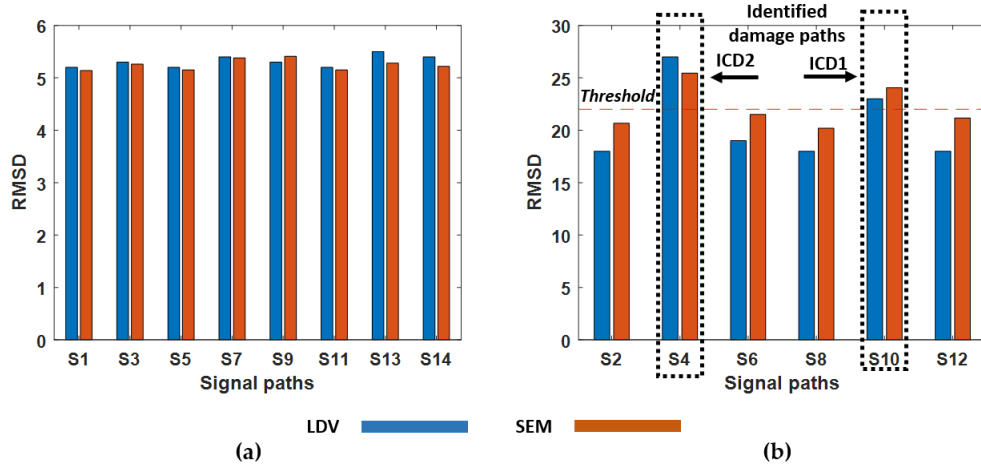


Figure 6.15: RMSD maps : (a) First wave arrival, (b) Entire signal length.

After confirming the waves' directional dependency, the RMSD is applied to the entire length of the signals (refer to Figure 6.1). The outer perimeter scanning points of a larger radius to the actuator were taken into account (shown in blue in Figure 6.14c). As shown in Figure 6.15b, the RMSD values obtained showed higher variations above the threshold value near the ICDs for both LDV and SEM data. An average threshold value of 22 was set (obtained from S2, S6, S8, and S12-RMSD values from healthy sensing points), and signal path values above the threshold are only considered for further investigation. Figure 6.15 (a,b) for both the data revealed that the RMSD variation is greater between points S4, and S10, and the value remains more or less constant for other points. The identified damaged ICD paths are then used to determine the sectors for use with the SEC method. The sectors are plotted with a precision of  $45^\circ$ , determined by the sensor's angular separation. This RMSD-

based study identified sensor points S4, and S10 as damage paths and sector borders were defined.

### 6.2.3.2 SEC models and results: Step 2

The velocity values obtained from the LDV, SEM, and LAMSS tools (obtained from University of South Carolina -<http://www.me.sc.edu/Research/lamss/>) are shown in Table 6.10. At  $90^\circ$ , the values are found to be in general agreement. The variation in the  $0^\circ$  value could be due to the nature of GW modes or changes in the density values considered by the LAMSS tool and SEM. Fitting the velocity values to an elliptical function yields the velocity profile as shown in (Figure A.3).

Method	Layer orientation $0^\circ$	Layer orientation $90^\circ$
LDV	2289	1868
SEM	2140	1724
LAMSS	1890	1689

Table 6.10: Predicted group velocity values.

The SEC sectorial map obtained for experimental case 1 is shown in Figure 6.16(a). The A and B portions denote neglected areas. This is done after taking into account the sector-specific segregated regions based on RMSD path analysis (subsection 6.2.3.1). The calculation time is reduced in this manner. The analysis is also performed on numerical SEM data (case 2: Figure 6.15b) and results obtained in Figure 6.16(b). The higher energy elliptical intersection region, which is closer to the ICD locations, is denoted by black circles. Tables 6.11 and 6.12 show error estimation, time, and grid point reduction (pixel numbers mentioned as nos) with and without SEC, respectively.

Case	Damage coords ICD1, ICD2	Estimated coords ICD1, ICD2	$\delta P$ ICD1, ICD2
Case 1	(10,8), (10,38.5)	(8.85,7.625), (8.5,39.62)	(1.50, 1.80)
Case 2	(10,8), (10,38.5)	(9.1,7.7), (9,39)	(0.96, 1.11)

Table 6.11: Error estimation using SEC [all units in cm].

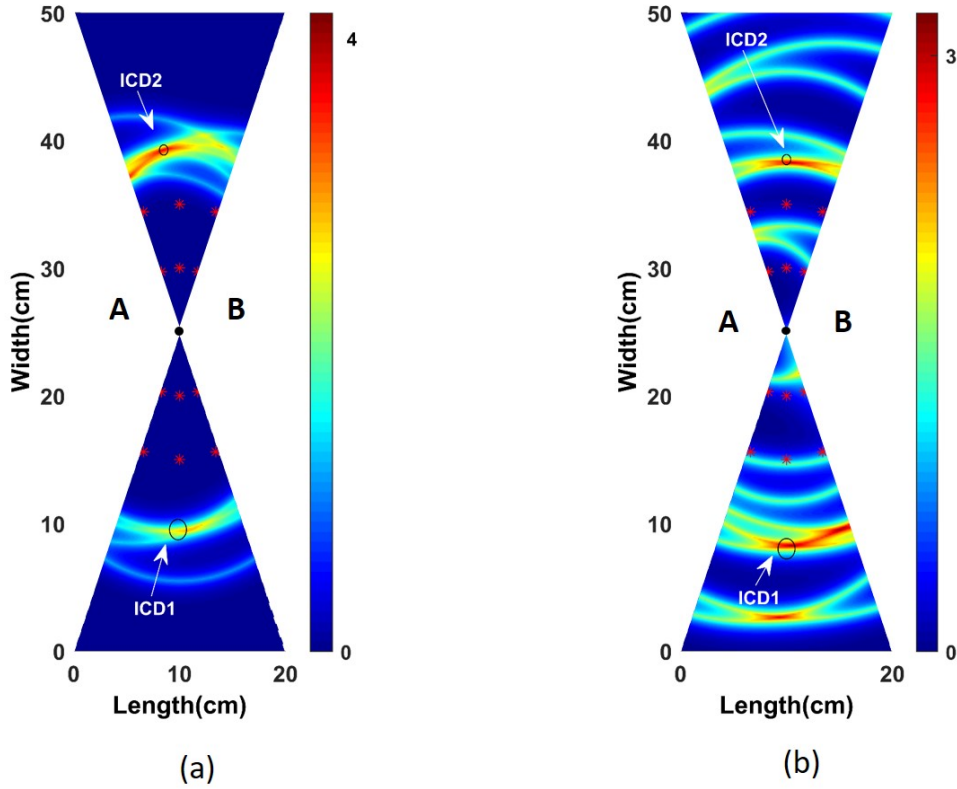


Figure 6.16: SEC localization results (a) Case 1: LDV case 1 (b) Case 2: SEM case 2.

Case	Time, grid points without SEC	Time, grid points with SEC	Reduction in Time, points
Case 1	(12 mins, 160801 nos)	(9 mins, 80400 nos)	(28%), (50%)
Case 2	(14 mins, 160801 nos)	(10 mins, 80400 nos)	(33%), (50%)

Table 6.12: Time and grid reduction percentage with and without SEC.

#### 6.2.4 Sectional conclusion

Multi-layered CFRPS were examined using LDV and a combined global area SHM-GW inspection. The A0 wave mode was used to identify damages, and the RMS map analysis identified visible ICDs at 200 kHz. Based on differences between signal damage paths (S4, S10), RMSD studies identified the ICDs using a directional dependency test. The improved SEC reduced SHM calculation time by 50% and localized ICDs with an error estimation value of 0.96 cm using only 14 scanning points.

### 6.3 ALS: multiple damage identification using FBG sensors

PZTs are widely used due to their low cost and versatility, but they are susceptible to electromagnetic fields and generate high noise, which can affect TOF determination in GW analysis [115]. To mitigate these effects, optical FBG sensors have been studied as they are less sensitive to electromagnetic interference and can be easily attached or embedded in structures [102]. A hybrid PZT-FBG has been explored for ALS analysis due to its ability to produce signals with less cross-talk and a higher sampling rate, such a strategy has become increasingly popular in recent years. The researchers used FBG to localize damages based on the TOF of GW modes [116]. The signals generated at various frequencies are first checked in this study using an improved CD formulation (Equation 3.1). Six simulated damage scenarios were used to test the change in the distance formulation. The damage sectors were identified based on the CD sector-wise area and then the SEC method is used to localize the multiple damages effectively.

#### 6.3.1 Details about ALS and damages

In the research work, a  $50 \text{ cm} \times 50 \text{ cm} \times 0.1 \text{ cm}$  ALS is used to conduct the GW study. By placing magnets of about 1.8 cm in diameter and 12 g in weight at different locations, a total of 6 damage scenarios were simulated. The experimental setup used for the SHM analysis is shown in Figure 6.17 and the explanation of the process of this experiment is described in Figure 2.15 and also in subsection 2.3.3. Figure 6.18 shows a schematic representation of ALS with the damage scenarios mentioned above. A rectangular rubber sheet of  $2.5 \text{ cm length} \times 2 \text{ cm width}$  is also attached to the magnets on both sides to obtain extra sensitivity of the GW signals (shown in Figure 6.19). A frequency range of 50 to 250 kHz (in steps of 50 kHz) was investigated. The methodology used in this scenario is similar to the previous methodology as shown in Figure 6.1. Except for the changes in the methodology where FBG acts as a sensor (refer to Figure 3.4b), the methodology remains the same.

#### 6.3.2 Results and discussion

Signals from the PZT actuator-FBG sensor network are validated by plotting healthy and damaged signals for all frequencies obtained. Figure 6.20 shows an example of healthy and damaged signals from actuators (PZT) 3, 6 at 150 kHz, demonstrating signal variation. The varying amplitude of the damage signal is then used to calculate the varying CD between them (Figure 6.21).





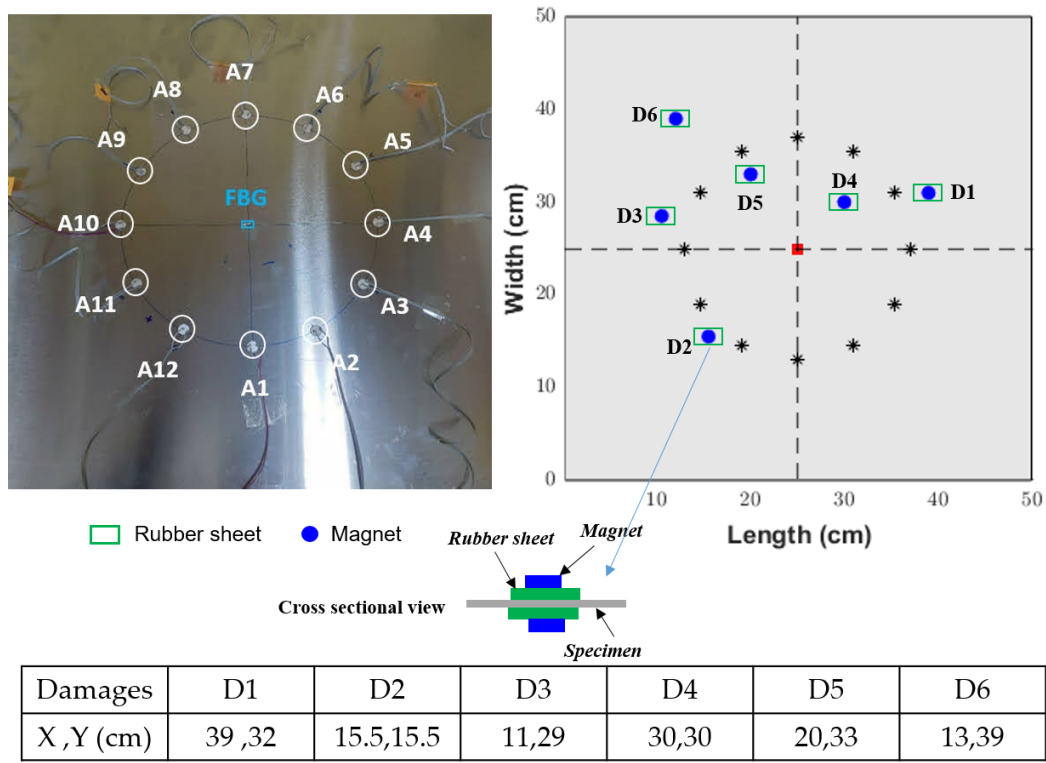


Figure 6.18: Schematic representation of the ALS and damage locations.

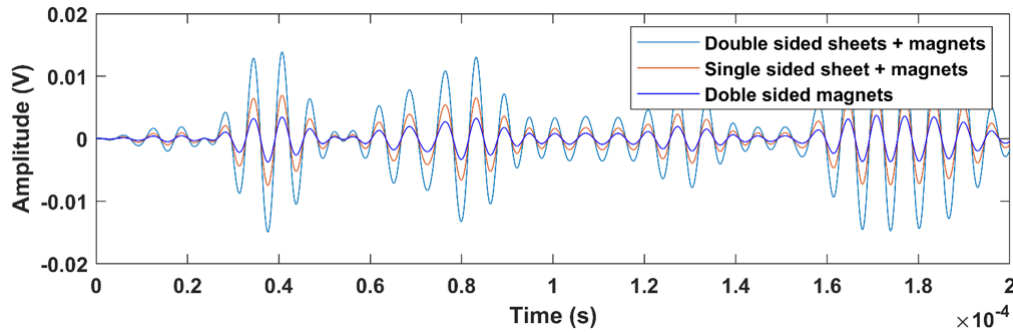


Figure 6.19: GW signals sensitivity with added rubber sheets.

identified using CD studies and as a result, a sector region was created. The analysis is performed for damages (in the form of magnets with rubber sheets) located at various locations. The location of damage using the SEC algorithm is calculated in the predicted sector zone to detect damage. Using an FBG-PZT coupled network strategy, a combined identification and localization approach is presented to localize the damages.

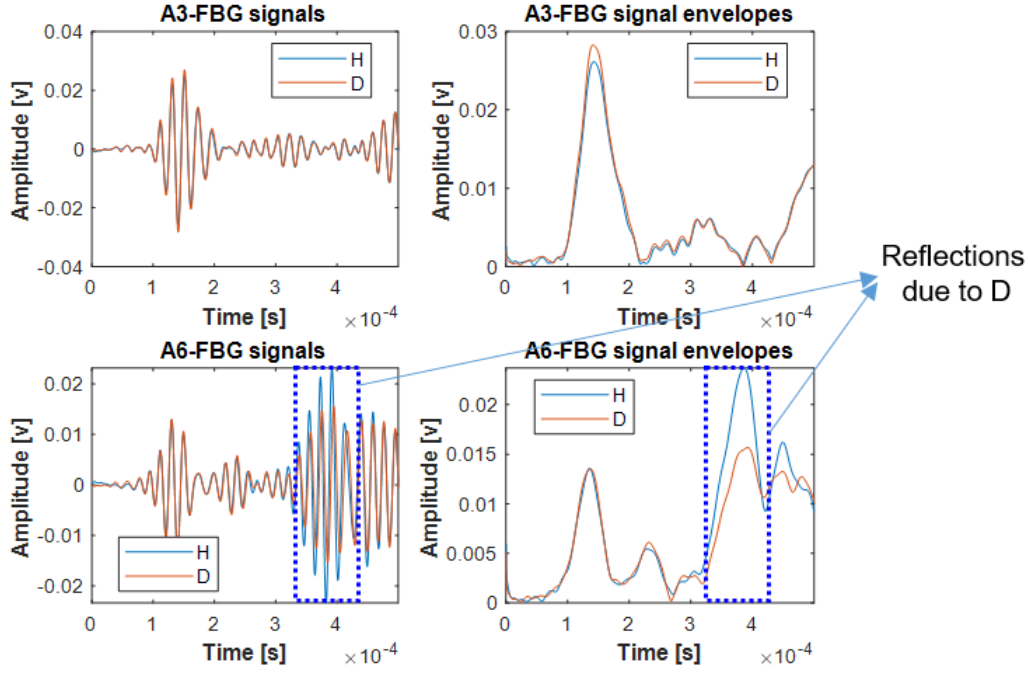


Figure 6.20: Exemplary signal difference between Healthy and Damage D1.

D states	Damage coords (cm)	Estimated coords (cm)	$\delta P$ (cm)
D1	(39,32)	(37,33)	2.2
D2	(15.5,15.5)	(15.2,14.8)	0.7
D3	(11,28)	(12.1,29)	1.4
D4	(30,30)	(30.6,29.5)	0.7
D5	(20,33)	(20,31)	2
D6	(13,39)	(12.9,38.2)	0.8

Table 6.13: Damage estimation analysis predicted with SEC.

#### 6.4 ALS-FEM: multiple damage identification using FEM models

In this section, numerical GW simulation with a PZT-FBG hybrid coupling process is used to analyze an ALS with the help of Abaqus FEM software. The damages are caused by making changes to the stiffness matrix (60 % reduction) in a few small regions of the ALS. Due to its ability/sensitivity to detect smaller damages, the GW A0 mode is chosen as the optimal GW mode for damage imaging, as shown in [101]. The theoretical values of the dispersion

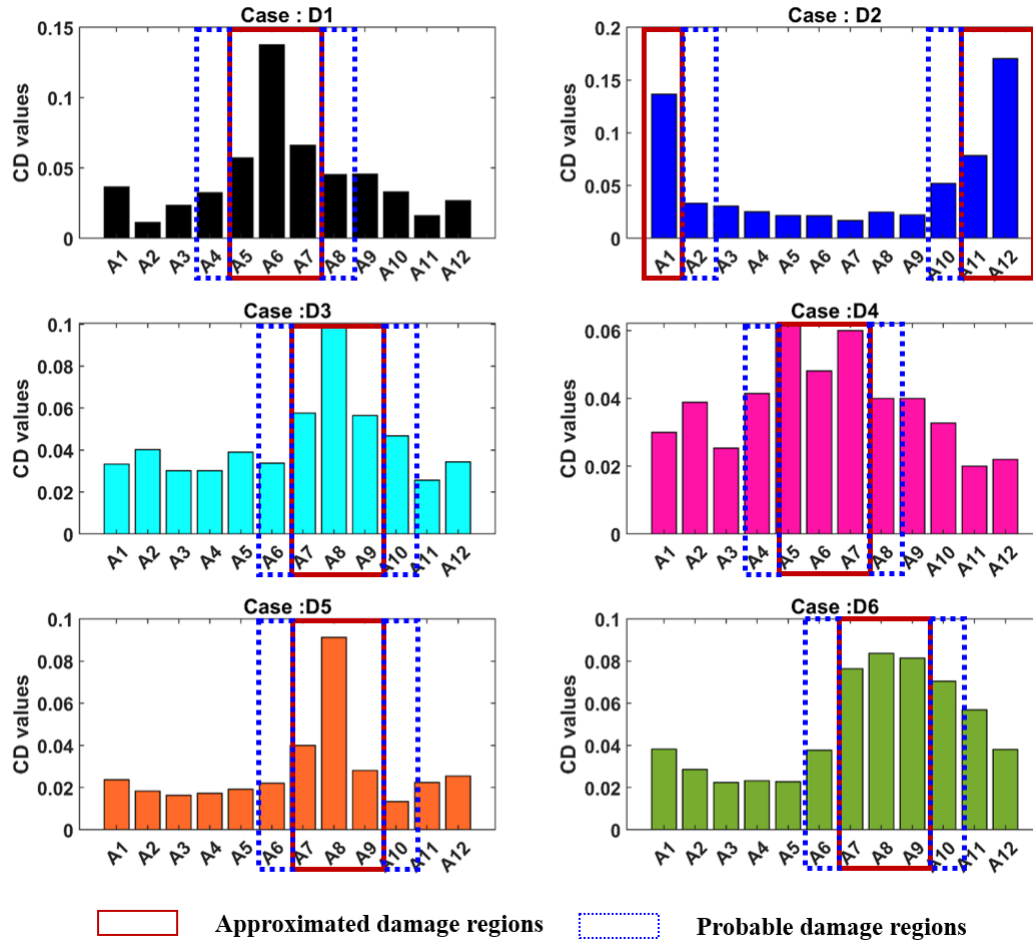


Figure 6.21: CD bars sectorial regions: experimental damage cases.

D states	Time, grid points without SEC	Time, grid points with SEC
D1	(14.5 mins, 251001 nos)	(6.8 mins, 42639 nos)
D2	(13 mins, 251001 nos)	(7.7 mins, 42639 nos)
D3	(15 mins, 251001 nos)	(9.3 mins, 42639 nos)
D4	(12.8 mins, 251001 nos)	(6.7 mins, 42639 nos)
D5	(16.2 mins, 251001 nos)	(7.4 mins, 42639 nos)
D6	(15.8 mins, 251001 nos)	5.8 mins, 42639 nos)

Table 6.14: Time and grid point difference with and without SEC.

curve are cross-checked with the numerical A0 velocity results obtained from the FBG-PZT model. The obtained results showed a good agreement of the

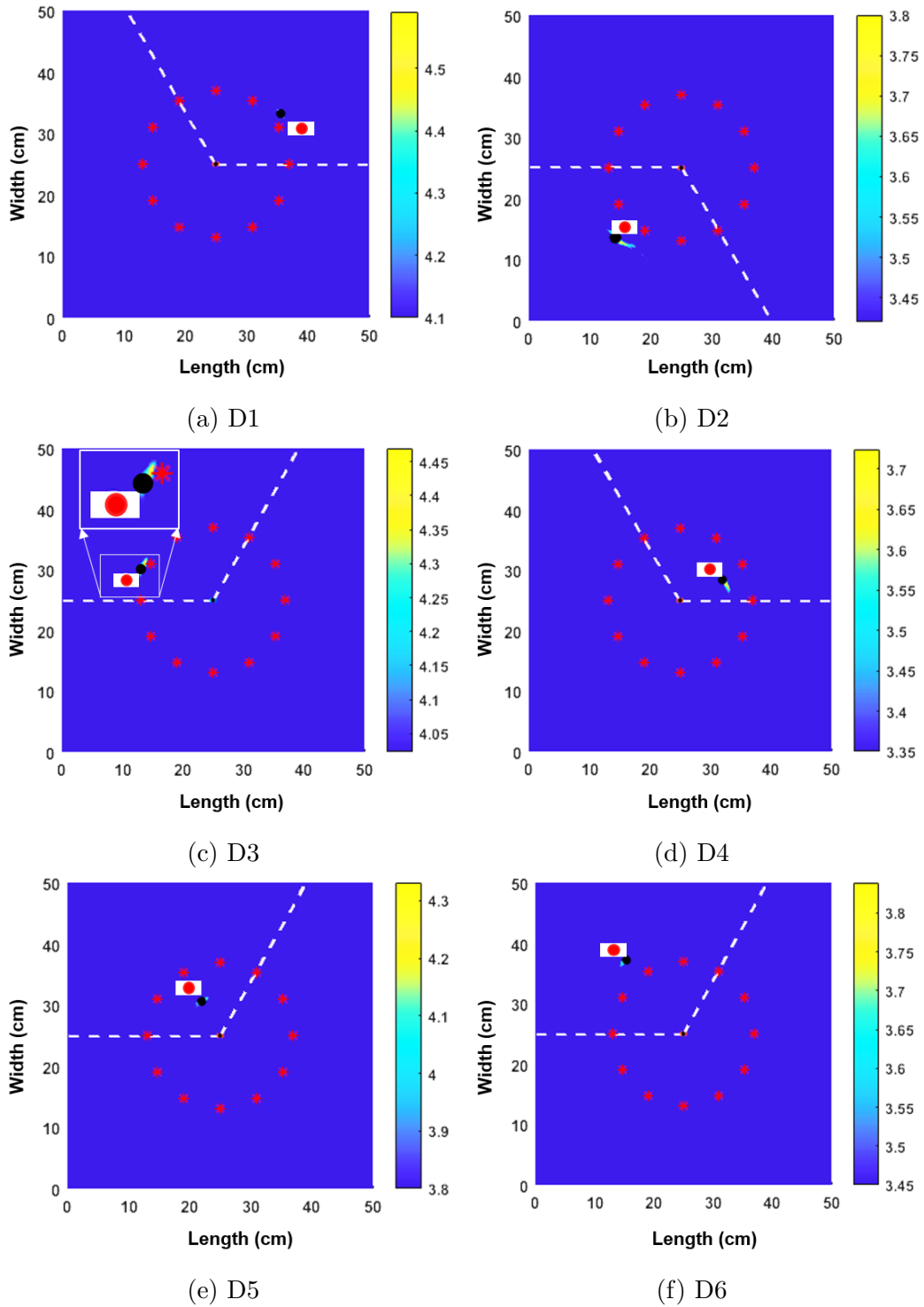


Figure 6.22: Localized SEC results of different damage scenarios.

velocity values (shown in Appendix Table A.3), indicating that the numerical simulation matches the laboratory experiments on similar ALS. The main advancement in this section is to showcase a GUI tool to convert numerical strains

to GW signals (shown in Appendix A.6) Matlab-FEM-based process (shown in Appendix A.5) to simulate the FBG PZT coupling mechanism to detect GW, which reduces overall run time, and a CD-based formulation (Equation 3.1) to identify the damaged region.

#### 6.4.1 FEM model preparation

Using the FEM Abaqus solver, a 3D numerical model was created and simulated using a dynamic explicit scheme. FEM-assisted GW studies were found to be time-consuming as a small mesh size is required to capture short wavelength [118]. FEM models for the healthy and damaged stages were created (Figure 6.23), meshed, and simulated in the Abaqus environment. The FEM model has the FBG sensor (linear row of elements of about 1 cm length) in the centre as shown in Figure 6.24a,b and 12 PZT actuators (made of cylindrical coordinate points) arranged in a circle to excite the waves circularly as shown in Figure 6.24 c. In meshing the model, a 3D C3D8R orthotropic brick element (3D hexagon) was used. Six damage scenarios were simulated at various locations to investigate the impact of GW. The GW signals change depending on where the PZTs and damages are located (location, size, length, etc.). Later in the study, the FEM model is linked to the Matlab script (Pseudocode in Appendix A.5) to automatically run the entire simulation process of frequency changes, damage creation, and data storage without any human intervention.

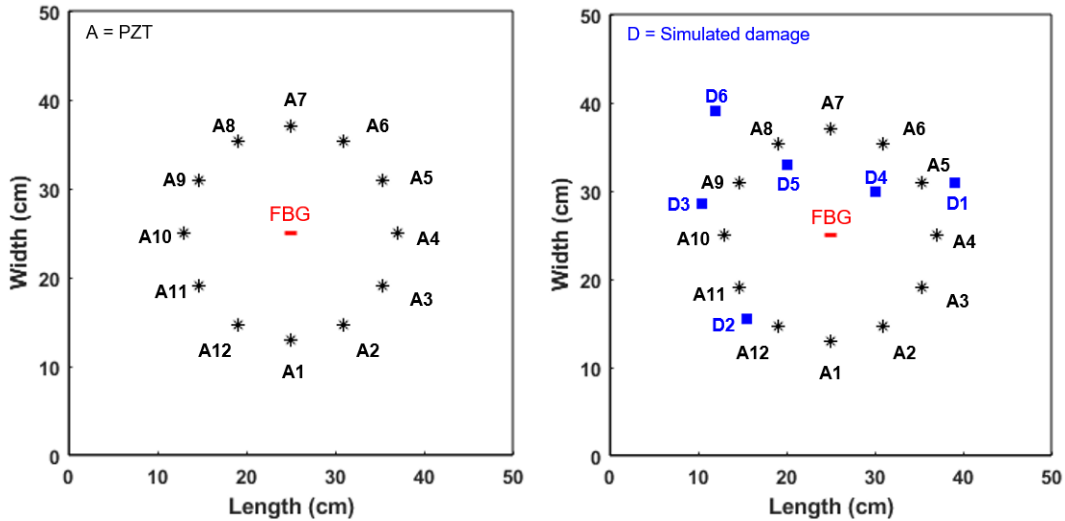


Figure 6.23: ALS: (a) Pristine, (b) with multiple simulated damages.

### 6.4.2 Dynamic explicit procedure

In this numerical setup, an excitation input is a 5-cycle sine modulated Hanning windowed frequency. To capture even the shortest wavelengths, a desired maximum elemental size ( $L_M$ ) is necessary. In this study, the  $L_M$  test was verified using the wavelength equation [5] (phase velocity of the specific mode / maximum frequency used), which produced a result of 9.8 mm (theoretical phase velocity  $V_{cpA0}$  Th 2458 m/s obtained from 250 kHz). In this FEM simulation, three elements per thickness are used and 0.05 mm is chosen as  $L_M$  (a value less than the calculated value). The numerical model was even checked with five elements per thickness which gave similar results (grid-independent study). The time period used in the experimental calculation [101] was determined to be 600  $\mu$ s, and this is also used in the numerical calculation.

### 6.4.3 FBG PZT hybrid coupled model

To understand wave propagation, interactions, and reflections, the FEM simulation waveform plots and wave fields are synchronized (shown in Appendix A.5.1). The use of 2D mesh, SEM can reduce the computation time largely. But, the idea to generate a 3D mesh is to replicate the actual 3D aluminium structure and to use Matlab-assisted pseudocode in Appendix A.5. Three million solid C3D8R (orthotropic 8 nodal 3D hexagonal elements) with the smallest mesh size of 0.05 mm are used to model the entire 3D model (Table 6.15 and Figure 6.24a). The dynamic explicit modelling is run with a fixed time step of 600  $\mu$ s. Applying displacement/rotation constraints to the location by selecting the edges, and an additional rotation constraint is applied to a corner point to prevent the FEM plate model from moving, are the boundary conditions. By selecting eight circular nodes to effectively excite the GW in all directions (Figure 6.24b), a cylindrical global coordinate system is created, which is much superior to a single point force-concentrated load [5]. The input displacement (amplitude vs time) obtained from the Matlab code is used to excite the waves for the frequencies used.

ALS FEM model	Element	Element number	Nodal number
3D solid	C3D8R	3E6	9/element

Table 6.15: FEM model parameters.

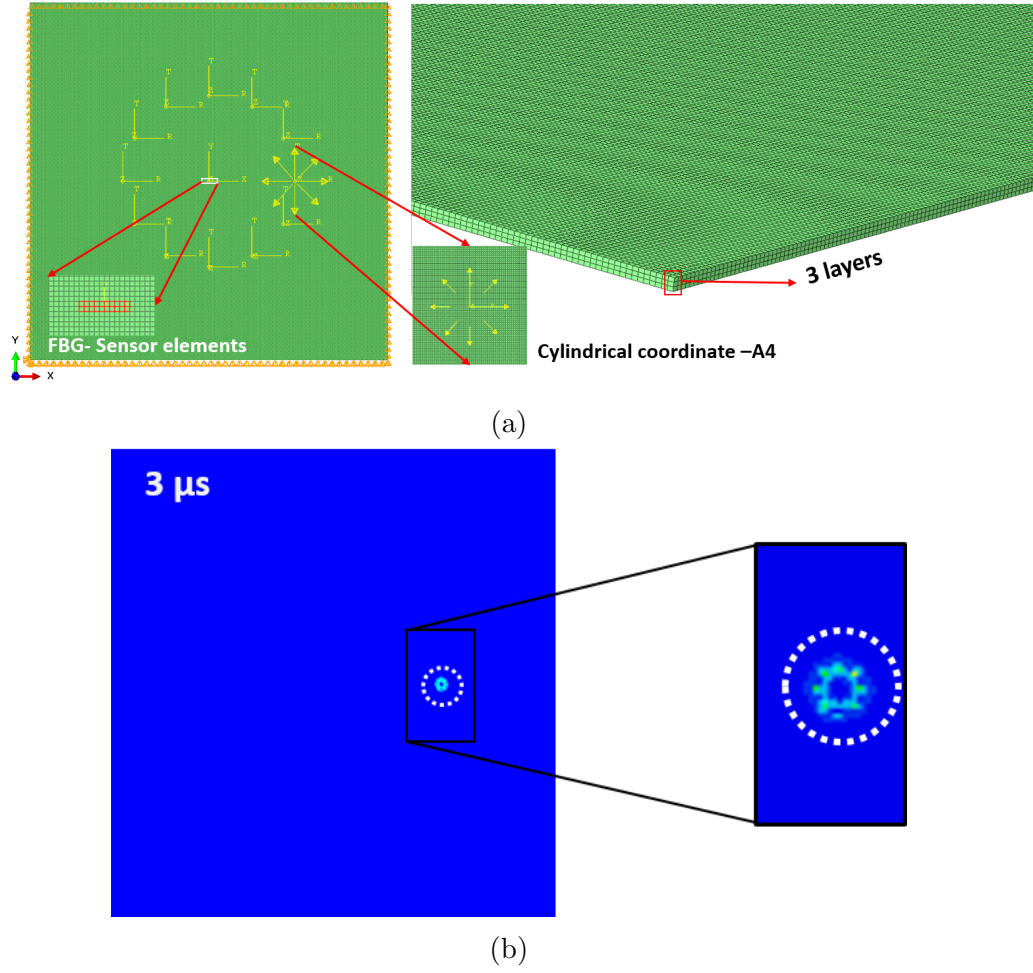


Figure 6.24: FEM (a) Meshed model, (b) Excitation from the cylindrical coordinate nodes.

#### 6.4.4 Theoretical equations

To compute the FBG spectrum for the transfer matrix approximation, the displacements of the numerical model derived from the FBG-PZT model were translated into strain. The theoretical equations show the equations involved in the spectrum modelling, which are then modelled into a GUI as shown in Appendix A.4. FBG Equation 6.2 represents Bragg's condition for a state without strain. The following equations are used in the reflectivity spectrum modelling.

$$\lambda_B = 2n_r\Lambda_0 \quad (6.2)$$

Where: centered wavelength is  $\lambda_B$ ,  $n_r$  is the effective refractive index (mean),

nominal period of the refractive index modulation is  $\Lambda_0$  (constant).

The  $\lambda_B$  is derived from first-order differential equations obtained along the GW prorogation direction and is related to the theory of the coupled mode [119]. The self-coupling coefficient ( $\Delta\beta$ ) is defined as a function of wavelength ( $\lambda$ ) and coupling coefficient ( $\kappa$ ) between the GW modes (Equations 6.3, 6.4).

$$\Delta\beta = 2\pi n_r \left( \frac{1}{\lambda} - \frac{1}{\lambda_B} \right) \quad (6.3)$$

$$\kappa = \frac{\pi}{\lambda} m \delta n_r \quad (6.4)$$

Where:  $\delta n_r$  is the mean change in the induced refractive index and is 6E-5 [13],  $m$  is the fringe visibility of the FBG and is close to a constant value of 1. The transfer matrix ( $T$ ) is calculated (Equation 6.5) using the coupled mode theory as follows:

$$T = \begin{bmatrix} S_{11} & S_{12} \\ S_{21} & S_{22} \end{bmatrix} \quad (6.5)$$

$S_{11}$ ,  $S_{12}$ ,  $S_{21}$ , and  $S_{22}$  are the wave outputs in both the positive and negative axes. The grating's reflectance ( $R$ ) is obtained as in [120], with less computational time results. The theoretical reflectivity spectrum (Figure 6.25) is plotted using the  $R$  (vs)  $\lambda$  values obtained. The Equations 6.6, 6.7 are repeated for each value of  $\lambda$  and  $x$  (length along FBG).

$$R = \left| \frac{S_{21}}{S_{22}} \right|^2 \quad (6.6)$$

$$\begin{aligned} \delta_x &= L/n \\ \Upsilon_B &= \sqrt{\kappa^2 - \Omega^2} \\ S_{11} &= e^{-i\Delta\beta\delta_x} \\ S_{12} &= ik\delta_x \sin((\Delta\beta\delta_x) \cdot / (\Delta\beta\delta_x)) \\ S_{21} &= -ik\delta_x \sin((\Delta\beta\delta_x) \cdot / (\Delta\beta\delta_x)) \\ S_{22} &= e^{i\Delta\beta\delta_x} \end{aligned} \quad (6.7)$$



Where:  $\delta_x$  is the length of the segment,  $L$  is the FBG length,  $n$  = short segments of  $L$ ,  $\Omega$  is the self-coupling coefficient.

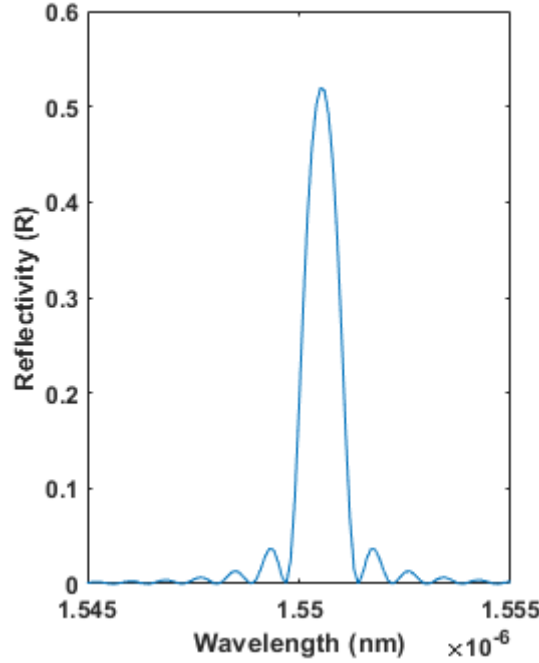


Figure 6.25: Theoretical reflectivity spectrum.

#### 6.4.5 CD similarity analysis: Step 1

Due to the FBG sensor's directional sensitivity [121], techniques like RMS, and RMSD are very difficult to implement. This subsection employs the CD method for damage identification due to its independence of amplitude or scaling. To distinguish between healthy and damaged paths in a group of signals, the previously mentioned CD formulation (Equation 3.1) is used. The CD formulation is used to investigate all possible actuator sensor pair signals in order to localize the damaged regions. The signals produced with the numerical simulations are displacement-based signals, and for the FBG measurements, strain-based signals are required.

To counteract this, a GUI was created as elaborately shown in Appendix A.6 to input the numerical signals, check the reflectivity spectrum and obtain the strain signals. The section A.6 is also shown with 2D model results. The signals from the PZT-FBG model network (obtained after GUI output) are validated by plotting healthy and damaged signals for all excited PZT networks. The difference in CD between them is then calculated by using the

varying amplitude of the damage signal. The CD change is then mapped to the location of the damage (D1-D6), and the probable region of the damage (red rectangle) is assumed, as shown in Figure 6.26.

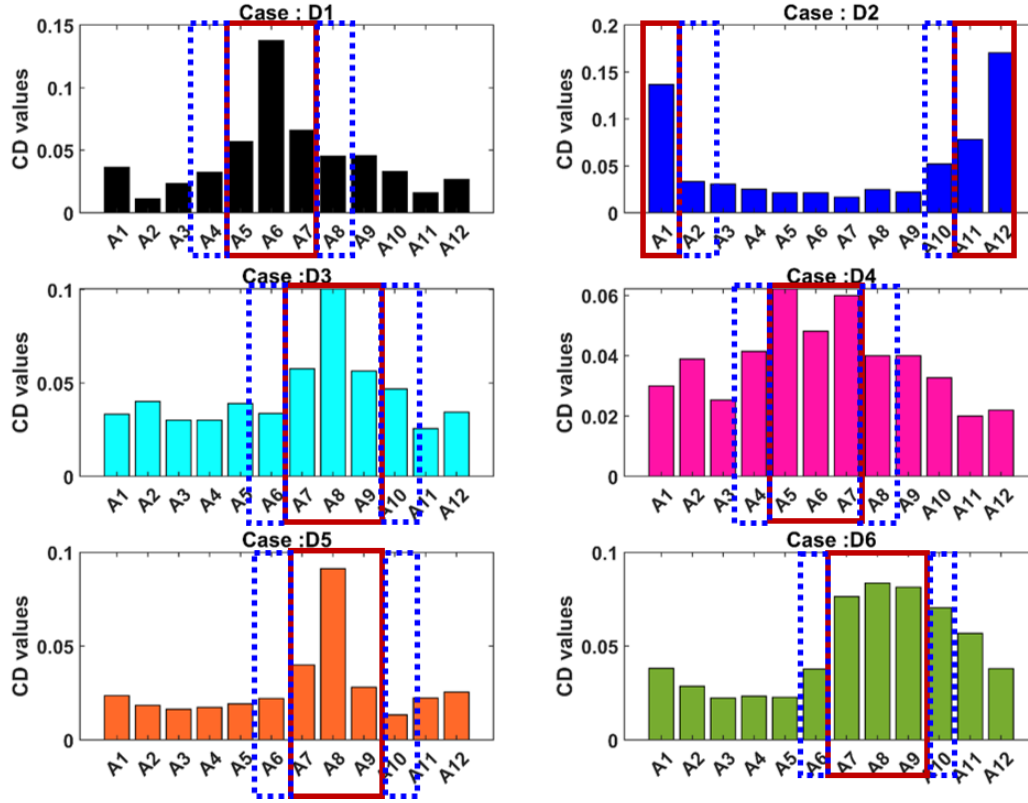


Figure 6.26: CD bars sectorial regions: numerical damage cases.

#### 6.4.6 SEC localization analysis of FEM models: Step 2

The results for all six damage scenarios are shown in Figure 6.27. To locate the hotspots, a threshold value of 75% is used in the form of min and max values (based on the threshold approximation shown in [25]). SEC calculation with the FEM models was quick as the signals obtained were with less noise, and thus filtering was not required. The error estimated values (in cm) obtained for the SEC localization are shown in Table 6.16, along with the original coordinates and the error estimate. The total time taken for the SEC calculation to run was 7.8 minutes (approximately) against the general elliptical function which when compared took 15 minutes (as shown in Table 6.17).

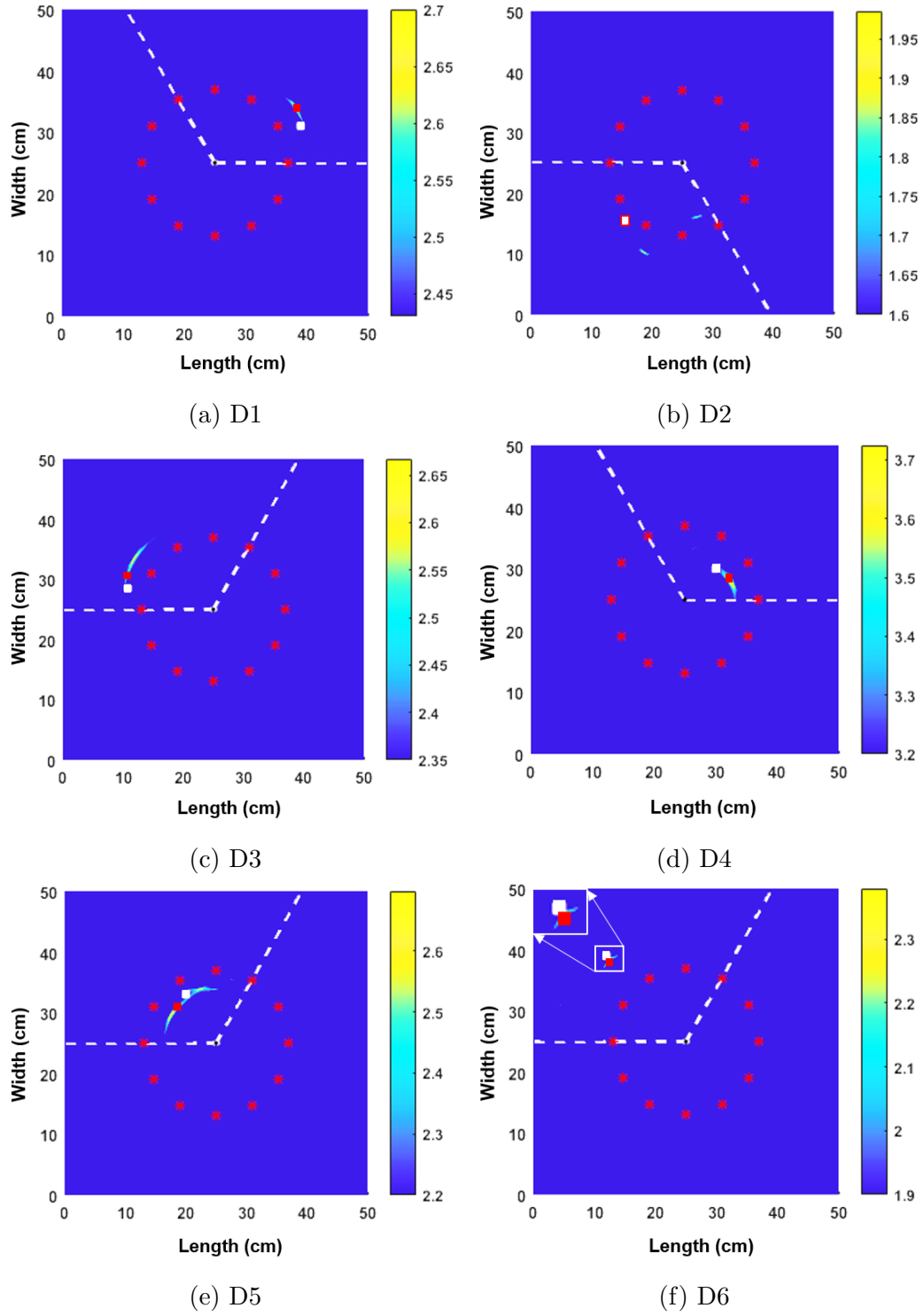


Figure 6.27: Localized FEM SEC results of different damage scenarios.

<b>D states</b>	<b>Damage coords (cm)</b>	<b>Estimated coords (cm)</b>	<b><math>\delta P(\text{cm})</math></b>
D1	(39,32)	(39,33.1)	1.1
D2	(15.5,15.5)	(15.5,15.4)	0.1
D3	(11,28)	(11,29)	1
D4	(30,30)	(32,28.8)	2.3
D5	(20,33)	(20.5,30.4)	1.5
D6	(13,39)	(12.9,38.5)	0.5

Table 6.16: Damage estimation analysis predicted with SEC.

<b>D states</b>	<b>Time, grid points without SEC</b>	<b>Time, grid points with SEC</b>
D1	(14.5 mins, 251001 nos)	(6.5 mins, 42639 nos)
D2	(13 mins, 251001 nos)	(7.2 mins, 42639 nos)
D3	(15 mins, 251001 nos)	(7.0 mins, 42639 nos)
D4	(12.8 mins, 251001 nos)	(6.8 mins, 42639 nos)
D5	(16.2 mins, 251001 nos)	(5.6 mins, 42639 nos)
D6	(15.8 mins, 251001 nos)	(6.0 mins, 42639 nos)

Table 6.17: Time and grid point reduction with and without SEC.

## 6.5 Sectional Conclusion

The study used the FBG-PZT hybrid technique to localize multiple damages in a numerically modelled ALS. The linking of Abaqus FEM and Matlab aided in the quick simulation of numerous models at various frequencies with less human intervention and computational time. Theoretical and numerical dispersion curve results matched well for the A0 mode. CD-based studies identified the damage region, while SEC-based quadrant analysis was used to locate FEM stiffness reduction areas. The grid was reduced to half of the 251001 calculation points, reducing the time by nearly half.

## Chapter 7

### Effect of GW in FBG direct and remote bonding configurations

#### 7.1 FBG sensor bonding configurations

Direct attachment of the FBG sensor to the structure (direct bonding) is a tried and tested technique in the FBG methods of GW analysis [102]. The results reported in sections 6.3 and 6.4 are for direct bonding arrangements. This direct-bonding configuration results in axial deformation along the length of the FBG. Direct bonding of the FBG sensor to a structure aids in the detection of both forward and backward propagating waves [11], and researchers used this technique in many SHM applications. Researchers proved that the remote bonding type setup, which involves the optical fiber instead of the FBG attaching to the structure, can also identify the GW [13]. The signal amplitude of FBGs remotely attached in structures is greater than that of directly bonded FBGs [102].

The magnitudes of the GW signals are compared in this study by keeping the FBG experimental setup in direct, remote bonding with different actuator connections (PZT based). In this section, the signal amplitudes using a remote bonding setup similar to that shown in [102], [122], but with elongated bonding cases, were studied in detail for the first time. As an improvement to the proposed remote moving bonding configuration, the research compares bonding configurations with different connections. The section serves as experimental evidence to study further direct and remote kinds of bonding using FBG sensors and SHM configurations in future work.

##### 7.1.1 Experimental analysis

The experimental analysis was performed on an isotropic ALS of dimensions 50 cm  $\times$  50 cm  $\times$  0.1 cm. The experimental setup is explained in brief in Figure 2.15 and also in [123]. Two PZTs were attached to the top and bottom

surfaces of the structure in a parallel fashion using cyanoacrylate glue. Three different connection types were made by changing the polarity of the PZTs as shown in Figure 7.1 and also explained in brief in [102]. A 5-cycle continuous sine tone burst is supplied to the PZT via a waveform generator after applying a modulated Hann window to it. A frequency of 50 to 250 kHz (in steps of 50 kHz) was used as the input excitation frequency and is supplied to the glued PZT to excite GW signals.

The FBG (used as a sensor of center wavelength 1550.04 nm) is placed at the center of the structure ( $25\text{ cm} \times 25\text{ cm}$ ) to sense the GW. The FBG was placed in a parallel manner to the PZT as it is sensitive to unidirectional signals and generally senses low electromagnetic noises when compared to PZT as a sensor. In-phase, out-of-phase, and direct PZT arrangements (three connection types) were analyzed on the structure to identify different GW modes as shown in Figure 7.1.

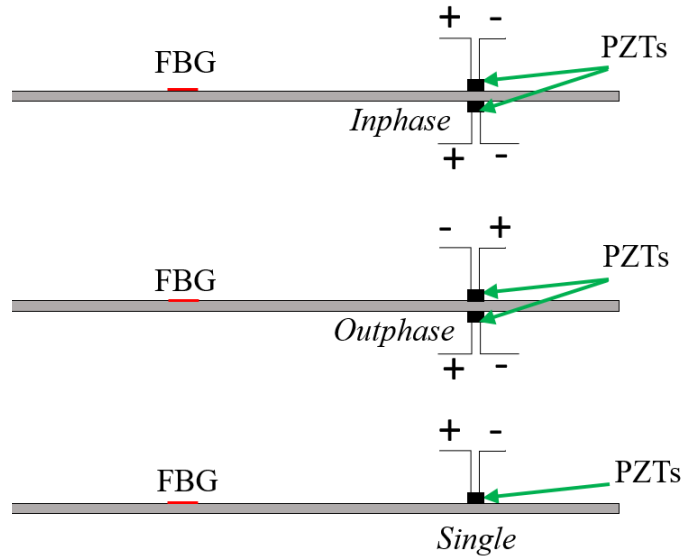


Figure 7.1: Different PZT connection types.

The direct bonding and remote bonding configurations were checked using the mentioned PZT connections in Figure 7.1. The output GW signals were measured using the edge reflection [120] technique. FBG measures the changes in the wavelength shift due to the axial strain induced by the excited waves. The output is the change in the reflection from the laser light, which is then directly proportional to the photodetector's measured power. More details about the edge reflection technique are shown in subsection 2.3.3 and also in Figure 2.16.

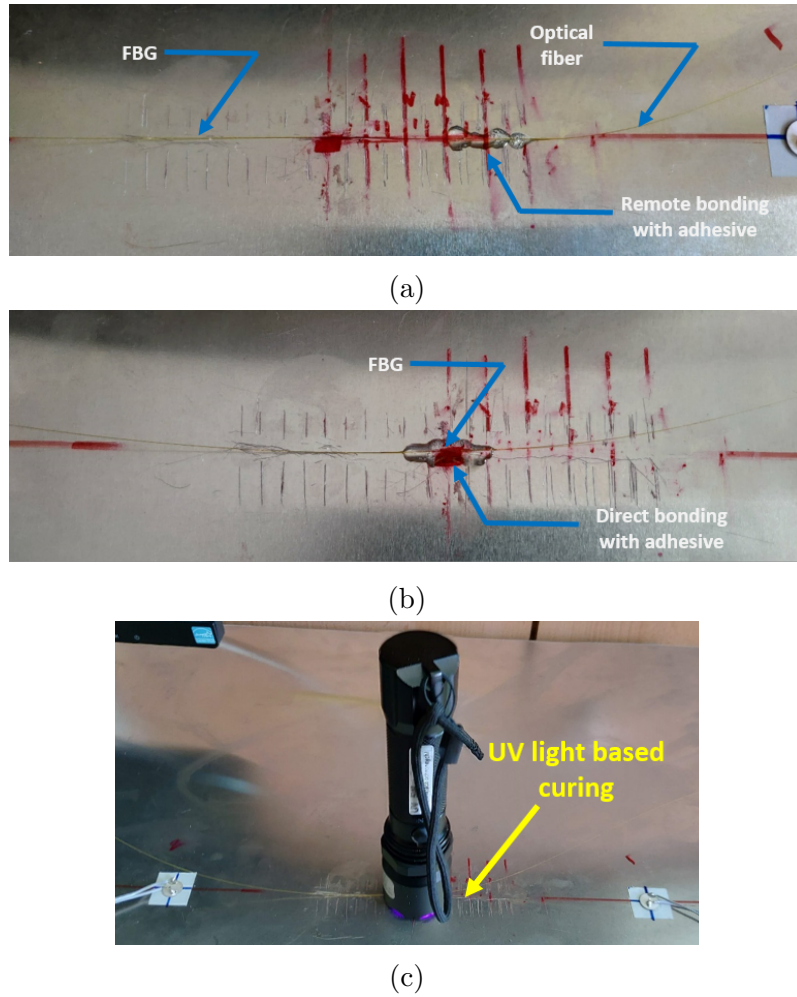


Figure 7.2: Process :(a) Remote bonding, (b) Direct bonding, (c) Curing.

The length of the adhesive was precisely changed to investigate the GW effects and their propagation through the fiber. The change in amplitude parameters was examined to confirm changes caused by the adhesive spread. For the remote bond arrangement (Figure 7.2a), the adhesive was applied on a length scale of  $H$  (1 cm) from the side of PZT1 (acting as an actuator) to  $4H$  (4 cm), as shown in Figure 7.3b. The length of the bond (the spread of the adhesive) was increased on both sides with a scale of  $H$  cm until it reached the length of  $4H$  cm for direct bonding (Figure 7.2b), as shown in Figure 7.3a. In total, three connection types, five frequencies, and four bond length types were investigated. The GW signals were obtained by averaging them 50 times. The expected GW results from the different connections are recorded in Table 7.1. The most difficult aspect of the experiment is measuring the GW because the configuration must be measured each time after carefully cleaning

the structure with hot water and then cured with UV source light, as shown in Figure 7.2c. Throughout the experiment, the reflectivity spectrum was checked almost every time to ensure that the laser's wavelength was set at the proper interval.

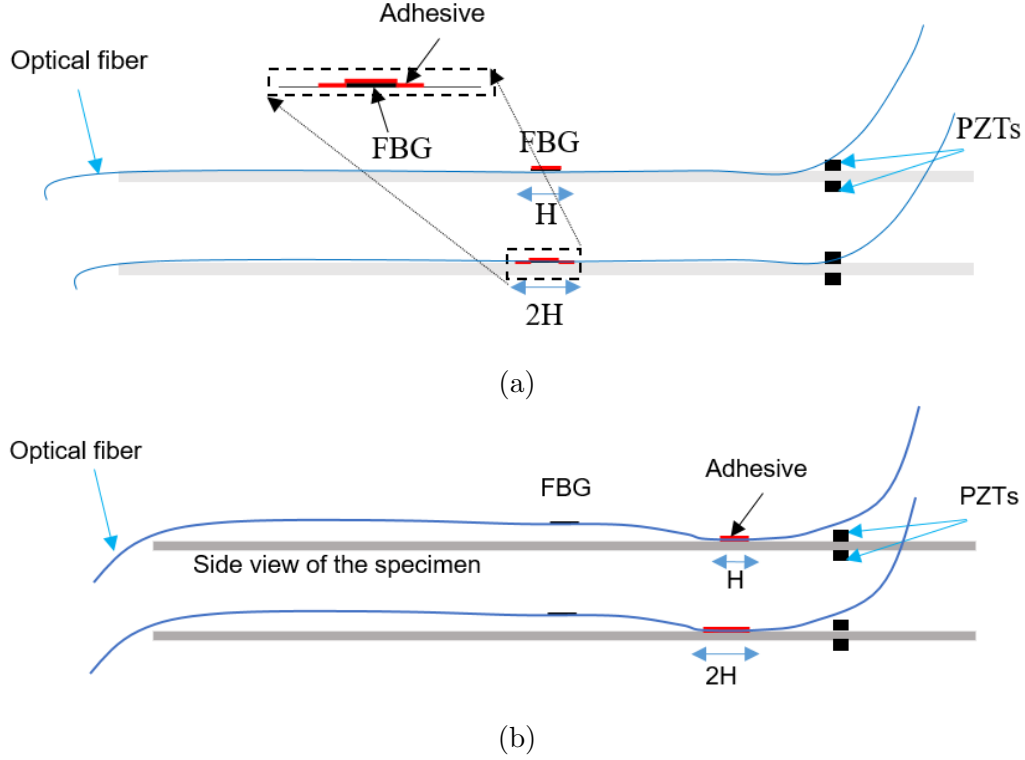


Figure 7.3: Schematic ALS cross-sectional configuration with (a) direct bonding, (b) remote bonding.

Connection type	Outcomes	Reason
Out phase (+,-)	amplifies A0 mode	Because of the negative polarity, the in-plane S0 mode is canceled, and the A0 mode is amplified.
In phase (+,+)	amplifies S0 mode	Because A0 mode is out-of-plane, the out-of-plane motion is cancelled in a phase connection, amplifying S0 mode
Normal (+)	A0, S0 mode	Signal with A0, S0 modes.

Table 7.1: PZT Connection types and effect of GW.



### 7.1.2 Results and Discussions

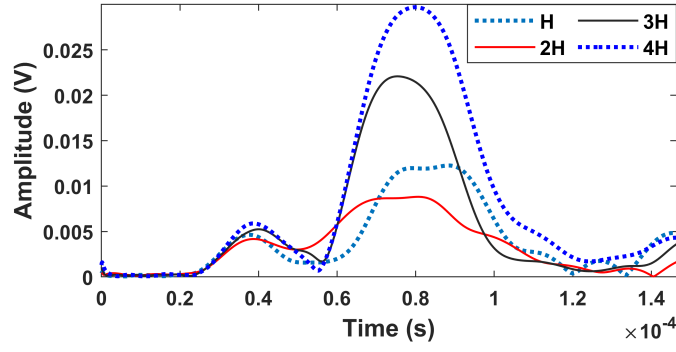
Figure 7.4 shows the GW signals obtained from the various connections mentioned (Table 7.1). Figure 7.4 shows the HT envelope of the GW signals obtained from the FBG sensor in a remote bonding configuration at various adhesive lengths. The fundamental GW modes are chosen based on PZT connections and the results of Table 7.1. It was discovered that as H moves closer to the FBG location, the amplitude value increases, making the connection a more direct bonding type (illustrated in Figure 7.5). As illustrated in Figure 7.5, the trend is observed in all remote bonding PZT connections.

The remote bonding study revealed that as the bonding length increases, the amplitude values of the peak values of the GW modes increase, and the trend can be seen in all three PZT connections. Similarly, direct bonding was tested at all three connections. An exemplary direct bonding configuration is shown in Figure 7.6 for out-phase PZT connection. Figure 7.7 shows the values of direct bonding PZT connections in descending order. The cause of the amplitude drop could be a higher strain applied due to the spread area/length of the adhesive (longer bond length), which masks the signal and causes an amplitude drop.

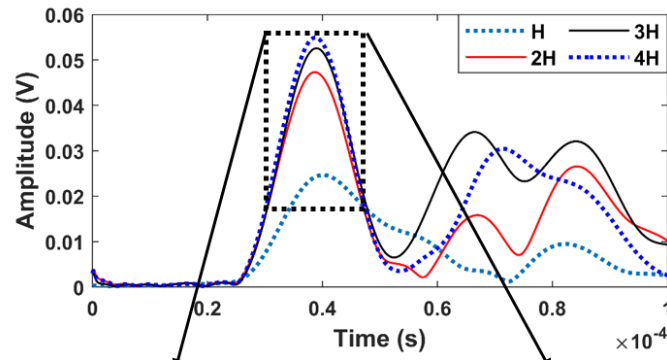
The bond length and its effects on the GW signals were investigated using FBG-based remote direct bonding with various PZT connections. It was discovered that the amplitude of the GW signals changed with the length of the adhesive spread. The results of using different PZT connections were also supported by the signal plots obtained from the experiments, which matched the reasoning.

## 7.2 FBG through thickness study: FEM study

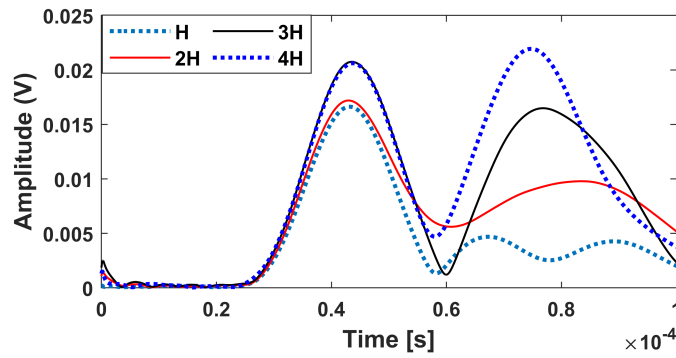
After studying direct and remote bonding studies, an extended study was performed to check the effect of embedding the FBG into a structure. A FEM direct bonding study was performed on a modelled homogeneous isotropic structure of dimensions  $50 \times 50 \times 1 \text{ cm}^3$  to study the sensitivity of the GW through the thickness of the specimen. In this case, a PZT actuator (A4) and one FBG sensor were modelled to achieve the pitch-catch configuration for sensing GW (Figure 7.8). The model with FBG elements/nodes at different layers of the structure is shown in Figure 7.9 with a zoomed-in picture of all modelled layers. Detailed analysis of the FEM modelling of the PZT-FBG SHM system is shown in subsection 6.4.1 and also in the author's paper [124].



(a)



(b)



(c)

Figure 7.4: Remote bonding : (a) A0 amplified, (b) S0 amplified, (c) S0, A0 modes.

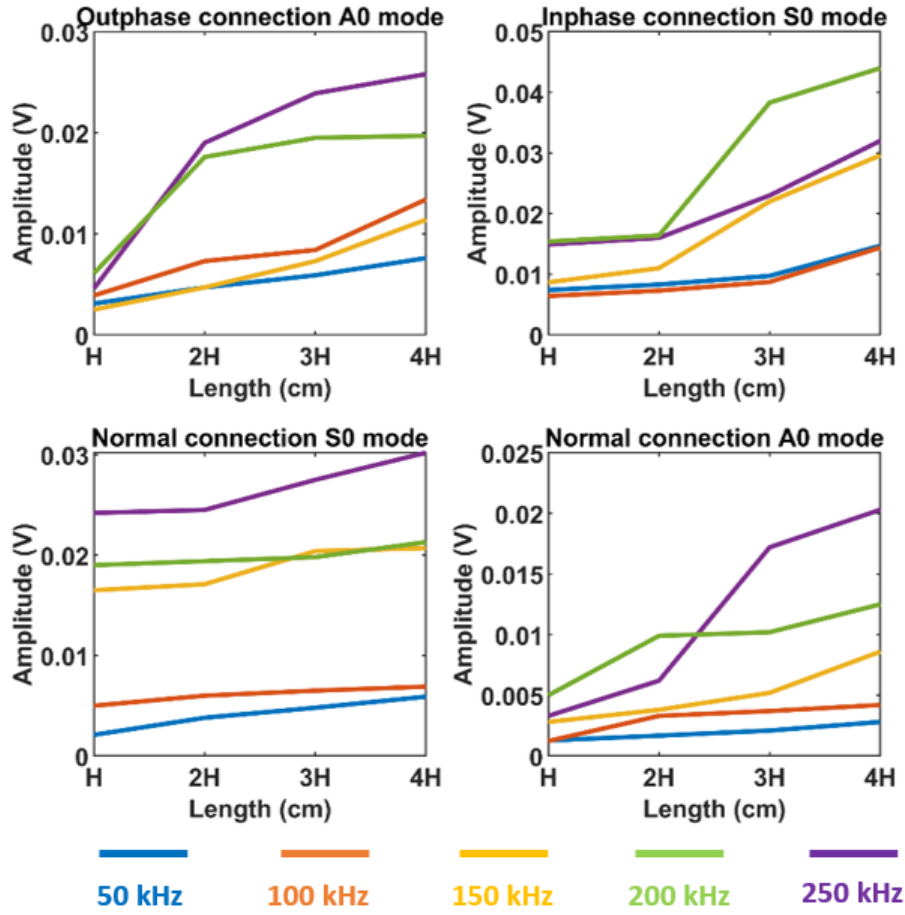


Figure 7.5: Amplitude pattern trend of remote bonded FBG at various frequencies and bond lengths.

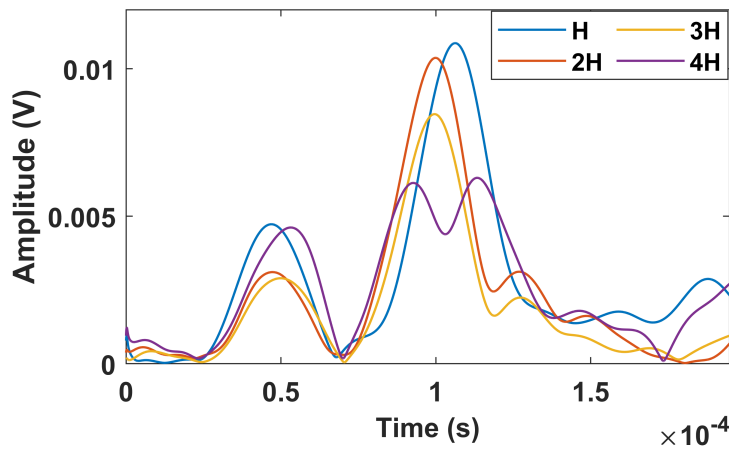


Figure 7.6: Exemplary HT envelope of out-phase direct bonding S0 GW mode at 100 kHz.

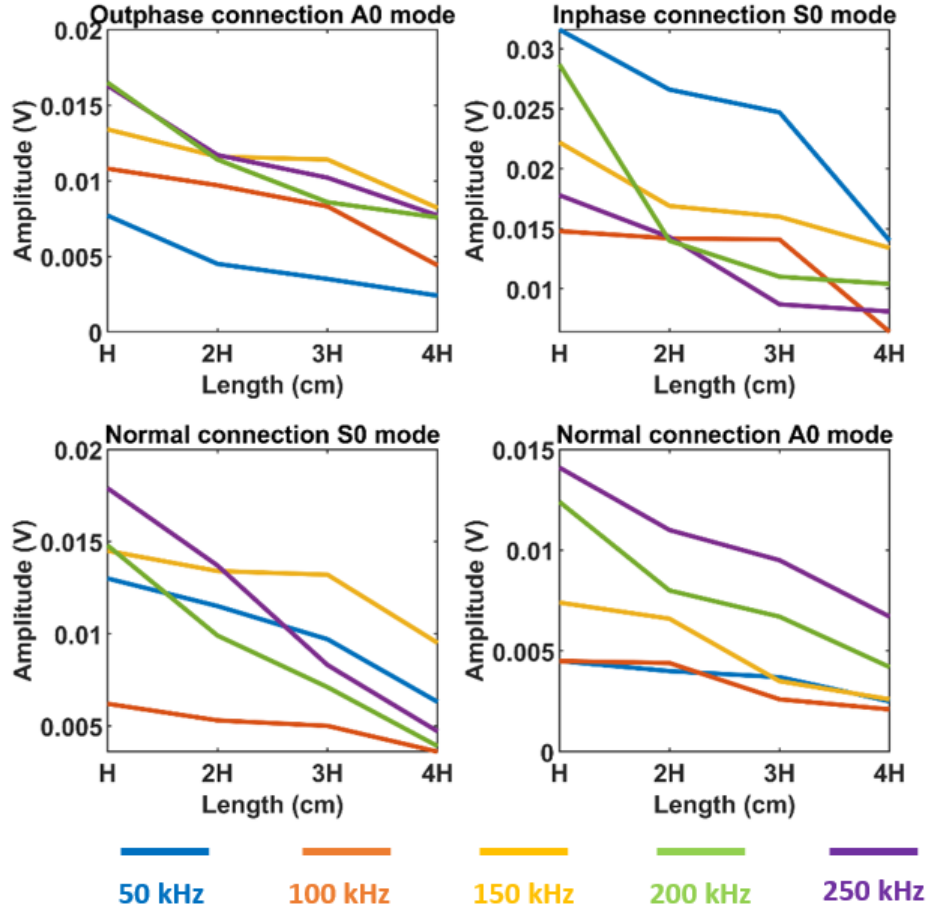


Figure 7.7: Amplitude pattern trend of direct bonded FBG at various frequencies and bond lengths.

The material properties used in the calculation are shown in Table 1 and the mesh parameters used are shown in Table A.2. The strain values obtained from the numerical FBG were converted to GW signal responses using the GUI as mentioned in Appendix A.6.1.

FEM analysis for a frequency of 50 kHz with A4 as actuator and FBG sensor, the GW signals are excited and plotted as shown in Figure 7.10 (in-plane direction). The overall thickness of the model was 0.01 m (1 cm) and 6 layers (0.001667 m each layer). The amplitude of the S0 mode from the in-plane direction is picked up for a frequency vs thickness study. From the theory [4], it was realized that for in-plane directions, the GW S0 mode shape through the thickness of the specimen shows a more linear oblique profile as shown in Figure 7.11 cosine fit. This FEM study demonstrated the relevance and agreement of the numerical simulation with the theory, demonstrating its potential for use in damage prediction.

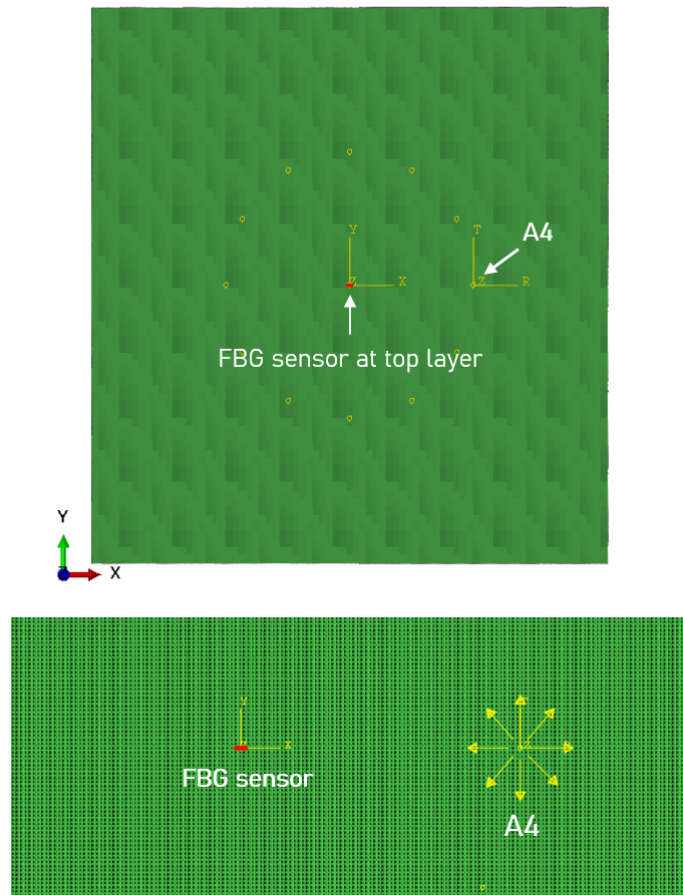


Figure 7.8: FEM FBG meshed model.

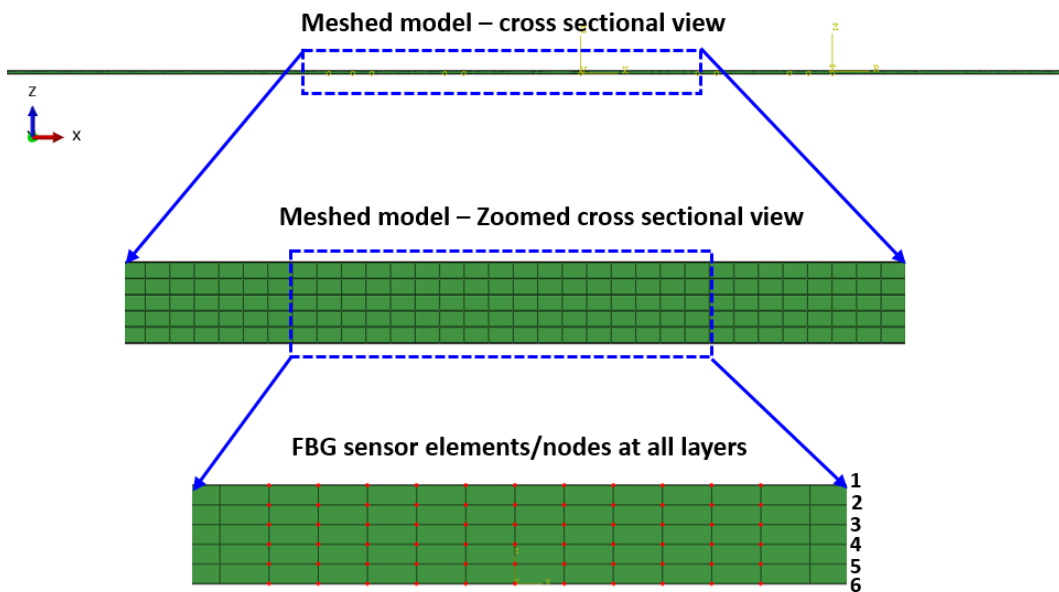


Figure 7.9: FEM model to check GW sensitivity.

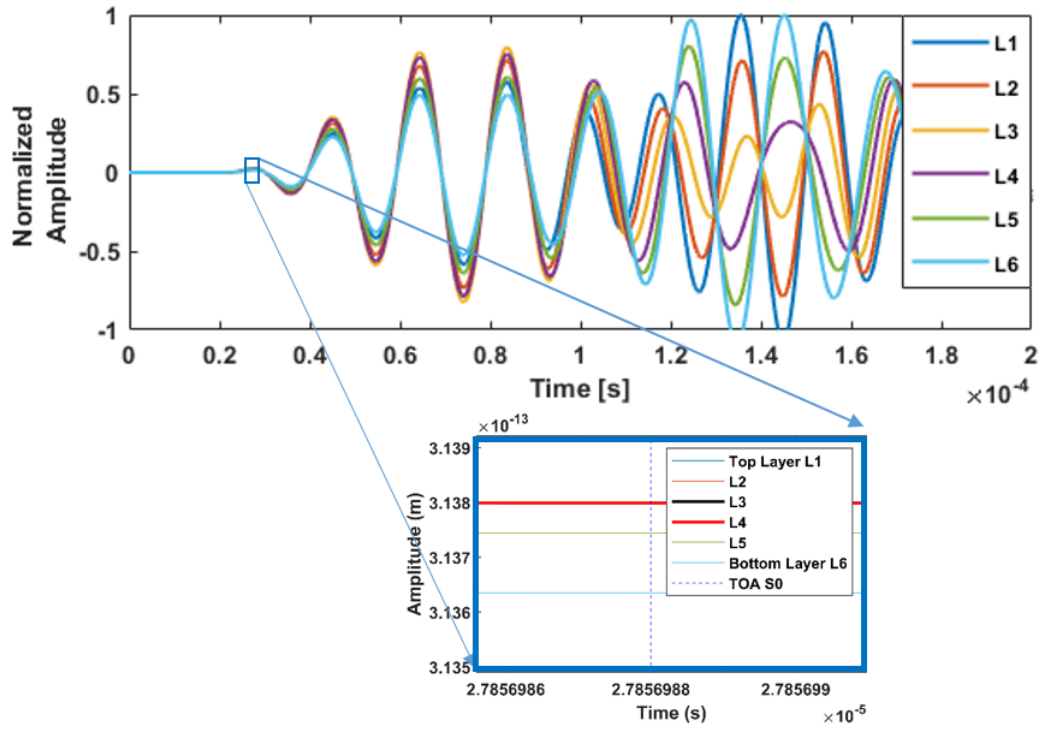


Figure 7.10: GW signals obtained via in-plane vibration.

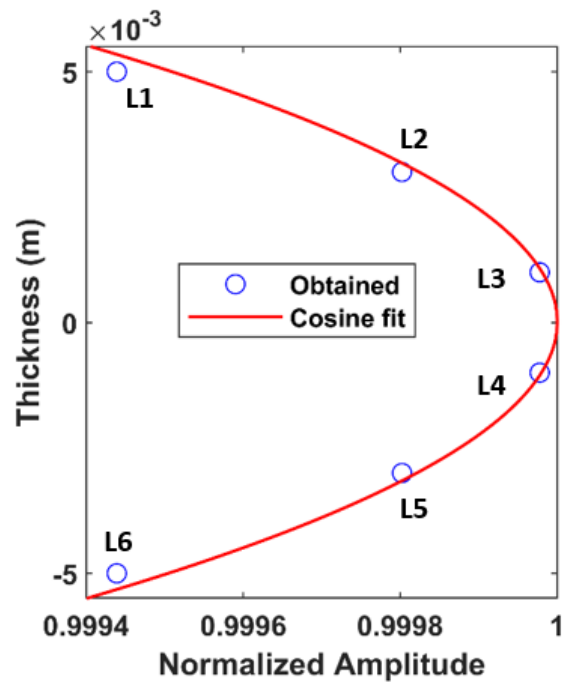


Figure 7.11: Frequency thickness profile.

## Chapter 8

### Conclusion and future work

#### 8.1 Thesis review: overall outcomes

Identification of different kinds of damage in different structures is very important for proving structural reliability and integrity. The damage detection (SHM level 1) is followed by damage localization (SHM level 2) and by quantification analysis (SHM level 3). For the identification of damage, the development of effective GW SHM systems is essential. An active monitoring approach requires a reliable and optimized sensor network that is capable of covering the entire structure of the study. An effective sensor network utilizing the GW-SHM system helps to pick up even a small crack or impact damage. The main objective of this thesis work involves evaluating different structures using a common multi-step SHM methodology by utilizing PZT-PZT, PZT-LDV and PZT-FBG sensing systems. Thus, using the multi-step method, SHM levels 1-3 are effectively achieved and are shown with various specimens.

The research work also involves quantification of the localized damages using CM formulations. The research work starts with the preliminary step which involves utilizing effective damage detection techniques in detecting the damages with the help of optimized sensor networks. After identifying the damage paths/region, the developed SEC algorithm is applied in localizing the damage coordinates. The SEC proved to reduce the overall calculation time and is tested on several isotropic and anisotropic structures. A CM-developed scheme is then utilized to quantify the damaged area. More details about the CM method are also mentioned in the author's paper in [107]. Thus, a rapid GW-based SHM method is proposed and tested in different types of structures for active monitoring. The complete structure of the thesis SHM levels achieve is shown in Figure 8.1.

The theory of waves and the concept of SHM in the assessment of various

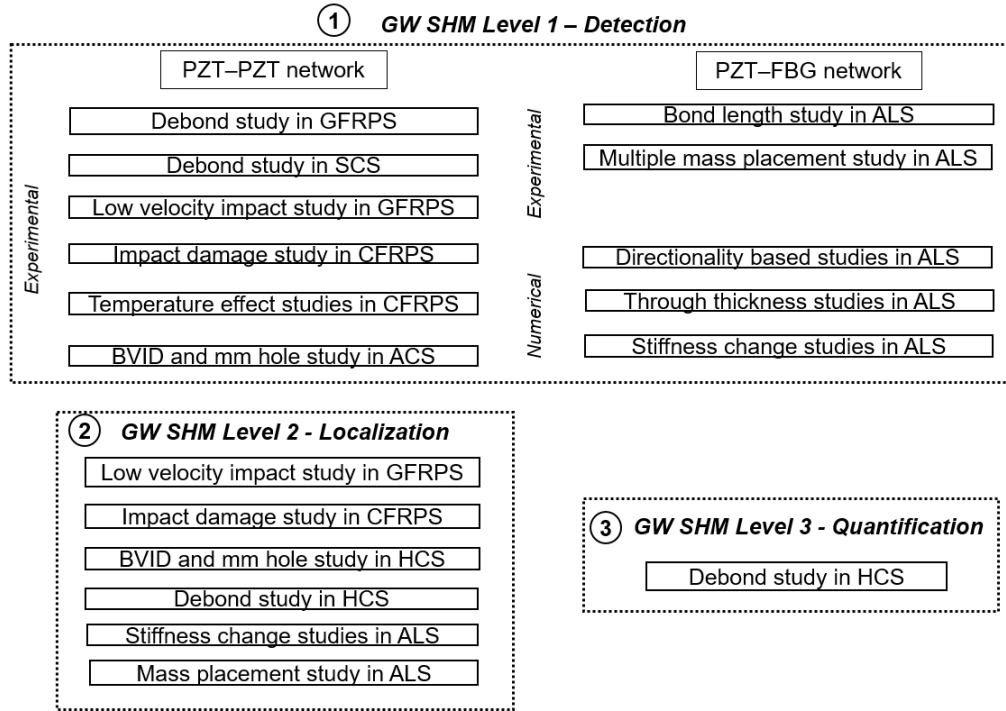


Figure 8.1: SHM levels 1-3 achieved using multi-step methodology.

structures are described in chapter 1. This chapter also introduces some results that prove the effectiveness of GW in SHM applications. Chapter 2 is about the literature review and instruments used in the thesis work. A literature survey to understand the state-of-the-art research work in damage imaging and the identified research gap is also presented in this chapter. Chapter 2 ends with the working principle of the instruments used in the thesis work for GW SHM monitoring.

Chapter 3 is about the research motive and the outline of the thesis. This chapter provides more information on research gaps and possible outcomes to solve. The chapter also focuses on the list of materials/ specimens used in the research study along with the damages that they are subjected to. Chapter 4 gives detailed information on the developed SEC method and a multi-step common methodology for damage identification purposes. Chapter 5 deals with utilizing the elliptical algorithm to actively monitor ACS structures. In the ACS specimen, different BVIDs and a smaller hole were localized using the elliptical algorithm. Additionally, the threshold-added elliptical method is successfully used to localize multiple impact damage analysis in GFRPS.

In chapter 6, the multi-step methodology utilized to assess multiple damages in various structures is explained in detail. In this chapter, the debond identi-



fication inside the SCS is elaborated on utilizing SHM multi-step methodology. The rapid process of identifying the multiple impact damages in CFRPS is explained in detail. In this chapter, numerical GW simulation with a PZT-FBG hybrid coupling process is used to analyze an ALS with the help of Abaqus FEM software. The damages are caused by making changes to the stiffness matrix (60 % reduction) in a few small regions of the ALS. Thus, the effectiveness of the multi-step approach is proved with both experimental and numerical models.

In chapter 7 Direct and remote bonding FBG configurations with different PZT connections were studied in detail in this chapter. The idea of effectively suppressing the GW modes is studied using different PZT configurations. A through-thickness analysis of the direct bonding study was explained using FEM analysis in this chapter.

## 8.2 Summary of the thesis contributions

The important contributions of the thesis work are summarized as points below;

- A common multi-step methodology is developed that could be used for different sensor types, materials and damage identification.
- The thesis discusses the use of the RMSD-based damage detection step to identify the damage paths when using PZT and LDV as sensor units. Such DI are quick in detecting the damaged sectors.
- CD-based DI in studying the damage paths from the PZT-FBG system (FBG as a sensor) data is explained in detail. The DI effectiveness is also proved with the data obtained from the developed 3D FEM numerical results.
- The effective use of the improved SEC method is explained elaborately in chapters 5, and 6, respectively. SEC's capability in detecting smaller impacts/dents, debond zones in SCS, artificially introduced damages, and stiffness-reduced regions from the 3D FEM models are all well elaborated in detail.
- The presence of damage near the actuator, far away region from the actuator, and presence of multiple damages are all effectively localized using the SEC method.
- The circular PZT network in SHM analysis proved to be effective in

localizing damages within and outside the sensor network. The sector-based area separation method developed from this concept proved to be effective in reducing overall calculation time.

- Damage quantification-based studies using CM formulations is explained by approximating the area of the debond in CFRPS.
- GW analysis of moving bond lengths is tested for the first time along with the combined different PZT configurations. The idea of effectively suppressing the GW modes is studied using remote and direct bonding of the FBG sensor by clubbing it with the PZT actuator network system. FBG embedding studies were performed numerically to check the theory of in-plane wave interactions.

The findings shown in this thesis work have been presented at numerous renowned conferences around the world and have also been published in conference proceedings. Eleven peer-reviewed journals have also been published so far with the thesis results and methods.

### 8.3 Future work

- The general limitations of the research work are the use of plate-like structures and PZT's temperature-bound performance (effective till 120 ° C as per the manufacturer's catalogue). The developed methodology in future studies will be subjected to complex structures with FBG as a sensor as it can effective up to 1200 ° C.
- Future studies also involve the evaluation of adhesive joints in structures using active structural monitoring methods. The studies of cyclic tensile and shear loading on different adhesive joints from the initial state until it reaches a plastic deformation will be actively monitored with PZT/FBG sensors.
- The PZT hybrid FBG sensing method to detect GW through the thickness in a composite structure is to be investigated further. The extended study involves embedding FBG at different depths of the composite structure and sensing the GW for damage analysis.
- FBG GW sensing analysis to monitor cracks on train rails, impact cracks in composites and debond in stiffener assemblies are all considered as future scope evaluation. The study also involves damage localization with the developed techniques and also verification with NDT techniques.

- In the thesis, remote bonding study has indeed shown higher magnitude at certain lengths. So, in future studies, the remote bonding configuration studies will be further put to new tests.
- In the thesis work, the study was carried out up to SHM level 3 of damage quantification. The future study involves adding prognosis-based structural monitoring applications to assess the lifetime period of the structures.

#### 8.4 Proven thesis

”Developed a common multi-step SHM methodology for reliable and accurate damage identification for piezoelectric-based, fiber optic-based and vibrometer-based sensing.”

The developed multi-step common method combines the use of PZT, LDV and FBG sensors for effective damage identification. It involves GW excitation, data acquisition, signal processing, feature extraction, and damage identification (steps 1,2 and 3). This technique offers early detection, improved accuracy, and reduced calculation time. The methodology was successful in locating various damages that were present in various material types detected by various sensor types. It was proven that a common SHM methodology was developed for reliable and accurate damage identification irrespective of sensor types used.

## Appendix A

### Appendix

#### A.1 ACS inspection

Figure A.1 at 150 kHz frequency shows Lamb wave propagation of the ACS specimen, revealing the damage. The experiment uses a frequency range from 10-200 kHz, and it was found that the 150 kHz frequency provides good results. The majority of the antisymmetric A0 mode waves are distinct and marked in the figure, while the S0 mode has a low amplitude. Wave reflections and mode changes occur when they enter the damaged area, which is crucial for visualizing the damage. BVID of 1.4 cm diameter is detected at 37  $\mu$ s, and analysis of wave pattern and detection of BVID of 1.8 cm are shown in the same figure at 48  $\mu$ s.

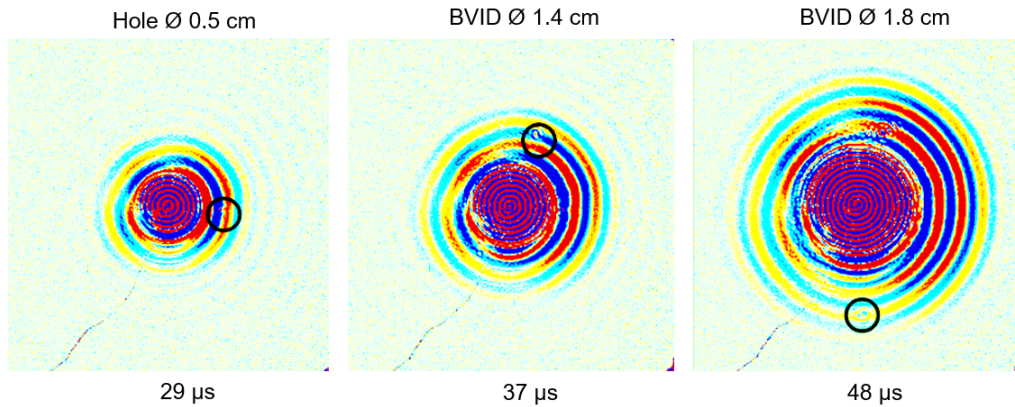


Figure A.1: FWF analysis at different time instances.

##### A.1.1 Velocity profile

Figure A.2 illustrates the calculation of the '*delt*' between two positions along the fiber orientations 0 ° and 90 ° fiber orientations for the GW signals in case

4. The velocity values  $0^\circ$  (2048 m/s) and  $90^\circ$  (2108 m/s) are used to create the velocity profile by fitting an elliptical function to them. This displays the whole  $360^\circ$  plot (Figure A.3). The details were then used in the elliptical algorithm as shown in subsection 5.1.4.

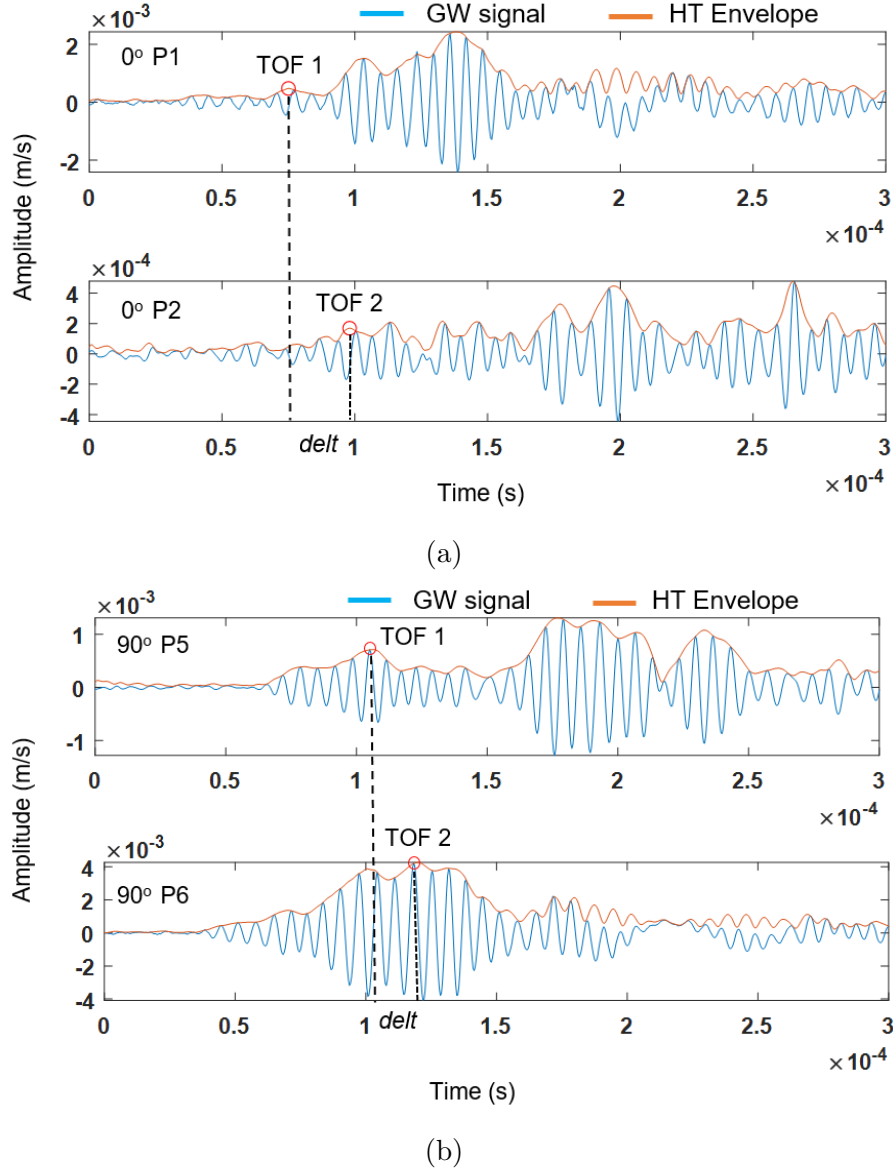


Figure A.2:  $delt$  calculation example of Case 4 signals at (a)  $0^\circ$  and (b)  $90^\circ$ .

## A.2 SCS inspection

The debonding detection (D1 and D2) using GW is shown in the FWF visualization plot (Figure A.4). The debonding is detected at an  $8.4 \mu\text{s}$  time instance by A0 GW mode. Velocity calculations are required to plot the GW

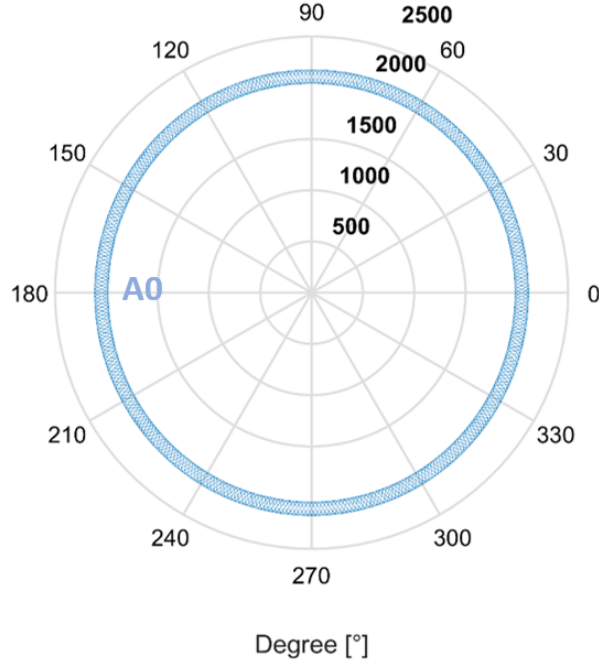


Figure A.3: Velocity profile from the LDV data for ACS specimen.

ellipses and to localize the damages. For both experimental and numerical signals, the values are obtained from S9S3, and S9S1 pairs located at  $0^\circ$ ,  $270^\circ$  (Table A.1). Because the CFRP ply orientation is along  $0^\circ/90^\circ$ , sensing pairs of  $0^\circ$  and  $270^\circ$  ( $-90^\circ$ ) were used to create the velocity profile, and it is slightly elliptical (Figure A.5).

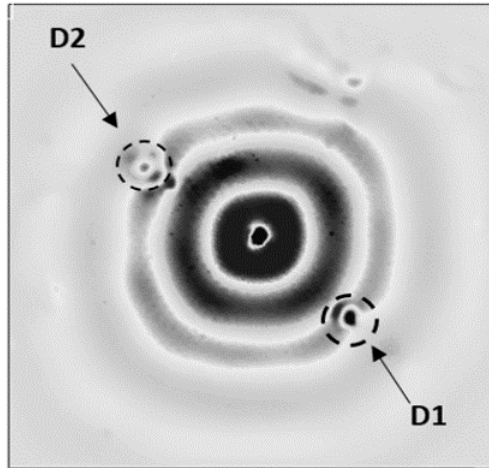


Figure A.4: Velocity profile from the LDV data for SCS specimen.

The debonding in FWF was identified by the A0 mode wavefield and is more visible as a separate wave packet at measured time instances. As a result,

Type	$V_{S0}$ at $0^\circ$	$V_{A0}$ at $0^\circ$	$V_{S0}$ at $270^\circ$	$V_{A0}$ at $270^\circ$
DAQR	3432 m/s	2130 m/s	3930 m/s	2586 m/s
FEM	3481 m/s	2208 m/s	3822 m/s	2497 m/s

Table A.1: Velocity values obtained from DAQR and Abaqus data.

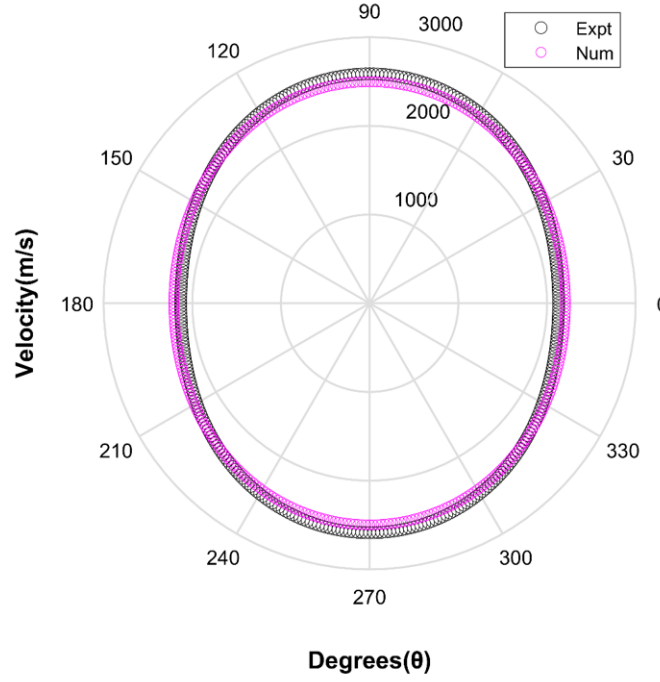


Figure A.5: Velocity profile based on values from Table A.1

it is chosen as the best GW mode, and the velocity values for the damage localization step are taken from this mode. Similarly, A0 mode velocity calculations are used to identify debonding in composite SCS [75],[76], Aluminium SCS [70]. When the sample is tested at higher temperatures conditions [66], positioning and glueing of PZTs [125], etc., there may be uncertainty/changes in the velocity measurements. A properly maintained room temperature and properly glued PZTs to SCS top skin prevented these circumstances. The A0 GW mode velocity ( $V_{A0}$ ) values obtained were then used to calculate the entire  $360^\circ$  values by fitting them with an elliptical function, as shown in Figure A.5. These values were later incorporated into the SEC damage localization method.

### A.3 CFRPS inspection

To identify the ICDs, the experimental and numerical data is analyzed using the RMS formulation [4],[93]. The findings of this study are depicted in Figure A.6, which shows the ICD region. In this research study, excitation frequencies of 50 and 100 kHz failed to identify the ICD when compared to 150 and 200 kHz. It has been discovered that 200 kHz identifies ICDs much better. RMS proved to be fast and accurate in detecting damage in CFRP multi-layered structures. In the following section, the excitation frequency for the SEC study is chosen to be 5 sine cycles, 200 kHz frequency with Hann windowed modulation.

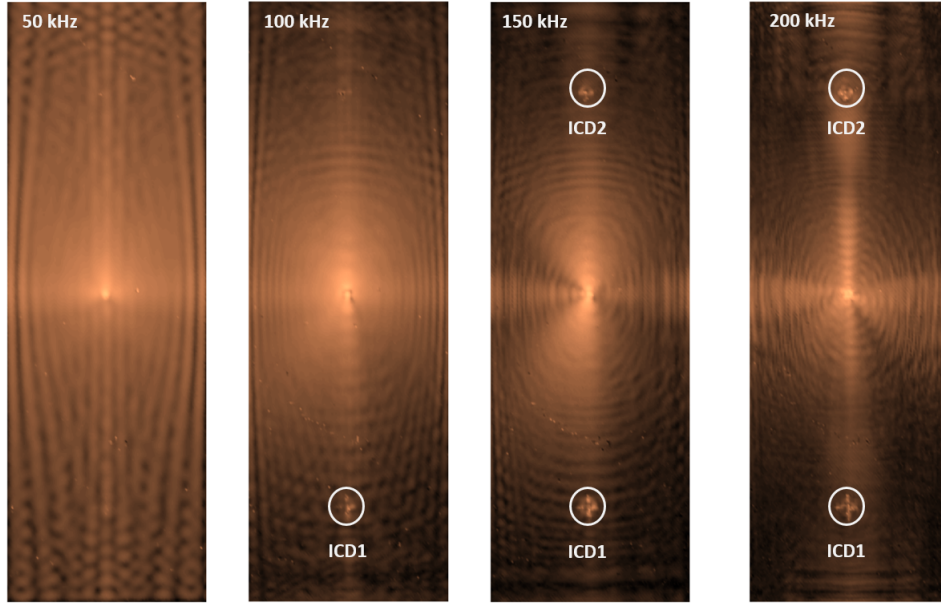


Figure A.6: RMS plots from LDV data at various excitation frequencies.

#### A.3.1 FWF waveform plots

At time instance 74  $\mu$ s in FWF (Figure A.7), mode conversion between S0 and A0 occurs, resulting in a new mode S0/A0+ at the ICD1, ICD2 where A0 is still visibly propagating. The coloured surface plots (Figure A.7) demonstrate the mode conversion phenomenon of S0/A0+ and thus the ICD. The A0+ mode is reflected from the sides of ICDs in the ICD1 zone, and internal reflections are also visible in the ICD2 zone.

Figure A.8 shows the 1D waveform plots displaying the primary A0 mode identified. The plots for the S1 sensing point (Figure 6.14c) with the HT envelope are shown. It found the greatest magnitude at A0. All other sensing



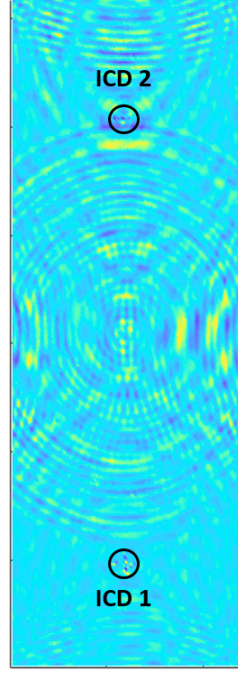


Figure A.7: FWF with S0/A0+ interaction.

points have similar cases. Figure A.9 depicts a comparison plot between the healthy and damaged signals obtained from S10 and S12. When compared to S12, S10 exhibits greater magnitude variation and larger signal dissimilarities. It emphasizes the source of the changes due to ICD. The A0 mode was chosen for the study because in most cases it exhibited as a wavepacket better than the mixed-up S0 mode.

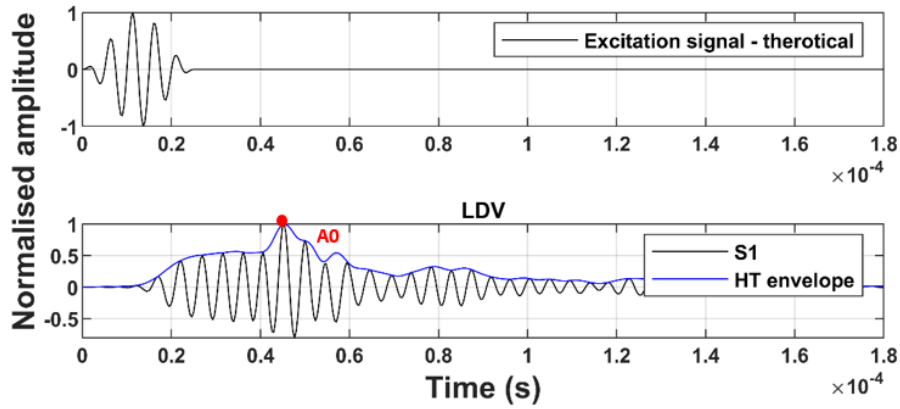


Figure A.8: 1D waveforms from theoretical and LDV data.

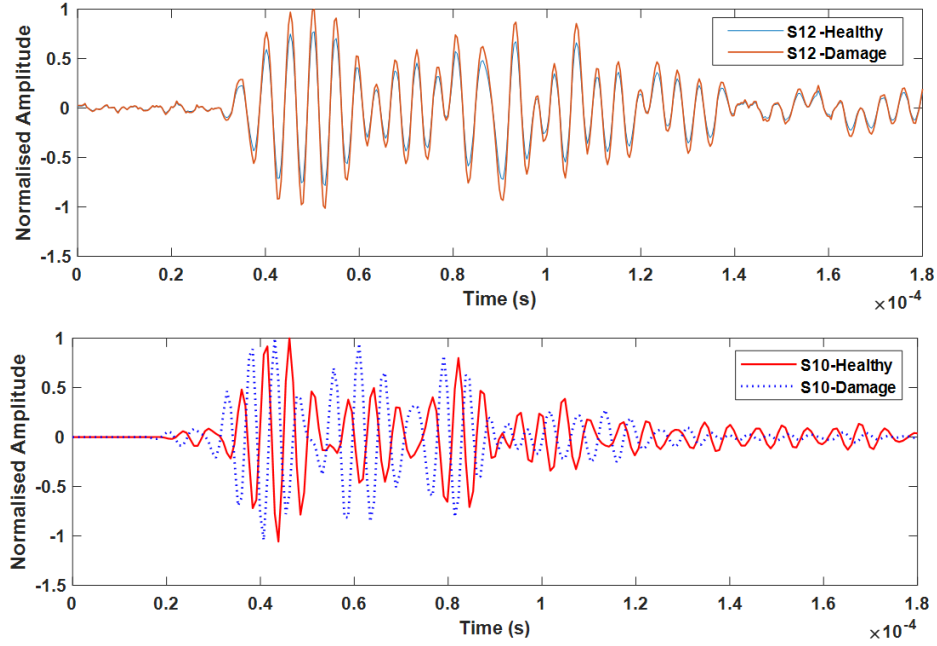


Figure A.9: Waveforms comparison plots from S10, S12 signals of LDV data.

#### A.4 ALS monitoring with FBGs

The two mediums that are taken into account when analyzing GW in plates are a bounded medium and an unbounded medium. The GWs are a superposition of longitudinal and shear waves that travel and disperse along the surface of the structure. The Dispersion calculator tool (<https://www.dlr.de/zlp/en/>) is used to determine the dispersion curves for a 1 mm thick aluminium structure, which depicts the movement of GW during propagation at various frequencies. Table A.2 displays the material characteristics that were used in the calculation. The dispersion curve values (group velocities) calculated using the calculator (theoretical values  $V_g$  Th) are shown in Figure A.10.

Material	Thickness m	E GPa	$\nu$	$\rho$ ( $kg/m^3$ )
ALS	0.01	74	0.33	2700

Table A.2: Material properties of ALS.

Because there are more modes present in the wave signals at higher operating frequencies and are therefore more challenging to interpret. In the majority of cases, the analysis takes into account the fundamental modes to eliminate such higher modes. The only fundamental modes that exist from the theoretical

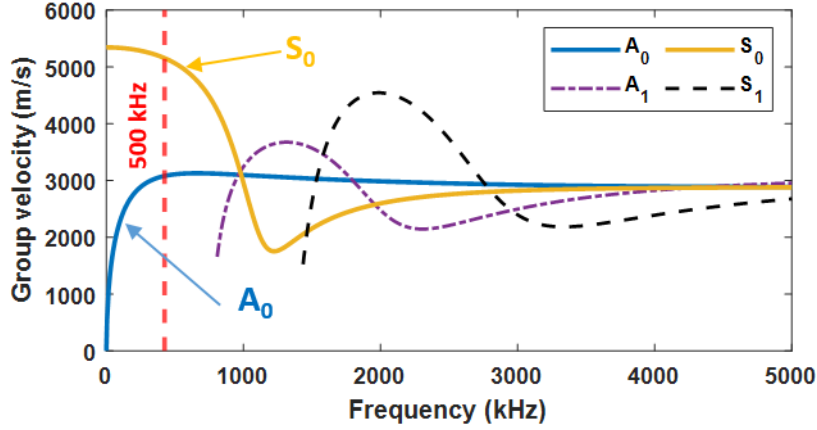


Figure A.10: Dispersion curves (Vg Th) for ALS.

results (Figure A.10) up to 500 kHz (denoted by a red dotted line) are A0 and S0. But, before starting the calculations an optimum frequency has to be selected for carrying out the detection and localization studies. So, an amplitude-based study [66] is conducted to identify the maximum A0 peak values for the analyzed frequencies of 50-250 kHz. The A0 mode is extremely sensitive to damage analysis [126] and many researchers [127], [122] use it to pinpoint where damage has occurred. Thus, in this research, the A0 mode is chosen for further studies.

The best frequency was determined to be 150 kHz excitation frequency because, when studied at most healthy (H) signals, it displayed the maximum A0 mode amplitude (direct wave). Figure A.11 displays an exemplary experimental study illustration of the maximum amplitude attained for the H case from each of the A (1–12) actuation. The mean values (MV) of all the frequencies are plotted in Figure A.11, and it is discovered that 150 kHz is characterized by the highest MV value, making it the frequency chosen for further investigation. The A0 GW mode velocity values obtained from the theoretical, experimental, and numerical studies are grouped in Table A.3. Due to the structure's homogeneity for 150 kHz, a group velocity of 2069 m/s for the A0 GW mode ( $V_{g_{A0}}$  Expt) is obtained throughout the structure. Similar results were found for the numerical case, where the group velocity values were 2164 m/s ( $V_{g_{A0}}$  Num).

## A.5 FEM Matlab pseudocode

The pseudocode algorithm 1 explains the flowchart algorithm used in the process of automating the FEM with Matlab linking. The algorithm connects

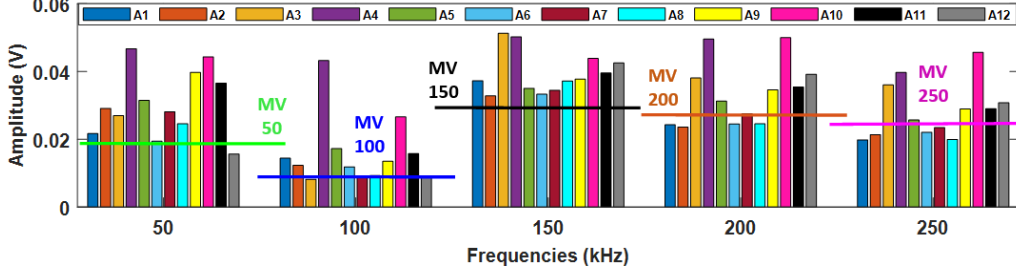


Figure A.11: Frequency (vs) Amplitude plot of A0 mode for H case.

Fr kHz	$V_{gA0}$ Th (m/s)	$V_{gA0}$ Expt (m/s)	$V_{gA0}$ Num (m/s)
50	1364	1289	1424
100	1759	1788	1744
150	2003	2069	2164
200	2278	2174	2334
250	2458	2362	2531

Table A.3: Comparing theoretical and numerical results.

the single FEM model with MATLAB codes and runs the same model, but changes the stiffness matrix (creating damages) at specific locations, as well as the frequencies and actuator numbers. The total run time for all actuators with a single damage scenario and frequency was 45 minutes. However, it was discovered that running a similar calculation with complete modelling took an average of 75 minutes and must be verified again before running. As a result, the pseudocode developed not only reduced the calculation time but also eliminated errors.

### A.5.1 FWF Analysis

The wavefield output is analyzed to determine the changes caused by damage and without damage (healthy state). Figure A.12 shows the FWF obtained at various time intervals through induced wave propagation (modelled) of PZT on a 3D ALS. Figure A.12(a) shows one example of an FWF with a damaged state (D1). The S0 mode propagates freely (Figure A.12 b), while the A0 mode propagates (Figure A.12c). Figure A.12d shows a zoomed-in view of wave reflection caused by the presence of D1. Velocity values are now checked using the signals obtained from the FBG sensor. The GW fundamental mode

---

**Algorithm 1** An algorithm to link Matlab with FEM

---

**Require:** FEM model to run iterative

**Ensure:** Change damage coords, frequencies and actuators

FEM

1: Full modelling of healthy, D1 model in Abaqus

2: Write the input file of the simulated job

3: Save elements and nodes as a text file

4: Save centre coords of all damages (D1:D6)

Matlab

5:  $i = 1; j = 1; n = 1$

6: For each Fr (i), A (n), D (j)

7: Call element sets, node sets

8: Call damage coords and pick the 3D area

9: Reduce the stiffness matrix (60

10 :  $i = i + 1; j = j + 1; n = n + 1$

11: End

12: Send results (.inp) to Abaqus 2 Matlab

13: Extract signals from .inp format and store them as .mat files

Where : Fr = frequency, A = actuators, D = damages. The stored files are then used in further signal-processing techniques in damage analysis.

---

group velocity values derived from numerical results are compared to theoretical results (obtained from the dispersion calculator as shown in the Appendix Figure A.10) and are well matched (Table A.3).

## A.6 FBG Reflectivity spectrum study

The Matlab-based GUI software tool was created to aid in simulating the FBG spectrum of an optical fiber at a specific location using a numerical model without the need to model the optical fiber. It is a better version of the SIMul tool [128] with added inputs for studying SEM calculations. This eliminates the need for a time-consuming experimental setup run. The most significant improvements are faster and more accurate transfer matrix calculations. These improvements are required due to the unique requirements for simulating GW propagation, which necessitates higher time sampling and greater spectrum representation accuracy. The extraction of spectrum shift and distortion values from the simulated spectrum is another important implementation. The change in the maximum value determines the shift in the spectrum, distortion is measured by the change in full width at half maximum (FWHM).

The tool includes/can take in simulation results from the SEM study in ad-

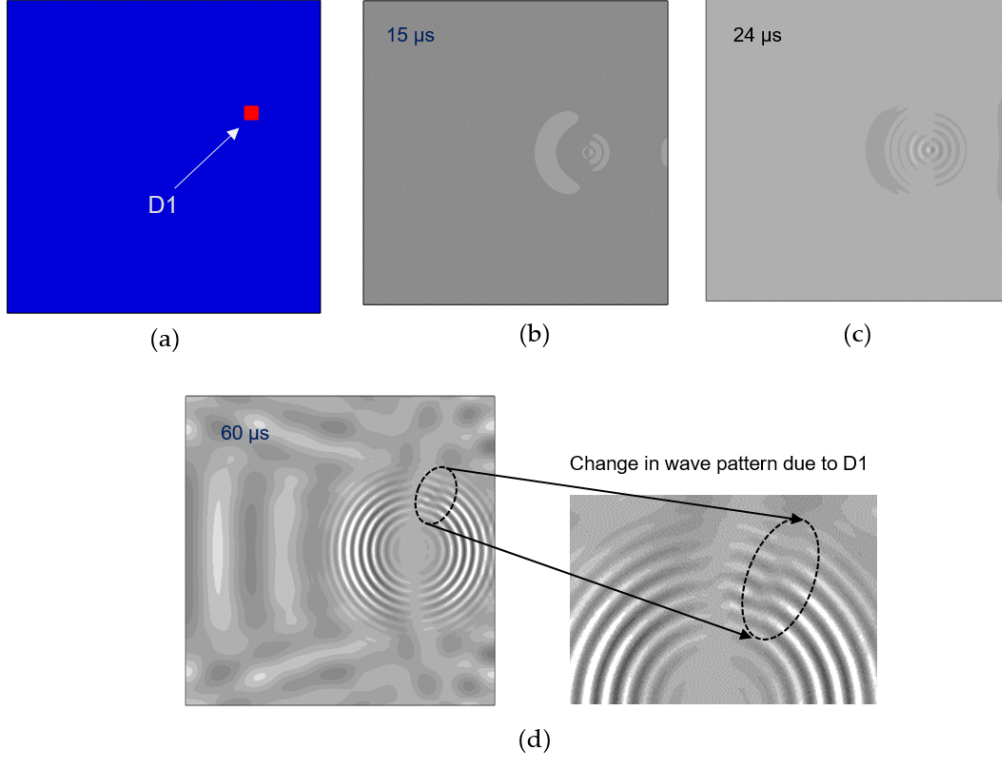
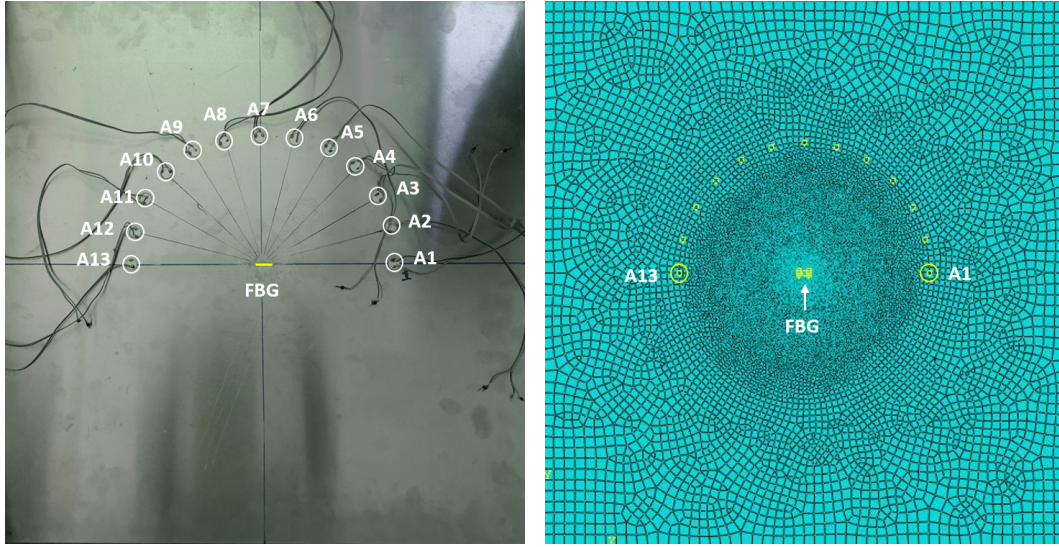


Figure A.12: ALS FEM model:(a) Model with D1, (b) S0 mode, (c) A0 mode, (d) Change in wave pattern due to D1.

dition to identifying the computationally expensive nature of GW simulations using FEM. For validation, an ALS plate was modelled. To perform FEM calculations, the Abaqus tool was used. A total of 13 PZTs arranged in a semi-circle array, each separated by  $15^\circ$ , were used to create a 2D shell ALS (Figure A.13). PZTs excite the GW, which is detected by the FBG in the centre of the plate. The FBG sensor primarily captures higher amplitude signals when they are parallel to the PZT actuators (in this case A1 and A13). Because FBGs sensing is highly unidirectional, placing it perpendicularly will catch low-amplitude signals. This is termed as directional sensitivity of the FBG sensor. The signals obtained from A13-FBG (parallel) and A7-FBG (perpendicular) are shown in Figure A.14 for further explanation. The experimental results were compared with a modelled frequency range of 50 to 250 kHz (in steps of 50 kHz). Figure A.13a shows the experimental ALS studied with 13 PZTs acting as actuators and 1 FBG as a sensor, as well as the corresponding 2D FEM numerical model and settings (Figure A.13b) created. Table A.2 shows the material properties used in the FEM calculation. The instrumentation used to acquire the experimental signals is described in detail in [117].



(a) Experimental ALS.

(b) Numerical ALS.

Figure A.13: Models used in the GUI build up.

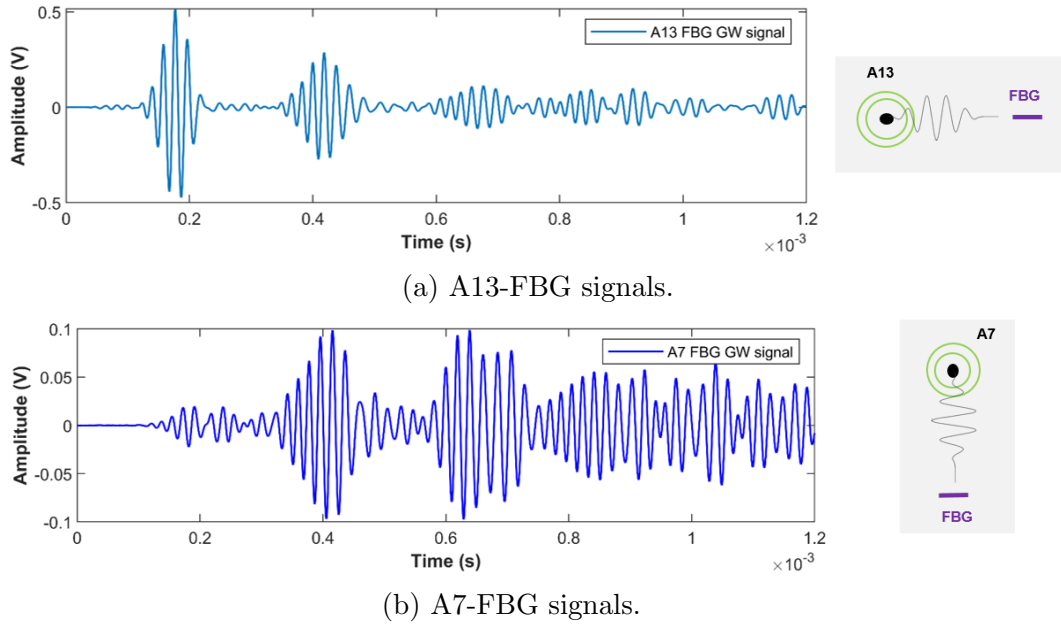


Figure A.14: Directional sensitivity analysis.

### A.6.1 GUI Matlab-based toolbox

The undeformed, uniform, non-uniform, and transverse strain values were extracted from the Abaqus model (.odb) files using a Python-based code. Tab 1's specifications are as follows:

Tab 1: Figure A.15 shows the extraction tab and its purposes.



- Select Stress / Strain files: there are two options for uploading a single file and verifying the reflectivity curves (or) uploading a directory and checking two or more files at once.
- Extraction: two options for obtaining and validating stress/strain values from nodes, as well as simply validating/visualizing the obtained files by importing them.
- Stress/strain files: display various stress/strain values in a table format.







Extract Stress/Strain		FBG Simulation	FBG signal variation	Developed at  						
1. Select Stress/ Strain files		2. Extraction		3. Stress/Strain table values						
 Import File   Import Directory		 File to Table   Nodes LE/S to Table		X	LE11	LE22	LE33	S11	S22	S3
				0	1.0000e-06	-3.0200e-08	2.0800e-08	-1670	-2750	
				1.0000e-04	1.0000e-06	-3.0200e-08	2.2700e-08	-1960	-2840	
				2.0000e-04	1.0000e-06	-3.0300e-08	2.4600e-08	-2260	-2950	
				3.0000e-04	1.0000e-06	-3.0200e-08	2.6500e-08	-2560	-3050	
				4.0000e-04	1.0000e-06	-3.0200e-08	2.8300e-08	-2860	-3140	
				5.0000e-04	1.0000e-06	-3.0100e-08	3.0100e-08	-3140	-3230	
				6.0000e-04	1.0000e-06	-2.9900e-08	3.1800e-08	-3420	-3320	
				7.0000e-04	1.0000e-06	-2.9800e-08	3.3500e-08	-3690	-3400	
				8.0000e-04	1.0000e-06	-2.9700e-08	3.5100e-08	-3950	-3480	
				9.0000e-04	1.0000e-06	-2.9500e-08	3.6600e-08	-4200	-3550	
				1.0000e-03	1.0000e-06	-2.9400e-08	3.8100e-08	-4440	-3620	
				0.0011	1.0000e-06	-2.9200e-08	3.9400e-08	-4660	-3690	
				0.0012	1.0000e-06	-2.9100e-08	4.0700e-08	-4880	-3750	
				0.0013	1.0000e-06	-2.8900e-08	4.2000e-08	-5080	-3810	
				0.0014	1.0000e-06	-2.8700e-08	4.3100e-08	-5270	-3860	
				0.0015	1.0000e-06	-2.8600e-08	4.4200e-08	-5450	-3910	
				0.0016	1.0000e-06	-2.8400e-08	4.5200e-08	-5610	-3950	
				0.0017	1.0000e-06	-2.8200e-08	4.6100e-08	-5770	-3990	
				0.0018	1.0000e-06	-2.8000e-08	4.6900e-08	-5900	-4020	
				0.0019	1.0000e-06	-2.7800e-08	4.7600e-08	-6030	-4050	
				0.0020	1.0000e-06	-2.7600e-08	4.8200e-08	-6140	-4070	
				0.0021	1.0000e-06	-2.7400e-08	4.8800e-08	-6230	-4090	
				0.0022	1.0000e-06	-2.7200e-08	4.9200e-08	-6310	-4100	
				0.0023	1.0000e-06	-2.7000e-08	4.9600e-08	-6380	-4110	

Figure A.15: Data extraction tab.

Tab 2: Based on the number of orders shown in Figure A.16;

- Select Stress / Strain files: there are two options for uploading a single file and verifying the reflectivity curves (or) uploading a directory and checking two or more files at once.
- Simulation type: Three options-uniform, non-uniform, and transverse strain simulation. It is designed to calculate from FEM Abaqus and SEM. The simulation button plots the undeformed state with the selected strain options.
- Optical fiber parameters: Constant values are used to calculate reflectivity curves.



- FBG array configuration: Constant values are required to run the calculation.
- Strain graph: linked to all other subtabs and displays the result graphs.
- Control buttons: to assist the user with any questions about the tool and to restore the values to their original state (defaults).

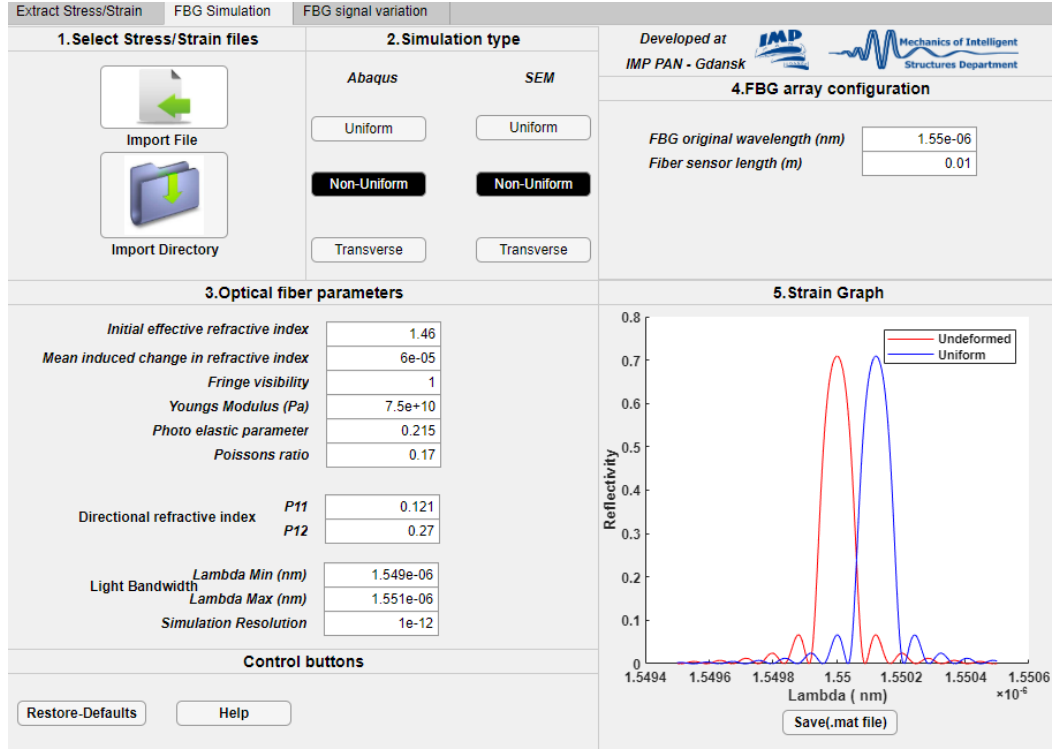


Figure A.16: FBG reflectivity spectrum calculation tab.

Tab 3: The specifications listed on the tab are as follows:

- The mat file from Tab 2 can be post-processed and analyzed according to user specifications.
- Draw an FWHM Gaussian plot.
- Show the difference in the peak shift and wavelength.

### A.6.2 Validation

To validate the results, a value from the numerical result (after converting the strains to FBG response via the GUI) is cross-checked with the experimental signal. As shown in Figure A.17, an exemplary experimental signal from 50 kHz actuator 1 is cross-checked with an actuator1 at 50 kHz numerical signal

obtained from the region of interest/slope (Figure 2.16). The values matched well showing the accuracy of the numerical model.

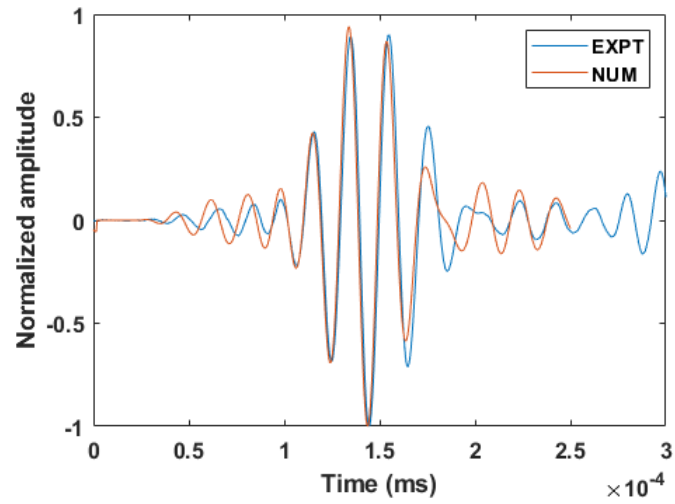


Figure A.17: Validation of GW signals.

## Bibliography

- [1] J. L. Rose, *Ultrasonic guided waves in solid media*. Cambridge university press, 2014.
- [2] “Aviation Safety Network.” [https://reports.aviation-safety.net/2005/20050814-0\\_B733\\_5B-DBY.pdf](https://reports.aviation-safety.net/2005/20050814-0_B733_5B-DBY.pdf). Accessed: 2022-09-30.
- [3] Z. Su and L. Ye, *Identification of damage using Lamb waves: from fundamentals to applications*, vol. 48. Springer Science & Business Media, 2009.
- [4] V. Giurgiutiu, *Structural health monitoring: with piezoelectric wafer active sensors*. Elsevier, 2007.
- [5] M. Mitra and S. Gopalakrishnan, “Guided wave based structural health monitoring: A review,” *Smart Materials and Structures*, vol. 25, no. 5, p. 053001, 2016.
- [6] W. Ostachowicz, R. Soman, and P. Malinowski, “Optimization of sensor placement for structural health monitoring: A review,” *Structural Health Monitoring*, vol. 18, no. 3, pp. 963–988, 2019.
- [7] F. J. Pallarés, M. Betti, G. Bartoli, and L. Pallarés, “Structural health monitoring (SHM) and Nondestructive testing (NDT) of slender masonry structures: A practical review,” *Construction and Building Materials*, vol. 297, p. 123768, 2021.
- [8] Y. An, E. Chatzi, S.-H. Sim, S. Laflamme, B. Blachowski, and J. Ou, “Recent progress and future trends on damage identification methods for bridge structures,” *Structural Control and Health Monitoring*, vol. 26, no. 10, p. e2416, 2019.
- [9] F. Ricci, E. Monaco, N. Boffa, L. Maio, and V. Memmolo, “Guided waves for structural health monitoring in composites: A review and implementation strategies,” *Progress in Aerospace Sciences*, vol. 129, p. 100790, 2022.

- [10] Z. Kotulski, “Elastic waves in randomly stratified medium. numerical calculations,” *Acta mechanica*, vol. 92, no. 1, pp. 143–163, 1992.
- [11] H. Huang and K. Balusu, “A theoretical/numerical study on ultrasound wave coupling from structure to remotely bonded fiber Bragg grating ultrasound sensor,” *Journal of Nondestructive Evaluation, Diagnostics and Prognostics of Engineering Systems*, vol. 4, no. 2, 2021.
- [12] J. Wee, *Enhancement of ultrasonic Lamb wave transfer to fiber Bragg grating sensors through remote bonding*. PhD thesis, North Carolina State University, 2018.
- [13] J. Wee, D. Hackney, P. Bradford, and K. Peters, “Experimental study on directionality of ultrasonic wave coupling using surface-bonded fiber Bragg grating sensors,” *Journal of Lightwave Technology*, vol. 36, no. 4, pp. 932–938, 2017.
- [14] L. Rayleigh, “On waves propagated along the plane surface of an elastic solid,” *Proceedings of the London mathematical Society*, vol. 1, no. 1, pp. 4–11, 1885.
- [15] W. J. Staszewski, “Structural health monitoring using guided ultrasonic waves,” in *Advances in smart technologies in structural engineering*, pp. 117–162, Springer, 2004.
- [16] T. Wang, *Finite element modelling and simulation of guided wave propagation in steel structural members*. PhD thesis, University of Western Sydney (Australia), 2014.
- [17] A. E. H. Love, *Some Problems of Geodynamics: Being an Essay to which the Adams Prize in the University of Cambridge was Adjudged in 1911*. University Press, 1911.
- [18] H. Lamb, “On waves in an elastic plate,” *Proceedings of the Royal Society of London. Series A, Containing papers of a mathematical and physical character*, vol. 93, no. 648, pp. 114–128, 1917.
- [19] M. Heesch, M. Dziendzikowski, K. Mendrok, and Z. Dworakowski, “Diagnostic-quality guided wave signals synthesized using generative adversarial neural networks,” *Sensors*, vol. 22, no. 10, p. 3848, 2022.
- [20] S. Shoja, V. Berbyuk, and A. Boström, “Delamination detection in composite laminates using low frequency guided waves: Numerical simulations,” *Composite Structures*, vol. 203, pp. 826–834, 2018.

- [21] S. Kowalczyk, S. Matysiak, and D. M. Perkowski, "On some problems of SH wave propagation in inhomogeneous elastic bodies," *Journal of Theoretical and Applied Mechanics*, vol. 54, no. 4, pp. 1125–1135, 2016.
- [22] M. Osika, A. Ziaja-Sujdak, R. Radecki, L. Cheng, and W. Staszewski, "Nonlinear modes in shear horizontal wave propagation-analytical and numerical analysis," *Journal of Sound and Vibration*, vol. 540, p. 117247, 2022.
- [23] P. Kijanka, W. J. Staszewski, and P. Packo, "Generalised semi-analytical method for excitability curves calculation and numerical modal amplitude analysis for Lamb waves," *Structural Control and Health Monitoring*, vol. 25, no. 7, p. e2172, 2018.
- [24] D. Gao, Y. Ma, Z. Wu, Y. , and H. Lu, "Guided wave based damage detection method for aircraft composite structures under varying temperatures," *Structural Durability & Health Monitoring*, vol. 15, no. 1, p. 23, 2021.
- [25] K. Balasubramaniam, P. Fiborek, D. Ziaja, M. Jurek, M. Sawczak, R. Soman, and P. H. Malinowski, "Global and local area inspection methods in damage detection of carbon fiber composite structures," *Measurement*, vol. 187, p. 110336, 2022.
- [26] K. Grabowski, S. Srivatsa, A. Vashisth, L. Mishnaevsky Jr, and T. Uhl, "Recent advances in mxene-based sensors for Structural Health Monitoring applications: a review," *Measurement*, p. 110575, 2021.
- [27] A. Katunin, I. Pivdiablyk, L. Gornet, and P. Rozycki, "A hybrid method for determination of fatigue limit and non-destructive evaluation of composite structures after low-velocity impact loading," *Composites Part B: Engineering*, vol. 238, p. 109898, 2022.
- [28] P. H. Malinowski, T. Wandowski, and S. K. Singh, "Employing principal component analysis for assessment of damage in GFRP composites using electromechanical impedance," *Composite Structures*, vol. 266, p. 113820, 2021.
- [29] C.-K. Soh, Y. Yang, and S. Bhalla, *Smart materials in structural health monitoring, control and biomechanics*. Springer Science & Business Media, 2012.

- [30] W. Li, T. Liu, D. Zou, J. Wang, and T.-H. Yi, “PZT based smart corrosion coupon using electromechanical impedance,” *Mechanical Systems and Signal Processing*, vol. 129, pp. 455–469, 2019.
- [31] T. Wandowski, P. Malinowski, and W. Ostachowicz, “Improving the emi-based damage detection in composites by calibration of ad5933 chip,” *Measurement*, vol. 171, p. 108806, 2021.
- [32] P. B. Dao, M. Fortuna, W. J. Staszewski, and T. Uhl, “An experimental study on the effect of temperature on acoustic emission characteristics in metallic structures,” in *IFTToMM World Congress on Mechanism and Machine Science*, pp. 2863–2872, Springer, 2019.
- [33] R. Lima, M. Drobiazko, A. Bernasconi, and M. Carboni, “On crack tip localisation in quasi-statically loaded, adhesively bonded double cantilever beam specimens by acoustic emission,” *Theoretical and Applied Fracture Mechanics*, vol. 118, p. 103286, 2022.
- [34] A. Wronkowicz-Katunin, A. Katunin, and K. Dragan, “Reconstruction of barely visible impact damage in composite structures based on non-destructive evaluation results,” *Sensors*, vol. 19, no. 21, p. 4629, 2019.
- [35] P. Pyzik, A. Ziaja-Sujdak, J. Spytek, M. O’Donnell, I. Pelivanov, and L. Ambrozinski, “Detection of disbonds in adhesively bonded aluminum plates using laser-generated shear acoustic waves,” *Photoacoustics*, vol. 21, p. 100226, 2021.
- [36] A. Spada, M. Capriotti, and F. L. di Scalea, “Global-local model for guided wave scattering problems with application to defect characterization in built-up composite structures,” *International Journal of Solids and Structures*, vol. 182, pp. 267–280, 2020.
- [37] R. Boettcher, M. Kunik, S. Eichmann, A. Russell, and P. Mueller, “Revisiting energy dissipation due to elastic waves at impact of spheres on large thick plates,” *International Journal of Impact Engineering*, vol. 104, pp. 45–54, 2017.
- [38] C.-A. Holst, V. Lohweg, K. Röckemann, and A. Steinmetz, “Wave-based quality inspection of repaired Carbon Fibre Reinforced Polymers for on-site aircraft maintenance,” in *2019 24th IEEE International Conference on Emerging Technologies and Factory Automation (ETFA)*, pp. 1643–1646, IEEE, 2019.

- [39] K. Dziedziech and W. J. Staszewski, “Wavelet-based transmissibility for the analysis of time-variant systems,” *Mechanical Systems and Signal Processing*, vol. 145, p. 106918, 2020.
- [40] J. Spytek, A. Ziaja-Sujdak, K. Dziedziech, L. Pieczonka, I. Pelivanov, and L. Ambrozinski, “Evaluation of disbonds at various interfaces of adhesively bonded aluminum plates using all-optical excitation and detection of zero-group velocity Lamb waves,” *NDT & E International*, vol. 112, p. 102249, 2020.
- [41] Y. Lugovtsova, J. Bulling, O. Mesnil, J. Prager, D. Gohlke, and C. Boller, “Damage quantification in an aluminium-CFRP composite structure using guided wave wavenumber mapping: Comparison of instantaneous and local wavenumber analyses,” *NDT & E International*, vol. 122, p. 102472, 2021.
- [42] R. K. Munian, D. R. Mahapatra, and S. Gopalakrishnan, “Ultrasonic guided wave scattering due to delamination in curved composite structures,” *Composite Structures*, vol. 239, p. 111987, 2020.
- [43] P. Deng, O. Saito, Y. Okabe, and H. Soejima, “Simplified modeling method of impact damage for numerical simulation of Lamb wave propagation in quasi-isotropic composite structures,” *Composite Structures*, vol. 243, p. 112150, 2020.
- [44] B. Zima and J. Moll, “Theoretical and experimental analysis of guided wave propagation in plate-like structures with sinusoidal thickness variations,” *Archives of Civil and Mechanical Engineering*, vol. 23, no. 1, pp. 1–19, 2023.
- [45] F. Lambinet and Z. S. Khodaei, “Measurement platform for structural health monitoring application of large scale structures,” *Measurement*, vol. 190, p. 110675, 2022.
- [46] M. Burkov, P. Lyubutin, and A. Byakov, “Lamb wave ultrasonic detection of barely visible impact damages of CFRP,” *Russian Journal of Nondestructive Testing*, vol. 55, no. 2, pp. 89–101, 2019.
- [47] M. S. Hameed, Z. Li, J. Chen, and J. Qi, “Lamb-wave-based multistage damage detection method using an active PZT sensor network for large structures,” *Sensors*, vol. 19, no. 9, p. 2010, 2019.

- [48] I. Dafydd and Z. Sharif Khodaei, “Analysis of barely visible impact damage severity with ultrasonic guided Lamb waves,” *Structural Health Monitoring*, vol. 19, no. 4, pp. 1104–1122, 2020.
- [49] S. Sikdar, A. Kundu, M. Jurek, and W. Ostachowicz, “Nondestructive analysis of debonds in a composite structure under variable temperature conditions,” *Sensors*, vol. 19, no. 16, p. 3454, 2019.
- [50] S. Mustapha, L. Ye, X. Dong, and M. M. Alamdari, “Evaluation of barely visible indentation damage (BVID) in CF/EP sandwich composites using guided wave signals,” *Mechanical Systems and Signal Processing*, vol. 76, pp. 497–517, 2016.
- [51] B. Eckstein, M. Moix Bonet, M. Bach, and C.-P. Fritzen, “Wave interaction at delamination and debondings due to impact damage in complex stiffened CFRP structures,” *Journal of Nondestructive Evaluation, Diagnostics and Prognostics of Engineering Systems*, vol. 1, no. 3, 2018.
- [52] N. Yue and M. Aliabadi, “A scalable data-driven approach to temperature baseline reconstruction for guided wave structural health monitoring of anisotropic carbon-fibre-reinforced polymer structures,” *Structural Health Monitoring*, vol. 19, no. 5, pp. 1487–1506, 2020.
- [53] B. Zima, “Damage detection in plates based on Lamb wavefront shape reconstruction,” *Measurement*, vol. 177, p. 109206, 2021.
- [54] J. Segers, S. Hedayatrasa, G. Poelman, W. Van Paepegem, and M. Kersemans, “Nonlinear local wave-direction estimation for in-sight and out-of-sight damage localization in composite plates,” *NDT & E International*, vol. 119, p. 102412, 2021.
- [55] G. Sha, M. Radzienski, R. Soman, T. Wandowski, M. Cao, and W. Ostachowicz, “Delamination imaging in laminated composite plates using 2d wavelet analysis of guided wavefields,” *Smart Materials and Structures*, vol. 30, no. 1, p. 015001, 2020.
- [56] F. Hervin, L. Maio, and P. Fromme, “Guided wave scattering at a delamination in a quasi-isotropic composite laminate: Experiment and simulation,” *Composite Structures*, vol. 275, p. 114406, 2021.
- [57] K. Balasubramaniam, S. Sikdar, R. Soman, and P. Malinowski, “Multi step structural health monitoring approaches in debonding assessment in a sandwich honeycomb composite structure using ultrasonic guided waves,” *Measurement*, vol. 194, p. 111057, 2022.



- [58] D. Ziaja and P. Nazarko, “Shm system for anomaly detection of bolted joints in engineering structures,” in *Structures*, vol. 33, pp. 3877–3884, Elsevier, 2021.
- [59] G. Azuara and E. Barrera, “Influence and compensation of temperature effects for damage detection and localization in aerospace composites,” *Sensors*, vol. 20, no. 15, p. 4153, 2020.
- [60] F. Lambinet and Z. S. Khodaei, “Damage detection & localization on composite patch repair under different environmental effects,” *Engineering Research Express*, vol. 2, no. 4, p. 045032, 2020.
- [61] G. Yan, X. Lu, and J. Tang, “Guided wave-based monitoring of evolution of fatigue damage in glass fiber/epoxy composites,” *Applied Sciences*, vol. 9, no. 7, p. 1394, 2019.
- [62] H. Alnuaimi, U. Amjad, P. Russo, V. Lopresto, and T. Kundu, “Monitoring damage in composite plates from crack initiation to macro-crack propagation combining linear and nonlinear ultrasonic techniques,” *Structural Health Monitoring*, vol. 20, no. 1, pp. 139–150, 2021.
- [63] C. Zhang, Z. Zhang, H. Ji, J. Qiu, and C. Tao, “Mode conversion behavior of guided wave in glass fiber reinforced polymer with fatigue damage accumulation,” *Composites Science and Technology*, vol. 192, p. 108073, 2020.
- [64] M. Dziendzikowski, A. Kurnyta, K. Dragan, S. Klysz, and A. Leski, “In situ barely visible impact damage detection and localization for composite structures using surface mounted and embedded PZT transducers: A comparative study,” *Mechanical Systems and Signal Processing*, vol. 78, pp. 91–106, 2016.
- [65] G. Sha, H. Xu, M. Radziński, M. Cao, W. Ostachowicz, and Z. Su, “Guided wavefield curvature imaging of invisible damage in composite structures,” *Mechanical Systems and Signal Processing*, vol. 150, p. 107240, 2021.
- [66] S. Sikdar, “Multi-level nondestructive analysis of joint-debond effects in sandwich composite structure,” *Polymer Testing*, vol. 80, p. 106149, 2019.
- [67] M. A. Fakihi, S. Mustapha, M. Makki Alamdari, and L. Ye, “Symbolic dynamics time series analysis for assessment of barely visible indenta-

- tion damage in composite sandwich structures based on guided waves,” *Journal of Composite Materials*, vol. 51, no. 29, pp. 4129–4143, 2017.
- [68] A. De Luca, D. Perfetto, A. De Fenza, G. Petrone, and F. Caputo, “A sensitivity analysis on the damage detection capability of a Lamb waves based SHM system for a composite winglet,” *Procedia Structural Integrity*, vol. 12, pp. 578–588, 2018.
- [69] S. Sikdar and W. Ostachowicz, “Ultrasonic Lamb wave-based debonding monitoring of advanced honeycomb sandwich composite structures,” *Strain*, vol. 55, no. 1, p. e12302, 2019.
- [70] L. Yu, Z. Tian, X. Li, R. Zhu, and G. Huang, “Core-skin debonding detection in honeycomb sandwich structures through guided wave wave-field analysis,” *Journal of Intelligent Material Systems and Structures*, vol. 30, no. 9, pp. 1306–1317, 2019.
- [71] M. Philibert, C. Soutis, M. Gresil, and K. Yao, “Damage detection in a composite T-joint using guided Lamb waves,” *Aerospace*, vol. 5, no. 2, p. 40, 2018.
- [72] C. Fendzi, N. Mechbal, M. Rebillat, M. Guskov, and G. Coffignal, “A general bayesian framework for ellipse-based and hyperbola-based damage localization in anisotropic composite plates,” *Journal of Intelligent Material Systems and Structures*, vol. 27, no. 3, pp. 350–374, 2016.
- [73] H. Zuo, Z. Yang, C. Xu, S. Tian, and X. Chen, “Damage identification for plate-like structures using ultrasonic guided wave based on improved MUSIC method,” *Composite Structures*, vol. 203, pp. 164–171, 2018.
- [74] R. Soman and P. Malinowski, “A real-valued genetic algorithm for optimization of sensor placement for guided wave-based structural health monitoring,” *Journal of Sensors*, vol. 2019, 2019.
- [75] K. Balasubramaniam, S. Sikdar, P. Fiborek, and P. H. Malinowski, “Ultrasonic guided wave signal based nondestructive testing of a bonded composite structure using piezoelectric transducers,” *Signals*, vol. 2, no. 1, pp. 13–24, 2021.
- [76] S. Sikdar, W. Van Paepegem, W. Ostachowicz, and M. Kersemans, “Nonlinear elastic wave propagation and breathing-debond identification in a smart composite structure,” *Composites Part B: Engineering*, vol. 200, p. 108304, 2020.

- [77] V. Memmolo, N. D. Boffa, L. Maio, E. Monaco, and F. Ricci, "Damage localization in composite structures using a guided waves based multi-parameter approach," *Aerospace*, vol. 5, no. 4, p. 111, 2018.
- [78] B. Zima and R. Kedra, "Detection and size estimation of crack in plate based on guided wave propagation," *Mechanical Systems and Signal Processing*, vol. 142, p. 106788, 2020.
- [79] J. Michaels, "Sparse array imaging with guided waves under variable environmental conditions," in *Structural health monitoring (SHM) in aerospace structures*, pp. 255–284, Elsevier, 2016.
- [80] N. Yue, Z. S. Khodaei, and M. Aliabadi, "Damage detection in large composite stiffened panels based on a novel SHM building block philosophy," *Smart Materials and Structures*, vol. 30, no. 4, p. 045004, 2021.
- [81] D. Li, M. Shi, F. Xu, C. Liu, J. Zhang, and D. Ta, "A new approach to guided wave ray tomography for temperature-robust damage detection using piezoelectric sensors," *Sensors*, vol. 18, no. 10, p. 3518, 2018.
- [82] T. Wandowski, P. Kudela, and W. Ostachowicz, "Numerical analysis of elastic wave mode conversion on discontinuities," *Composite Structures*, vol. 215, pp. 317–330, 2019.
- [83] S. Abbas, F. Li, J. Qiu, Y. Zhu, and X. Tu, "Optimization of ultrasonic guided wave inspection in structural health monitoring based on thermal sensitivity evaluation," *Journal of Low Frequency Noise, Vibration and Active Control*, vol. 40, no. 1, pp. 601–622, 2021.
- [84] "Ceram Tec group." <https://www.ceramtec-group.com/>. Accessed: 2022-02-30.
- [85] L. Varandas, D. Dalli, G. Catalanotti, and B. Falzon, "Estimating the mode I through-thickness intralaminar R-curve of unidirectional carbon fibre-reinforced polymers using a micromechanics framework combined with the size effect method," *Composites Part A: Applied Science and Manufacturing*, vol. 162, p. 107141, 2022.
- [86] K. Balasubramaniam, S. Sikdar, T. Wandowski, and P. H. Malinowski, "Ultrasonic guided wave-based debond identification in a gfrp plate with l-stiffener," *Smart Materials and Structures*, vol. 31, no. 1, p. 015023, 2021.

- [87] Z. Ismail, S. Mustapha, M. A. Fakhri, and H. Tarhini, "Sensor placement optimization on complex and large metallic and composite structures," *Structural Health Monitoring*, vol. 19, no. 1, pp. 262–280, 2020.
- [88] T. Kang, M. Yoon, S. Han, K.-M. Kim, and B. Koo, "Selection of optimal exciting frequency and Lamb wave mode for detecting wall-thinning in plates using scanning laser doppler vibrometer," *Measurement*, vol. 200, p. 111676, 2022.
- [89] J. Pan, K. Shankar, H. K. Singh, H. Wang, Z. Zhang, and H. Tong, "Vibration-based detection of skin-stiffener debonding on composite stiffened panels using surrogate-assisted algorithms," *Composite Structures*, vol. 270, p. 114090, 2021.
- [90] L. Maio, F. Ricci, V. Memmolo, E. Monaco, and N. Boffa, "Application of laser doppler vibrometry for ultrasonic velocity assessment in a composite panel with defect," *Composite Structures*, vol. 184, pp. 1030–1039, 2018.
- [91] K. Zheng, Z. Li, Z. Ma, J. Chen, J. Zhou, and X. Su, "Damage detection method based on Lamb waves for stiffened composite panels," *Composite Structures*, vol. 225, p. 111137, 2019.
- [92] O. Mouhat, A. Bybi, A. El Bouhmid, H. Boubel, O. Elmrabet, and M. Rougui, "The effect of ply orientation and damage detection in composite stiffened panel using Lamb waves," in *Solid State Phenomena*, vol. 298, pp. 161–166, Trans Tech Publ, 2019.
- [93] T. J. Saravanan, N. Gopalakrishnan, and N. P. Rao, "Damage detection in structural element through propagating waves using radially weighted and factored RMS," *Measurement*, vol. 73, pp. 520–538, 2015.
- [94] E. Wojtczak, M. Rucka, and M. Knak, "Detection and imaging of debonding in adhesive joints of concrete beams strengthened with steel plates using guided waves and weighted root mean square," *Materials*, vol. 13, no. 9, p. 2167, 2020.
- [95] M. Radzieński, P. Kudela, A. Marzani, L. De Marchi, and W. Ostachowicz, "Damage identification in various types of composite plates using guided waves excited by a piezoelectric transducer and measured by a laser vibrometer," *Sensors*, vol. 19, no. 9, p. 1958, 2019.
- [96] T. Jothi Saravanan, "Investigation of guided wave dispersion characteristics for fundamental modes in an axisymmetric cylindrical waveguide

- using rooting strategy approach,” *Mechanics of Advanced Materials and Structures*, vol. 29, no. 4, pp. 495–505, 2022.
- [97] A. Muc, M. Barski, A. Stawiarski, M. Chwał, and M. Augustyn, “Dispersion curves and identification of elastic wave modes for fiber metal laminates,” *Composite Structures*, vol. 255, p. 112930, 2021.
  - [98] M. Ciminello, N. D. Boffa, A. Concilio, V. Memmolo, E. Monaco, and F. Ricci, “Stringer debonding edge detection employing fiber optics by combined distributed strain profile and wave scattering approaches for non-model based SHM,” *Composite Structures*, vol. 216, pp. 58–66, 2019.
  - [99] P. Kudela and P. Fiborek, “Vectorization of the code for guided wave propagation problems,” in *European Workshop on Structural Health Monitoring*, pp. 707–715, Springer, 2020.
  - [100] P. Malinowski, T. Wandowski, and W. Ostachowicz, “Damage detection potential of a triangular piezoelectric configuration,” *Mechanical Systems and Signal Processing*, vol. 25, no. 7, pp. 2722–2732, 2011.
  - [101] K. Balasubramaniam, R. Soman, and P. Malinowski, “Guided waves based damage detection based on quadrant area using optical fiber sensors,” in *Health Monitoring of Structural and Biological Systems XVI*, vol. 12048, pp. 44–51, SPIE, 2022.
  - [102] J. Wee, B. Wells, D. Hackney, P. Bradford, and K. Peters, “Increasing signal amplitude in fiber Bragg grating detection of Lamb waves using remote bonding,” *Applied optics*, vol. 55, no. 21, pp. 5564–5569, 2016.
  - [103] A. Rytter, *Vibrational based inspection of civil engineering structures*. Ph.D thesis, Aalborg University, 1993.
  - [104] M. A. Fakh, M. Chiachío, J. Chiachío, and S. Mustapha, “A bayesian approach for damage assessment in welded structures using Lamb-wave surrogate models and minimal sensing,” *NDT & E International*, vol. 128, p. 102626, 2022.
  - [105] P. Pyrzanowski, “Estimation and consequences of the crack thickness parameter in the assessment of crack growth behaviour of “squat” type cracks in the rail–wheel contact zone,” *Engineering Fracture Mechanics*, vol. 74, no. 16, pp. 2574–2584, 2007.

- [106] J. E. Michaels and T. E. Michaels, “Guided wave signal processing and image fusion for in situ damage localization in plates,” *Wave motion*, vol. 44, no. 6, pp. 482–492, 2007.
- [107] K. Balasubramaniam, S. Sikdar, D. Ziaja, M. Jurek, R. Soman, and P. Malinowski, “A global-local damage localization and quantification approach in composite structures using ultrasonic guided waves and active infrared thermography,” *Smart Materials and Structures*, vol. 32, no. 3, p. 035016, 2023.
- [108] P. Perlikowski, K.-C. Woo, S. Lenci, and T. Kapitaniak, “Dynamics of systems with impacts,” *Journal of Computational and Nonlinear Dynamics*, vol. 12, no. 6, 2017.
- [109] R. Soman, P. Kudela, K. Balasubramaniam, S. K. Singh, and P. Malinowski, “A study of sensor placement optimization problem for guided wave-based damage detection,” *Sensors*, vol. 19, no. 8, p. 1856, 2019.
- [110] R. Bogenfeld, J. Kreikemeier, and T. Wille, “An analytical scaling approach for low-velocity impact on composite structures,” *Composite Structures*, vol. 187, pp. 71–84, 2018.
- [111] F. Sarasini, J. Tirillò, S. D’Altilia, T. Valente, C. Santulli, F. Touchard, L. Chocinski-Arnault, D. Mellier, L. Lampani, and P. Gaudenzi, “Damage tolerance of carbon/flax hybrid composites subjected to low velocity impact,” *Composites Part B: Engineering*, vol. 91, pp. 144–153, 2016.
- [112] “G ANGELONI group.” <https://www.g-angeloni.com/>. Accessed: 2022-02-30.
- [113] K. Balasubramaniam, D. Ziaja, M. Jurek, P. Fiborek, and P. Malinowski, “Experimental and numerical analysis of multiple low-velocity impact damages in a glass fibered composite structure,” *Materials*, vol. 14, no. 23, p. 7268, 2021.
- [114] S. Lv, X. Qin, J. Wei, L. Sun, L. Zhang, Q. Sui, and M. Jiang, “Linear annular path damage probability distribution based ultrasonic guided wave method for position imaging and tracking of multi-damage on plate-like carbon fiber composite structure,” *Thin-Walled Structures*, vol. 183, p. 110362, 2023.
- [115] R. Di Sante, “Fibre optic sensors for structural health monitoring of aircraft composite structures: Recent advances and applications,” *Sensors*, vol. 15, no. 8, pp. 18666–18713, 2015.

- [116] F. Yu and Y. Okabe, “Linear damage localization in CFRP laminates using one single fiber-optic Bragg grating acoustic emission sensor,” *Composite Structures*, vol. 238, p. 111992, 2020.
- [117] R. Soman, “Multi-objective optimization for joint actuator and sensor placement for guided waves based structural health monitoring using fibre Bragg grating sensors,” *Ultrasonics*, vol. 119, p. 106605, 2022.
- [118] A. Żak, M. Krawczuk, and W. Ostachowicz, “Propagation of in-plane elastic waves in a composite panel,” *Finite elements in analysis and design*, vol. 43, no. 2, pp. 145–154, 2006.
- [119] D. C. Betz, G. Thursby, B. Culshaw, and W. J. Staszewski, “Structural damage location with fiber Bragg grating rosettes and Lamb waves,” *Structural health monitoring*, vol. 6, no. 4, pp. 299–308, 2007.
- [120] J. Wee, D. Hackney, P. Bradford, and K. Peters, “Simulating increased Lamb wave detection sensitivity of surface bonded fiber Bragg grating,” *Smart Materials and Structures*, vol. 26, no. 4, p. 045034, 2017.
- [121] R. Soman, K. Balasubramaniam, A. Golestani, M. Karpiński, P. Malinowski, and W. Ostachowicz, “Actuator placement optimization for guided waves based structural health monitoring using fibre Bragg grating sensors,” *Smart Materials and Structures*, vol. 30, no. 12, p. 125011, 2021.
- [122] P. Fiborek, R. Soman, P. Kudela, and W. Ostachowicz, “Spectral element modeling of ultrasonic guided wave propagation in optical fibers,” *Ultrasonics*, vol. 124, p. 106746, 2022.
- [123] K. Balasubramaniam, R. Soman, and P. Malinowski, “Development of GUI based tool for the visualization of the FBG spectrum subjected to guided waves,” in *European Workshop on Structural Health Monitoring*, pp. 170–179, Springer, 2023.
- [124] K. Balasubramaniam, R. Soman, T. Wandowski, P. Malinowski, and W. Ostachowicz, “Through thickness inspection in various structures using ultrasonic wave coupling in an embedded fiber optical sensor,” in *Health Monitoring of Structural and Biological Systems XVII*, vol. 12488, pp. 86–92, SPIE, 2023.
- [125] P. Fiborek, P. Kudela, and W. Ostachowicz, “2D-3D interface coupling in the time domain spectral element method for the adhesive layer effects

- on guided wave propagation in composite plates,” *Smart Materials and Structures*, vol. 28, no. 5, p. 055014, 2019.
- [126] R. Soman, J. Wee, and K. Peters, “Optical fiber sensors for ultrasonic structural health monitoring: a review,” *Sensors*, vol. 21, no. 21, p. 7345, 2021.
- [127] F. Lambinet and Z. Sharif Khodaei, “Development of hybrid piezoelectric-fibre optic composite patch repair solutions,” *Sensors*, vol. 21, no. 15, p. 5131, 2021.
- [128] G. Pereira, M. McGugan, and L. P. Mikkelsen, “Fbg\_simul v1. 0: Fibre Bragg grating signal simulation tool for finite element method models,” *SoftwareX*, vol. 5, pp. 163–170, 2016.